

# Impacts of Degradation on Water, Energy, and Carbon Cycling of the Amazon Tropical Forests

Marcos Longo<sup>1</sup>, Sassan S. Saatchi<sup>1</sup>, Michael Keller<sup>2</sup>, Kevin W. Bowman<sup>3</sup>, Antonio Ferraz<sup>4</sup>, Paul R Moorcroft<sup>5</sup>, Douglas Morton<sup>6</sup>, Damien Bonal<sup>7</sup>, Paulo Brando<sup>8</sup>, Benoît Burban<sup>9</sup>, Géraldine Derroire<sup>10</sup>, Maiza Nara dos-Santos<sup>11</sup>, Victoria Meyer<sup>12</sup>, Scott Reid Saleska<sup>13</sup>, Susan Trumbore<sup>14</sup>, and Grégoire Vincent<sup>15</sup>

<sup>1</sup>Jet Propulsion Laboratory, California Institute of Technology

<sup>2</sup>USDA Forest Service

<sup>3</sup>Jet Propulsion Lab (NASA)

<sup>4</sup>Unknown

<sup>5</sup>Harvard University

<sup>6</sup>Goddard Space Flight Center (NASA)

<sup>7</sup>INRA

<sup>8</sup>Woods Hole Research Center

<sup>9</sup>INRAE UMR 0745 EcoFoG

<sup>10</sup>CIRAD

<sup>11</sup>Brazilian Agricultural Research Corporation

<sup>12</sup>Jet Propulsion Laboratory

<sup>13</sup>University of Arizona

<sup>14</sup>Max Planck Institute for Biogeochemistry

<sup>15</sup>Institut de Recherche pour le Developpement

November 30, 2022

## Abstract

Selective logging, fragmentation, and understory fires directly degrade forest structure and composition. However, studies addressing the effects of forest degradation on carbon, water, and energy cycles are scarce. Here, we integrate field observations and high-resolution remote sensing from airborne lidar to provide realistic initial conditions to the Ecosystem Demography Model (ED-2.2) and investigate how disturbances from forest degradation affect gross primary production (GPP), evapotranspiration (ET), and sensible heat flux (H). We used forest demography information retrieved from airborne lidar samples (13,500 ha) and calibrated with 817 inventory plots (0.25 ha) across precipitation and degradation gradients in the Eastern Amazon as initial conditions to ED-2.2 model. Our results show that the magnitude and seasonality of fluxes were modulated by changes in forest structure caused by degradation. During the dry season and under typical conditions, severely degraded forests (biomass loss [?] 66%) experienced water-stress with declines in ET (up to 34%) and GPP (up to 35%), and increases of H (up to 43%) and daily mean ground temperatures (up to 6.5°C) relative to intact forests. In contrast, the relative impact of forest degradation on energy, water, and carbon cycles markedly diminishes under extreme, multi-year droughts, as a consequence of severe stress experienced by intact forests. Our results highlight that the water and energy cycles in the Amazon are not only driven by climate and deforestation, but also the past disturbance and changes of forest structure from degradation, suggesting a much broader influence of human land use activities on the tropical ecosystems.

# Impacts of Degradation on Water, Energy, and Carbon Cycling of the Amazon Tropical Forests

Marcos Longo<sup>1</sup>, Sassan Saatchi<sup>2,3</sup>, Michael Keller<sup>2,4,5</sup>, Kevin Bowman<sup>2</sup>, António Ferraz<sup>2,3</sup>, Paul R. Moorcroft<sup>6</sup>, Douglas C Morton<sup>7</sup>, Damien Bonal<sup>8</sup>, Paulo Brando<sup>9,10,11</sup>, Benoît Burban<sup>12</sup>, Géraldine Derroire<sup>13</sup>, Maiza N dos-Santos<sup>5</sup>, Victoria Meyer<sup>2</sup>, Scott Saleska<sup>14</sup>, Susan Trumbore<sup>15</sup>, Grégoire Vincent<sup>16</sup>

<sup>1</sup>NASA Postdoctoral Program Fellow, Jet Propulsion Laboratory, California Institute of Technology,  
Pasadena CA, United States

<sup>2</sup>Jet Propulsion Laboratory, California Institute of Technology, Pasadena, CA, United States

<sup>3</sup>Institute of Environment and Sustainability, University of California, Los Angeles, CA, United States

<sup>4</sup>International Institute of Tropical Forestry, USDA Forest Service, Rio Piedras, Puerto Rico

<sup>5</sup>Embrapa Informática Agropecuária, Campinas, SP, Brazil

<sup>6</sup>Department of Organismic and Evolutionary Biology, Harvard University, Cambridge, MA, United States

<sup>7</sup>NASA Goddard Space Flight Center, Greenbelt, MD, United States

<sup>8</sup>Université de Lorraine, INRAE, AgroParisTech, UMR Silva, F-54000 Nancy, France

<sup>9</sup>Department of Earth System Science, University of California, Irvine, CA, United States

<sup>10</sup>Woods Hole Research Center, Woods Hole, MA, United States

<sup>11</sup>Instituto de Pesquisa Ambiental da Amazônia, Brasília, DF, Brazil

<sup>12</sup>Institut National de Recherche en Agriculture, Alimentation et Environnement (INRAE), UMR 0745

EcoFoG, Campus Agronomique, Kourou 97379, France

<sup>13</sup>Centre de Coopération Internationale en Recherche Agronomique pour le Développement (CIRAD),

UMR EcoFoG (Agroparistech, CNRS, INRAE, Université des Antilles, Université de Guyane), Campus

Agronomique, Kourou 97379, France

<sup>14</sup>University of Arizona, Tucson, AZ, United States

<sup>15</sup>Max-Planck-Institut für Biochemie, Jena, Germany

<sup>16</sup>AMAP, Univ Montpellier, IRD, CIRAD, CNRS, INRAE, Montpellier, 34000 France

## Key Points:

- Airborne lidar can be used to inform degradation-driven changes in structure to vegetation models

- 31 • Forest degradation typically depletes evapotranspiration and productivity and in-  
32 creases flammability
- 33 • Extreme droughts reduce functional differences between degraded and intact trop-  
34 ical forests

**Abstract**

Selective logging, fragmentation, and understory fires directly degrade forest structure and composition. However, studies addressing the effects of forest degradation on carbon, water, and energy cycles are scarce. Here, we integrate field observations and high-resolution remote sensing from airborne lidar to provide realistic initial conditions to the Ecosystem Demography Model (ED-2.2) and investigate how disturbances from forest degradation affect gross primary production (GPP), evapotranspiration (ET), and sensible heat flux (H). We used forest demography information retrieved from airborne lidar samples (13,500 ha) and calibrated with 817 inventory plots (0.25 ha) across precipitation and degradation gradients in the Eastern Amazon as initial conditions to ED-2.2 model. Our results show that the magnitude and seasonality of fluxes were modulated by changes in forest structure caused by degradation. During the dry season and under typical conditions, severely degraded forests (biomass loss  $\geq 66\%$ ) experienced water-stress with declines in ET (up to 34%) and GPP (up to 35%), and increases of H (up to 43%) and daily mean ground temperatures (up to 6.5°C) relative to intact forests. In contrast, the relative impact of forest degradation on energy, water, and carbon cycles markedly diminishes under extreme, multi-year droughts, as a consequence of severe stress experienced by intact forests. Our results highlight that the water and energy cycles in the Amazon are not only driven by climate and deforestation, but also the past disturbance and changes of forest structure from degradation, suggesting a much broader influence of human land use activities on the tropical ecosystems.

**Plain Language Summary**

In the Amazon, timber extraction and forest fires that are ignited by people are the chief causes of damages that we call forest degradation. Degradation is as widespread as deforestation, and change the way forests behave. Degraded forests may pump less water to the atmosphere and absorb less carbon dioxide from the atmosphere. To understand the differences in behavior between degraded and intact forests, we used high-resolution scanning laser data collected from aircraft flights over regions in the Amazon where we knew if and when the forest was degraded. Then, we provided these data to a computer program that calculates the exchange of water and carbon between the forest and the atmosphere. We found that, during the dry season, degraded forests are 6.5°C warmer, pump 1/3 less water, absorb 1/3 less carbon, and show higher fire risk than in-

67 tact forests. To our surprise, when the Amazon is hit by severe droughts, intact forests  
68 start to behave like degraded forests, because all forests run out of water and become  
69 hot. Our results are important because they show that forest degradation caused by peo-  
70 ple can have large impacts on dry-season climate and favor more fire, especially during  
71 typical, non-drought years.

## 72 **1 Introduction**

73 Tropical forests account for 25–40% of total carbon stocks in terrestrial ecosystems  
74 (Sabine et al., 2004; Meister et al., 2012), but their maintenance and functioning have  
75 been weakened by climate and land-use change. As a result, tropical forests may shift  
76 to net sources of carbon to the atmosphere, with residence time of carbon in forests de-  
77 clining by 50% (Davidson et al., 2012; Grace et al., 2014; Lewis et al., 2015; Erb et al.,  
78 2016). Land use and land cover changes contribute to nearly 15% of total annual car-  
79 bon emissions (Harris et al., 2012; Friedlingstein et al., 2019). However, most studies as-  
80 sessing the effects of land use change on tropical forest stocks and fluxes have focused  
81 on the effects of deforestation (e.g., Harris et al., 2012; Achard et al., 2014). The effects  
82 of logging, understory fires and forest fragmentation — collectively known as *forest degra-*  
83 *dation* (Hosonuma et al., 2012) — could play a comparable role in the forest’s energy,  
84 water, and carbon cycle, but they remain poorly quantified.

85 Significant fractions of the remaining tropical forests are located within 1 km to the  
86 forest’s edge (Haddad et al., 2015; Lewis et al., 2015) and thus are probably degraded  
87 (Asner et al., 2006; Morton et al., 2013; Pütz et al., 2014; Tyukavina et al., 2016; Potapov  
88 et al., 2017). The area impacted by forest degradation in the Amazon each year is highly  
89 uncertain, but likely comparable to deforestation (Asner et al., 2006; Morton et al., 2013;  
90 Tyukavina et al., 2017). Total carbon losses attributable to degradation may be simi-  
91 lar or exceed deforestation-related losses in tropical forests (Berenguer et al., 2014; Pear-  
92 son et al., 2017; Baccini et al., 2017; Aragão et al., 2018; Erb et al., 2018), and degra-  
93 dation may even dominate the carbon losses in indigenous lands and protected areas (Walker  
94 et al., 2020). At the local scale, carbon stocks in degraded forests are extremely variable.  
95 Lightly disturbed forests (e.g., reduced-impact logging) store as much carbon as intact  
96 forests, while forests impacted by severe or multiple disturbances may lose 65–95% of  
97 their original carbon stocks (Berenguer et al., 2014; Alamgir et al., 2016; Longo et al.,  
98 2016; Rappaport et al., 2018; Ferraz et al., 2018). Unquestionably, estimates of fluxes

99 from forest degradation and regeneration are more uncertain than emissions from de-  
100 forestation (Aragão et al., 2014; Morton, 2016; Bustamante et al., 2016), because their  
101 impacts on forests are more subtle than deforestation and thus more difficult to detect  
102 and quantify with traditional remote sensing techniques.

103 Selective logging and fires also modify the forest structure, composition and func-  
104 tioning. For example, selective logging in the tropics generally targets large trees (diam-  
105 eter at breast height,  $DBH \geq 40\text{--}60$  cm) from a few marketable species (e.g., Feldpausch  
106 et al., 2005; Blanc et al., 2009; Pinagé et al., 2019), but the other logging structures such  
107 as skid trails and log decks kill or damage mostly small trees ( $DBH < 20$  cm) (Feldpausch  
108 et al., 2005). Likewise, fire mortality decreases with tree size and the bark thickness (e.g.,  
109 Brando et al., 2012; Pellegrini et al., 2016), although areas disturbed by recurrent fires  
110 also show significant losses of large trees (Martins et al., 2012). Consequently, degrada-  
111 tion creates more open canopies and thinner understory (e.g., d’Oliveira et al., 2012; Pinagé  
112 et al., 2019; Silvério et al., 2019) and increased abundance of fast-growing, low wood-  
113 density species (Barlow et al., 2016; Both et al., 2019; Brando, Silvério, et al., 2019).

114 Previous studies indicate an increase in dry-season length in parts of the Amazon  
115 where both deforestation and forest degradation are pervasive (e.g., Fu et al., 2013; Sena  
116 et al., 2018), and that the onset of the wet season is modulated by forest transpiration  
117 (J. S. Wright et al., 2017). Temperature and vapor pressure deficit (VPD), important  
118 drivers of evapotranspiration (ET), were found by Kapos (1989) to be significantly higher  
119 near forest edges. Likewise, Jucker et al. (2018) installed a network of micrometeorolog-  
120 ical measurements across a study area in Sabah, Malaysia, that included intact forests,  
121 a broad range of degraded forests and oil-palm plantations, and found that forest struc-  
122 ture, along with topographic features, explained most of the variance in understory tem-  
123 perature. Yet, only a few studies on experimental sites quantified the magnitude, sea-  
124 sonality, and interannual variability of water, and energy cycles in degraded forests. For  
125 example, S. D. Miller et al. (2011) analyzed the impact of reduced-impact, low-intensity  
126 selective logging in the Amazon using eddy covariance towers and found only minor im-  
127 pacts of logging on sensible and latent heat fluxes. Recently, Brando, Silvério, et al. (2019)  
128 compared eddy covariance data from two towers at an experimental fire site in the Ama-  
129 zon forest, and found declining differences in gross primary productivity and small dif-  
130 ferences in evapotranspiration between the control and burned area between 4 and 8 years  
131 after the last burn.

132 Field inventory plots are fundamental to sample the structure and species compo-  
133 sition of tropical forests, but they also have important limitations to characterize the het-  
134 erogeneity of degraded landscapes. First, the number of plots required to characterize  
135 stands increase with heterogeneity, often reaching impractical numbers (Marvin et al.,  
136 2014). In addition, most tropical forest degradation occurs in private landholdings and  
137 privately managed logging concessions, where limited access by researchers may create  
138 sampling bias towards well-managed areas, which generally experience less intensive degra-  
139 dation. However, airborne laser scanning (airborne lidar) can circumvent these limita-  
140 tions over large areas with sub-meter resolution. Airborne lidar data have been used suc-  
141 cessfully to quantify structural characteristics of the canopy such as height and leaf area  
142 distribution (Hunter et al., 2013; Shao et al., 2019). Moreover, these data have also been  
143 used to quantify changes in canopy structure and carbon stocks at local to regional scale  
144 that experienced multiple levels of degradation (e.g., Asner et al., 2010; Longo et al., 2016;  
145 Ferraz et al., 2018; Meyer et al., 2019).

146 Numerical models can be used to understand the links between changes in forest  
147 structure, light and water availability for different local plant communities, and the over-  
148 all impact on energy, water, and carbon fluxes between forests and the atmosphere. In  
149 the past, *big-leaf* models have been modified to account for the long-term impacts of se-  
150 lectively logged tropical forests on the carbon cycle of tropical forests (e.g., Huang et al.,  
151 2008; Huang & Asner, 2010). However, big-leaf models cannot represent the mechanisms  
152 that control access and availability of light and water in complex and heterogeneous for-  
153 est structures (Purves & Pacala, 2008; Fisher et al., 2018). Individual-based models can  
154 represent the changes in the population structure and micro-environments due to degra-  
155 dation (R. Fischer et al., 2016; Maréchaux & Chave, 2017), but the complexity and com-  
156 putational burden of these simulations often limit their application to single sites. Cohort-  
157 based models, such as the Ecosystem Demography (ED-2.2) model (Medvigy et al., 2009;  
158 Longo, Knox, Medvigy, et al., 2019), strike a balance between these end-members be-  
159 cause they can efficiently represent the horizontal and vertical heterogeneity of forests,  
160 provided that they are informed with initial conditions and accurate parameterizations  
161 that can capture the landscape variability.

162 In this study, we use airborne lidar data to quantify forest structure variability across  
163 the Amazon in order to provide critical initial conditions for ecosystem demography mod-  
164 els. We also investigate the role of forest degradation on the Amazon forest productiv-

165 ity, flammability, as well as the degradation impacts on the water and energy cycles. Specif-  
166 ically, we seek to answer the following questions:

- 167 1. What are the relationships between degradation metrics (e.g. biomass loss) and  
168 changes in carbon, water, and energy fluxes, and how does it vary across seasons  
169 and regions with different rainfall regimes?
- 170 2. How do droughts affect the relationships between degradation and ecosystem func-  
171 tioning?
- 172 3. Does forest degradation make Amazon forests more susceptible to fires? If so, which  
173 parts of the Amazon experience the largest flammability response to degradation?

174 To this end, we integrate field inventory plots with high-resolution airborne lidar data  
175 over five study regions in the Eastern Amazon along a precipitation gradient and with  
176 a broad range of anthropogenic disturbance histories, to provide initial conditions to ED-  
177 2.2 that realistically represent the structural diversity of degraded forests. While lim-  
178 ited to specific regions in the Amazon where detailed degradation information exists, our  
179 goal is to provide a framework that can be extended to larger scales, including biome-  
180 and pantropical scales.

## 181 **2 Materials and Methods**

### 182 **2.1 Study regions**

183 We selected five study regions across a gradient of disturbance and climate con-  
184 ditions where ground and airborne lidar are available to study the forest function (Fig-  
185 ure 1; Table 1). Three of these sites include eddy covariance tower measurement of en-  
186 ergy, water, and carbon dioxide fluxes for comparison with the model simulations, and  
187 have been the focus of several ecological studies in the past.

- 188 1. *Paracou, French Guiana (GYF)* is a field station where a logging experiment was  
189 conducted between 1987 and 1988 that includes intact forest controls and three  
190 selective logging treatments: timber extraction using conventional logging tech-  
191 niques, timber extraction and canopy thinning, and timber and fuelwood extrac-  
192 tion followed by canopy thinning (Gourlet-Fleury et al., 2004). The eddy covari-  
193 ance tower at the site is located in the undisturbed forest and has been operational  
194 since 2004 (Guyaflux; Bonal et al., 2008).

**Table 1.** Overview of the study regions, including mean annual precipitation (MAP) and dry-season length (DSL).

Region (Code)	Coordinates	MAP <sup>a</sup> [mm]	DSL <sup>b</sup> [mo]	Lidar [ha]	Inventory [ha]	Disturbances <sup>c</sup>
Paracou (GYF)	5.28°N; 52.91°W	3040	2(0)	963	79.8	INT, CL1, LTH
Belterra (BTE)	3.09°S; 54.95°W	1890	5(1)	4057	16.7	INT, RIL, BN1, BN2, BN3
Paragominas (PRG)	3.15°S; 47.61°W	1850	6(2)	3217	35.6	INT, RIL, CL1, BN1, LB1, BN2, BN3
Feliz Natal (FZN)	12.14°S; 54.68°W	1940	5(4)	4210	14.0	INT, CL1, CL2, BN1, LB1, BN2, BN3
Tanguro (TAN)	13.08°S; 52.41°W	1800	5(4)	1006	22.9	INT, BN1, BN3, BN6

<sup>a</sup> Source for mean annual precipitation (MAP) data: GYF – Gourlet-Fleury et al. (2004); other regions – nearest site available at INMET (2019).

<sup>b</sup> Dry-season length (DSL): number of months with precipitation below 100 mm; numbers in parentheses indicate number of severely dry months (precipitation below 30 mm).

<sup>c</sup> Disturbance history classes: INT – intact; RIL – reduced-impact logging; CL $x$  – conventional logging ( $x$  times); LTH – conventional logging and thinning; LB1 – conventional logging and burned (once); BN $x$  – burned  $x$  times.

- 195        2. *Belterra, Brazil (BTE)*. Over the past 100 years, this region experienced cycles  
196            of economic growth and recession that created a complex landscapes dominated  
197            by deforestation, degradation and second-growth (VanWey et al., 2007), with in-  
198            tact areas in the Tapajós National Forest. An eddy covariance tower known as Km  
199            67 overlaps with one of the surveyed sites and has data for 2001–2005, and 2008–  
200            2011 (Hayek et al., 2018).
- 201        3. The *Paragominas, Brazil (PRG)* region used to be within the largest timber pro-  
202            duction area in Brazil and has undergone selective logging since the 1970s (Veríssimo  
203            et al., 1992). Since the 1990s, the economy has shifted towards agriculture, intro-  
204            ducing large-scale deforestation such that nearly half of the original forest cover  
205            has been lost, and most of the remaining areas have been logged (Pinto et al., 2009).
- 206        4. *Feliz Natal, Brazil (FZN)* is located at the southern fringe of the Amazon in a mo-  
207            saic landscape of soybean fields, grazing lands, and logged forests. This region reg-  
208            ularly experiences severe dry seasons and frequent understory fires (Morton et al.,  
209            2013; Rappaport et al., 2018).
- 210        5. *Tanguro, Brazil (TAN)* is located in an experimental fire study area within a larger  
211            landscape covered by intact forests and forests that were disturbed with low-intensity  
212            understory fires (one, three, and six times) between 2004 and 2010 (Brando et al.,  
213            2014). The surveyed region also includes two eddy covariance towers that have been  
214            operating since 2014 both at the intact and burned forests (Brando, Silvério, et  
215            al., 2019).

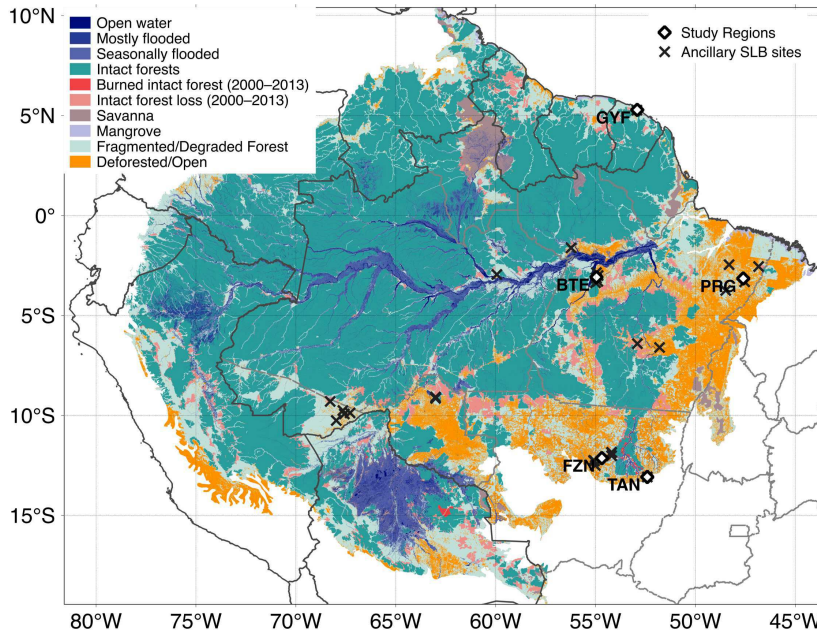


**Figure 1.** Location of the five study regions within the Amazon biome region, along with land classification as of 2013. Intact forest and intact forest loss were obtained from Potapov et al. (2017); open and deforested areas were obtained from PRODES-INPE (2018) (Brazil) and areas with tree cover below 20% according to Hansen et al. (2013) (other countries); wetlands and water bodies in the Amazon River Basin were from Hess et al. (2015) and savannas and mangroves were obtained from Olson et al. (2001).

216 These five study regions were sampled at multiple sites by small-footprint, multiple-  
 217 return airborne lidar. The lidar data provided both the terrain elevation at high spatial  
 218 resolution (1-m) and detailed information about the vertical structure of forests from a  
 219 uniform point cloud density to meet a minimum return density of 4 returns per  $\text{m}^2$  over  
 220 99.5% of the area (Leitold et al., 2015). Living trees of diameter at breast height  $\text{DBH} \geq$   
 221 10 cm were either botanically identified (experimental plots in GYF) or identified from  
 222 field characteristics by local parataxonomists. To characterize the disturbance history,  
 223 we used either published information from the experimental regions GYF (Gourlet-Fleury  
 224 et al., 2004; Bonal et al., 2008; Wagner et al., 2013) and TAN (Brando et al., 2012, 2014),  
 225 or the disturbance history analysis from (Longo et al., 2016), which was based on a vi-  
 226 sual interpretation of the Normalized Burn Ratio (NBR) of cloud-free Landsat images  
 227 since 1984, and complemented with information from logging companies for the reduced-  
 228 impact logging sites (e.g., Pinagé et al., 2019). Details on site-specific data used in this

229 study are available in Text 1 and previous work (Longo et al., 2016; Vincent et al., 2017;  
230 Brando, Silvério, et al., 2019), and were obtained through the Paracou Experimental Sta-  
231 tion and the Sustainable Landscapes Brazil data servers (Paracou Portal, 2016; Sustain-  
232 able Landscapes Brazil, 2019; dos-Santos et al., 2019).

## 233 **2.2 Overview of the modeling framework**

234 In this study, we used the Ecosystem Demography model, version 2.2 (ED-2.2) (Moorcroft  
235 et al., 2001; Medvigy et al., 2009; Longo, Knox, Medvigy, et al., 2019) to simulate the  
236 impacts of forest structure on energy, water, and carbon cycles. For any point of inter-  
237 est, the ED-2.2 model simulates the forest structure and functional diversity across a land-  
238 scape, and simulates the energy, water, and carbon budgets for multiple canopy envi-  
239 ronments, which represent the forest heterogeneity (Longo, Knox, Medvigy, et al., 2019).  
240 ED-2.2 has been successfully evaluated and used in both short-term and long-term stud-  
241 ies in the Amazon forest (Powell et al., 2013; Zhang et al., 2015; Levine et al., 2016; Longo,  
242 Knox, Levine, et al., 2019). In ED-2.2, the horizontal and vertical heterogeneities of forests  
243 are represented through a hierarchical structure. Each area with the same climate (e.g.,  
244 footprint of an eddy covariance tower or a grid cell in a gridded meteorological driver)  
245 is called a *polygon*. Each polygon is subdivided into *patches*, which represent collections  
246 of forest gaps within a polygon that share a similar age since last disturbance and same  
247 disturbance type (although not necessarily contiguous in space). Patches are further sub-  
248 divided into *cohorts*, which are collections of individual plants that have similar size and  
249 similar functional group. Importantly, because ED-2.2 incorporates the horizontal het-  
250 erogeneity of the plant community structure and composition, the model can efficiently  
251 incorporate and simulate the dynamics of degraded forests.

252 Most of the ED-2.2 modules used in this study have been previously described in  
253 Longo, Knox, Medvigy, et al. (2019). The main changes used in this study include (1)  
254 a modified height-diameter allometry based on the Jucker et al. (2017) approach and lo-  
255 cally collected field data that can be used consistently by the initialization and model;  
256 (2) an improved allocation to living and structural tissues, which is now based on more  
257 recent allometric equations (Chave et al., 2014; Falster et al., 2016) and datasets (Falster  
258 et al., 2015); (3) a revised photosynthesis solver, which now accounts for the maximum  
259 electron transport ratio and the maximum triose-phosphate utilization (von Caemmerer,  
260 2000; Oleson et al., 2013; Lombardozzi et al., 2018); (4) updated values of traits and trade-

261 offs, using multiple studies and trait databases, including GLOPNET, TRY, and NGEETropics (I. J. Wright et al., 2004; Santiago & Wright, 2007; Chave et al., 2009; Kattge  
262 et al., 2009, 2011, 2020; Baraloto et al., 2010; Powers & Tiffin, 2010; Gu et al., 2016; Ba-  
263 har et al., 2017; Norby et al., 2017). These changes are described in Text 2. Moreover,  
264 we used an approach developed by X. Xu (unpublished) and based on Lloyd et al. (2010)  
265 to account for light-dependent plasticity of three leaf traits (specific leaf area, leaf turnover  
266 rate, and carboxylation capacity), and calibrated using existing data (Lloyd et al., 2010;  
267 Russo & Kitajima, 2016; Keenan & Niinemets, 2016).

269 To obtain initial conditions for ED-2.2 from airborne lidar, we devised a multi-step  
270 approach that links airborne lidar data with ecosystem properties (Figure 2). Here we  
271 provide a summary of the initialization procedure; the technical details of this approach  
272 are described in Text 3. For step 1, we split all collected point cloud data into  $50 \times 50$  m  
273 columns, simulated waveforms from the discrete returns (Blair & Hofton, 1999; Popescu  
274 et al., 2011; Hancock et al., 2019) to obtain unscaled leaf area density profiles based on  
275 the vertical distribution of returns (e.g., MacArthur & Horn, 1969; Ni-Meister et al., 2001;  
276 Stark et al., 2012; Antonarakis et al., 2014; Tang & Dubayah, 2017), and assigned the  
277 relative proportion of each plant functional type provided by one of the 769 training plots  
278 that had the most similar vertical structure; the similarity was based on the profile com-  
279 parison that yielded the smallest Kolmogorov-Smirnov statistic. The vertical profile was  
280 split into cohort layers centered around local maxima or saddle points, using a modified  
281 procedure based on function `peaks` (package `RSEIS`, Lees, 2017) of the R statistical soft-  
282 ware (R Core Team, 2019). For step 2, we used a collection of 817 forest inventory plots  
283 (0.16–0.26 ha) that were also surveyed by airborne lidar, which included plots from all  
284 study regions as well additional sites available from Sustainable Landscapes Brazil (SLB)  
285 and used in a previous study (ancillary SLB sites, Figure 1; Longo et al., 2016); we de-  
286 veloped statistical models based on subset selection of regression (A. J. Miller, 1984) and  
287 heteroskedastic distribution of residuals (Mascaro et al., 2011) to estimate plot-level prop-  
288 erties (aboveground biomass, basal area, stem number density, leaf area index) from point  
289 cloud metrics and field estimates, following the approach by Longo et al. (2016). For step  
290 3, we sought to obtain a plot-specific scaling factor to the leaf area density profile that  
291 produced the best agreement between the four estimated plot-level properties from step  
292 1 and the plot-level properties obtained by integrating the vertical distribution from step  
293 2, by minimizing the sum of relative square differences of the four properties. For step

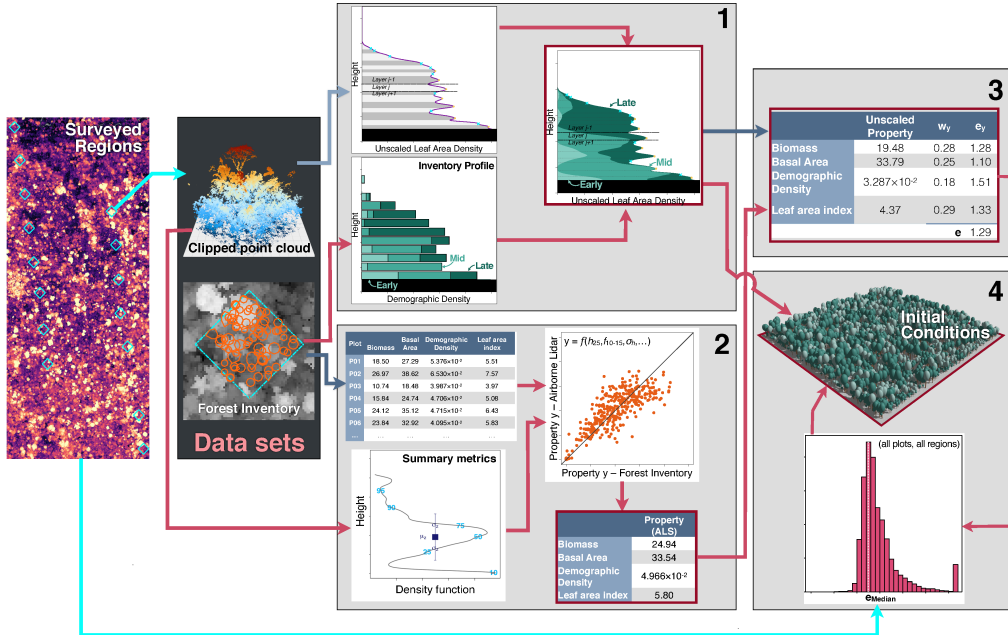


**Figure 2.** Schematic representation of the method to obtain initial conditions for ED-2 from airborne lidar. Each light box represents one step in the procedure. The results of each step are highlighted with a red border. Dark blue arrows are stages that require individual-based allometric equations, and light blue arrows are stages that require a light extinction model.

294 4, we analyze the scaling factor distribution for all plots for which we could test the ap-  
 295 proach, and define a unique and global scaling factor, based on the median scaling factor  
 296 to, that is used to correct all predicted profiles.

297 Once we obtained the initial conditions for each 50×50 m column, we grouped in-  
 298 dividual columns based the disturbance history (degradation level) and the study region  
 299 (Table 1). We used the following broad categories for disturbance history: intact (INT),  
 300 reduced-impact logging (RIL), conventional logging (CL $x$ , where  $x$  is the number of log-  
 301 ging disturbances), conventional logging and thinning (LTH), logged and burned once  
 302 (LB1) and burned (BN $x$ , where  $x$  is the number of burns). Importantly, we did not per-  
 303 form any averaging or sampling of the individual columns before providing them to ED-  
 304 2.2; instead, we provided all columns to the model, so the initial conditions character-  
 305 ize the observed distribution of forest structures that exist within each group.

### 2.3 Assessment of the modeling framework

We evaluated three characteristics to assess the ability of model framework to represent the forest structure heterogeneity caused by degradation, and to represent components of the energy, water, and carbon cycle. First, we quantified the ability of the airborne lidar initialization to capture the differences in forest structure caused by degradation. Second, we assessed whether the model can realistically represent fluxes and storage of water, energy and carbon across different regions. Third, we compared the model sensitivity to degradation-driven effects on fluxes and storage with independent observations.

To evaluate the airborne lidar initialization, we used a cross-validation approach in which we replicated the procedure described above (Section 2.2) 2000 times, using a hierarchical bootstrap approach. We first sampled regions (with replacement), to ensure that some regions would be entirely excluded from the replicate, then we sampled plots (also with replacement), to ensure that the replicate had the same number of plots as the original training data set. We then predicted the structure of all plots in the excluded regions, using iterations that did not have any plot in the training data set; to make this number consistent across regions, we used the smallest number of iterations that met this criterion across all regions ( $n = 612$ ). Finally, for each region, we compared the average forest structure from all cross-validation replicates that excluded the region from the training stage. Because estimates of forest properties have larger uncertainties in smaller plots (Chave et al., 2004; Meyer et al., 2013; Mauya et al., 2015), we only evaluated the method when a disturbance class within a region had at least 20 plots.

To verify the model's ability to realistically represent the regional variability of fluxes and storage, we carried out ED-2.2 simulations initialized with airborne lidar for the intact forests regions where eddy covariance tower and forest inventory plots co-located with airborne lidar were available (GYF and BTE). Region TAN had two eddy-covariance towers, one within the footprint of the burned forests and a second in intact forest (Brando, Silvério, et al., 2019), which allowed us to contrast the model's predicted impacts of degradation on fluxes and biophysical properties with the pair of tower measurements.

## 2.4 Model configuration and analyses

Our main focus is to understand the role of degradation-driven changes in forest structure in altering both the state and the fluxes of energy, water, and carbon, both under typical and extreme climate. To account for regional differences in climate and to sample a broad range of interannual variability, we used time series of meteorological drivers pooled from gridded reanalyses (one set of time series per region). For most meteorological variables required by ED-2.2 (pressure, temperature, humidity, incoming short-wave and longwave radiation, and winds), we used  $0.625^\circ \times 0.5^\circ$ , hourly averages (1980–2016) from the version 2 of the Modern-Era Retrospective Analysis for Research and Applications (MERRA-2, Gelaro et al., 2017). MERRA-2 precipitation is known to have significant negative biases in the tropics (Beck et al., 2019); therefore we used the  $0.1^\circ \times 0.1^\circ$ , 3-hourly precipitation rates from the version 2 of the Multi-Source Weighted Ensemble Precipitation product (MSWEP-2, Beck et al., 2019). To ensure that the only difference between simulations in the same study region was the distribution of forest structures, we imposed the same edaphic conditions: free-drainage soils with 8 m deep, and nearly equal fractions of sand (32%), silt (34%), and clay (34%). To avoid confounding effects from post-disturbance mortality and recovery, all simulations were carried out without enabling dynamic vegetation, such that the differences in forest structure would remain the same for the entire time series, and all differences between simulations in the same region could be attributable to well-characterized differences in forest structure.

To investigate the role of degradation on fire risk, we built on the original fire model from ED-1 (Moorcroft et al., 2001) to determine when fire-prone conditions would occur in each patch. The flammable area  $\alpha_F$  ( $\% \text{ yr}^{-1}$ ) is calculated from the fire disturbance rate  $\lambda_F$  ( $\text{yr}^{-1}$ ):

$$\alpha_F = 100 [1 - \exp(-\lambda_F \Delta t)], \quad (1)$$

$$\lambda_F = \begin{cases} I C_{\text{Fuel}} & , \text{ if } \left[ \frac{1}{|z_F|} \int_{z_F}^0 \vartheta(z) dz \right] < (1-f) \vartheta_{\text{WP}} + f \vartheta_{\text{Fc}} \\ 0 & , \text{ otherwise} \end{cases} . \quad (2)$$

where  $\Delta t = 1 \text{ yr}$ ;  $I = 0.5 \text{ m}^2 \text{ kgC yr}^{-1}$  is a fire intensity parameter;  $z_F = 30 \text{ cm}$  is the depth of the soil layer used to estimate dryness;  $\vartheta$  ( $\text{m}^3 \text{ m}^{-3}$ ) is the soil moisture;  $\vartheta_{\text{WP}}$  is the permanent wilting point and  $\vartheta_{\text{Fc}}$  is the field capacity, both defined as in Longo, Knox, Medvigy, et al. (2019); and  $f = 0.02$  is a phenomenological parameter that defines dry conditions. Because understory fires are the dominant type of fire in the Ama-

364 zon (A. Alencar et al., 2006; Morton et al., 2013), we considered fuels to be comprised  
365 by above-ground litter, above-ground coarse woody debris, and above-ground biomass  
366 from grasses and seedlings (trees with height  $< 2$  m); canopy trees were not considered  
367 to be fuels. The fire parameterization, although simple, has been previously demonstrated  
368 to capture the general features of fire regime across tropical South America (Longo, Knox,  
369 Levine, et al., 2019).

### 370 **3 Results**

#### 371 **3.1 Evaluation of the model initialization and simulated dynamics**

372 The ED-2.2 model initialization approach from airborne lidar (Figure 3) captured  
373 the main differences in forest structure and composition, both across study regions and  
374 along degradation gradients. To illustrate the initialization, we focus on the basal area  
375 distribution obtained from cross-validation at disturbance histories within study regions  
376 that had at least 20 plots (Figure 3). At sites GYF, PRG, and TAN, the airborne lidar  
377 initialization predicted the total basal area with absolute biases ranging from 3% (GYF)  
378 to 13% (TAN), and root mean square error of the order of 18–27% (Figures 3c, 3f and  
379 3i). The largest absolute discrepancies occurred for intermediate-sized trees ( $20 \leq \text{DBH}$   
380  $< 40$  cm) at GYF and PRG, where the airborne lidar initialization underestimated basal  
381 area by 2.9 and 4.3  $\text{cm}^2 \text{m}^{-2}$ , respectively (Figures 3c and 2f). The largest overestima-  
382 tion of airborne lidar was observed among larger trees ( $60 \leq \text{DBH} < 100$  cm) in intact  
383 forests at GYF (2.4  $\text{cm}^2 \text{m}^{-2}$ ; Figure 3c). The size distribution of most degraded forests  
384 were well characterized (Figures 3a-b, 3d-e and 3g); the largest deviations from inven-  
385 tory were observed in logged and burned forests in PRG, where airborne lidar underes-  
386 timated total basal area by 3.0  $\text{cm}^2 \text{m}^{-2}$  (Figure 3d). Likewise, the initialization algo-  
387 rithm represented the higher relative abundance of early successional plants in the most  
388 degraded sites, and the dominance of mid- and late-successional plants at intact forests  
389 at GYF and PRG (Figure S1), and realistically represented the leaf area distribution across  
390 regions and degradation levels (Figure S2).

391 ED-2.2 simulations using forest inventory and airborne lidar as initial conditions  
392 were compared with eddy covariance tower estimates of all sites (Figures 4 and S4-S9,  
393 and Table S1). Gross primary productivity (GPP) generally showed small biases rela-  
394 tive to tower estimates ( $-0.046$  to  $+0.394 \text{ kgC m}^{-2} \text{ yr}^{-1}$ ), and relatively small errors (less

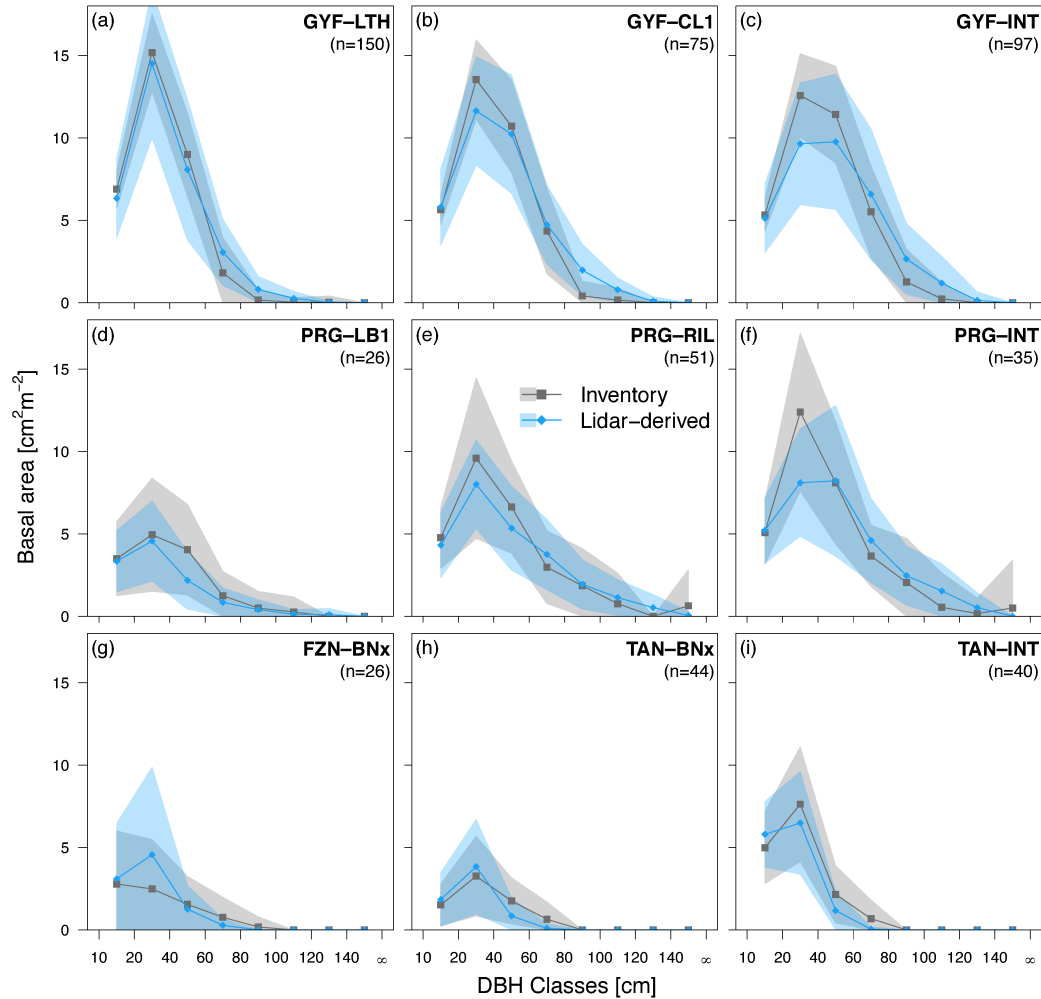


**Figure 3.** Assessment of basal area distribution as a function of diameter at breast height (DBH) for different study regions and degradation levels. Grey points are obtained from forest inventory plots, and blue points are obtained from the airborne lidar initialization (Figure 2) using a 612-fold regional cross-validation (i.e. excluding all plots from region in the calibration stage). Bands around points correspond to the standard deviation either across all plots in the same category (inventory) or across all plots and replicates (lidar). Sites: GYF – Paracou, PRG – Paragominas, FZN – Feliz Natal, TAN – Tanguro. Disturbance classes: BNx – Burned twice or more, CL1 – conventional logging (once), LB1 – logged and burned once, LTH – logged and thinned, RIL – reduced-impact logging, INT – intact. Additional comparisons are shown in the Supporting Information: basal area as functions of plant functional type (Figure S1); leaf area index profiles as functions of height (Figure S2); comparisons for Belterra (BTE-RIL) (Figure S3).

395 than observed variability) at all sites, regardless of the initial conditions (Figure 4; Ta-  
396 ble S1). While the GPP seasonality was correctly represented at GYF, the model did  
397 not capture the late wet-season decrease and early dry-season increase of GPP at BTE,  
398 and it showed a delayed dry-season decline GPP at TAN compared to tower estimates  
399 (Figure S4). Net ecosystem productivity (NEP), on the other hand, showed significant  
400 biases, large errors, and relatively small correlation with tower estimates (Figure 4; Ta-  
401 ble S1), which were driven by excessive seasonality of heterotrophic respiration (Figure S5).  
402 Because the initial carbon stocks in necromass pools are uncertain, and the results on  
403 magnitude and seasonality of ecosystem respiration (and consequently NEP) are incon-  
404 sistent with tower estimates, we will not discuss the simulation results in terms of res-  
405 piration and NEP.

406 Water fluxes also showed small biases relative to the observed variability at GYF,  
407 TNF and TAN (Burned), regardless of the initialization ( $-0.01$  to  $+0.54$  mm day $^{-1}$ ; Fig-  
408 ures 4a and 4c; Table S1); biases at TAN (Intact) were larger ( $0.69$ – $0.82$  mm day $^{-1}$ ).  
409 With the exception of TAN (Burned), the correlation between ED-2.2 and tower was high  
410 at daily averages (Figures 4b and 4d; Table S1). At TAN (Burned), the poorer agree-  
411 ment with tower estimates was caused by the model predicting a similar seasonality of  
412 water flux at both control and burned forests, whereas towers suggest an increase in wa-  
413 ter flux during the earlier part of the dry season (Figure S6). ED-2.2 predictions of sen-  
414 sible heat flux had high correlation with observations at all sites (Figures 4b and 4d; Ta-  
415 ble S1), although sensible heat flux shows significant biases at BTE, and dampened sea-  
416 sonality at GYF and TAN (Burned) (Figures 4a and 4c; Table S1; Figure S6). Outgo-  
417 ing shortwave radiation correctly captured the seasonality at the wettest sites, but it did  
418 not capture the sharp dry-season increase at TAN (Figure S8), which may be associated  
419 with dry-season leaf senescence and shedding that was likely underestimated by ED-2.2.  
420 In addition, ED-2.2 simulations overestimated outgoing longwave radiation at all sites  
421 except at TAN (Burned) using inventory initialization (Figure S9). Nonetheless, the sea-  
422 sonality and the intra-seasonal variation of outgoing longwave radiation were correctly  
423 captured by ED-2.2, resulting in generally high correlation and small standard devia-  
424 tion of residuals at most sites (Figure 4; Table S1).

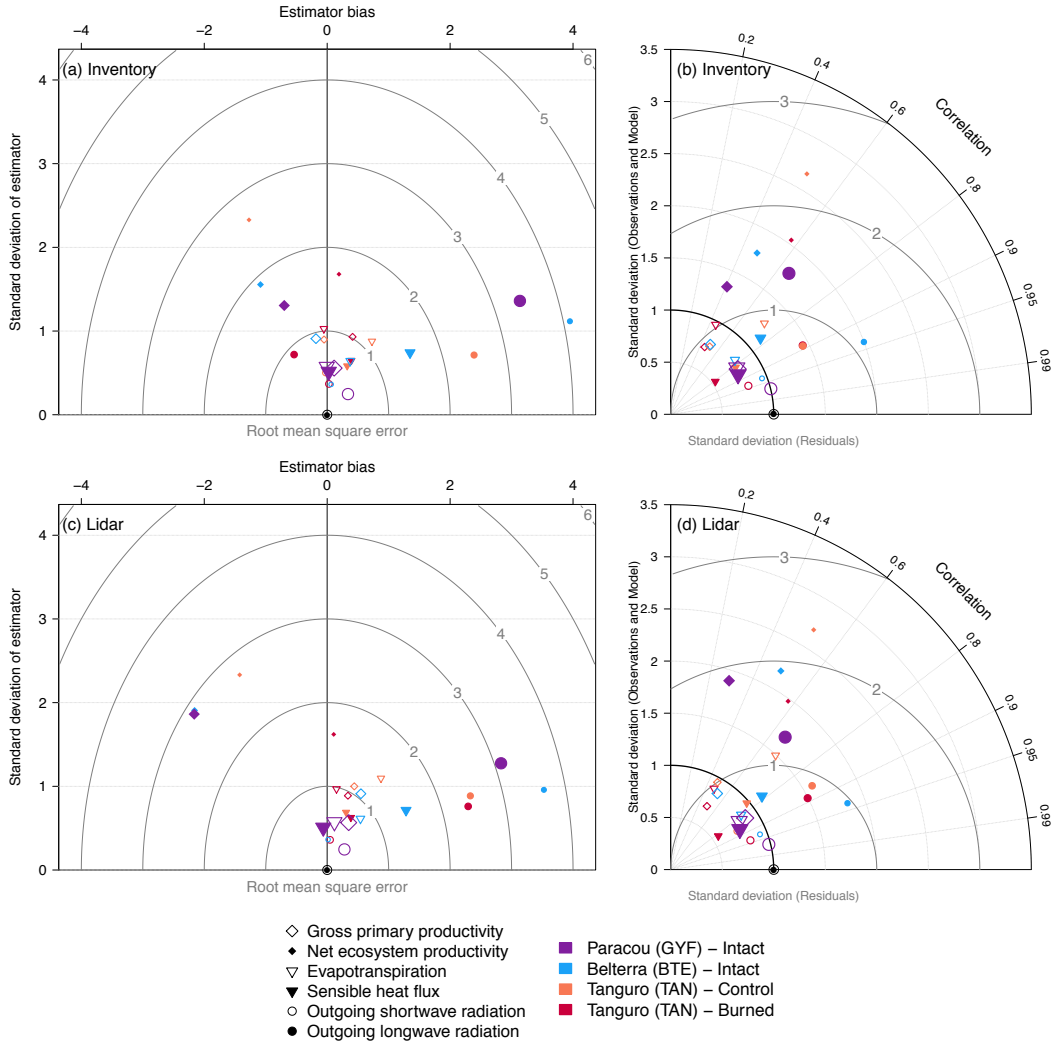


**Figure 4.** Summary of ED-2.2 model assessment using eddy covariance towers as benchmarks, using simulations initialized with forest inventory and airborne lidar. (a,c) Bias-variance diagram and (b,d) Taylor diagram of multiple daily-averaged fluxes of carbon, energy, and water for Paracou (GYF), Belterra (BTE) and Tanguro (TAN, control and burned), for simulations initialized with (a,b) forest inventory plots and (c,d) airborne lidar. In the bias-variance diagram, bias ( $x$  axis), standard deviation of residuals ( $y$  axis) and root mean square error (concentric arcs) are normalized by the standard deviation of observations, as is the standard deviation of models in the Taylor diagram. In both diagrams,  $\odot$  corresponds to the perfect model prediction. In all plots, we only compare daily averages of days with no measurement gaps. Comparisons of the seasonal cycle for all variables included in the diagrams are available at Figures S4-S9.

### 3.2 Degradation effects on seasonality of fluxes

From ED-2.2, we found that forest degradation can have substantial impacts on the ecosystem function such as evapotranspiration (ET) or ground temperature in severely or recently degraded forests, and in parts of the Amazon with a longer dry season. At GYF, the airborne lidar survey sampled only intact forests and areas that were logged 25 years prior to the data acquisition: consequently, the average water vapor flux and ground temperature were nearly indistinguishable across degraded and intact forests (Figures 5a, S10a). At the equatorial sites, degradation effects were small during the wet season but showed marked reduction in ET (2.1–6.7% in BTE and 4.3–31.8% in PRG) and increase in daytime temperature (0.4–0.9°C in BTE and 1.0–6.0°C in PRG) during the dry season, with the largest changes relative to intact forests found at burned areas (Figures 5b, 5c, S10b,c). At the southern (driest) sites, the seasonal changes were even more pronounced: at both FZN and TAN, ET decreased by 21–25% early in the dry season (Jun) at the most severely burned forests, whereas ET in intact forests peaked in the middle of the dry season (Jul–Aug; Figures 5d and 5e). Similarly, burned forests were warmer year-round than intact forests at the southern sites (FZN and TAN), with minimum warming during the wet season (Dec–Mar; 0.5–0.8°C), and maximum warming occurring at the peak of the dry season (Jul–Aug; 1.0–6.5°C; Figures S10d and S10e).

Importantly, the ED-2.2 results in Figures 5 and S10 emerge from the different distribution of forest structures associated with degradation histories. ED-2.2 accounts for the diversity of forest structures within each disturbance history by means of patches; each patch represents a different forest structure found within any disturbance regime, and patch area is proportional to the probability of finding such forest structure (Longo, Knox, Medvigy, et al., 2019). For example, the ground temperature is consistently warmer at the low biomass patches, but the differences between the lowest and highest patch temperatures are as low as 1°C at GYF (Figure 6a) and less than 4°C during the wet season even at the southern regions (Figures 6d and 6e). In contrast, differences along biomass gradients exceed 9°C during the dry season at all regions except GYF (Figure 6).

Likewise, when all simulated patches are considered, we observe strong coherence between biomass and gross primary productivity (GPP) across all regions and throughout the year (Figures 7 and S11). However, the effect of local communities on GPP is seasonal: differences in typical GPP between low-biomass and high-biomass patches do

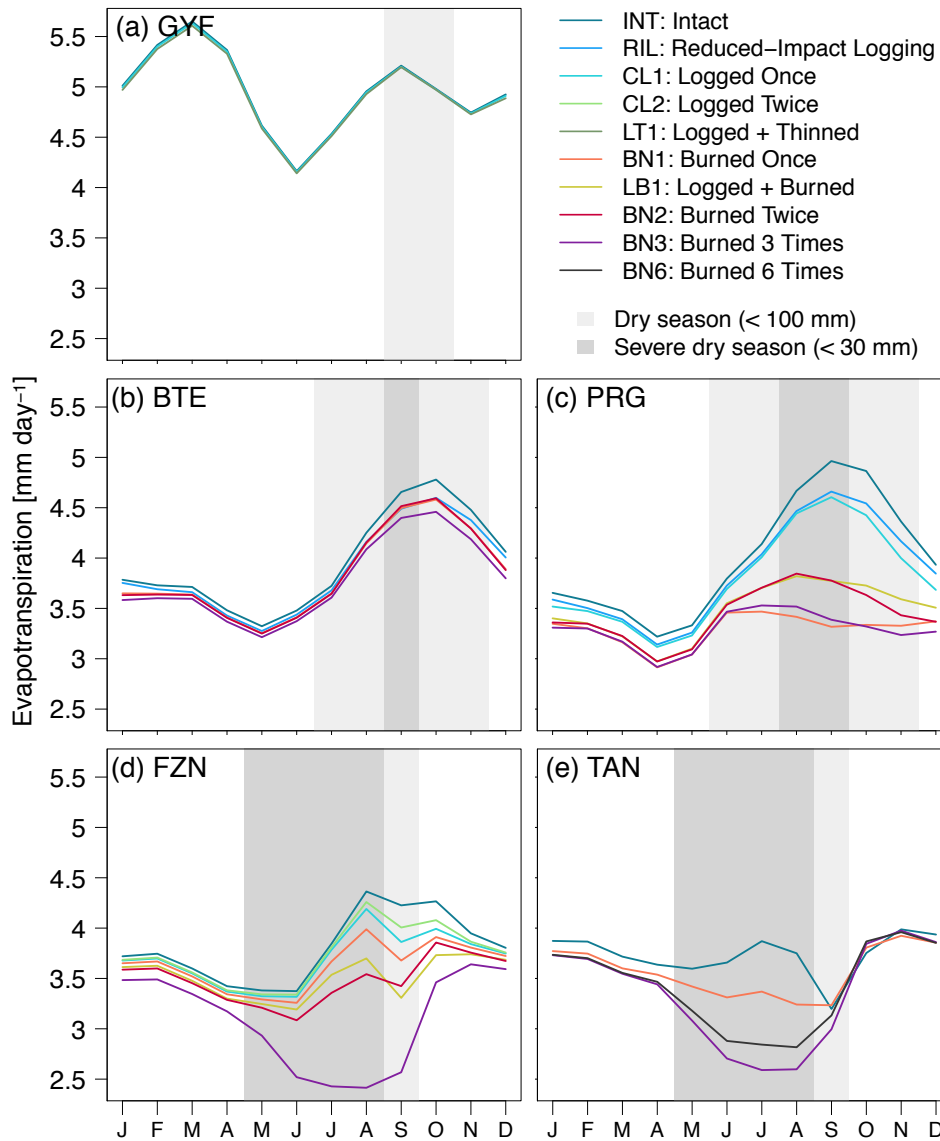


**Figure 5.** Monthly mean evapotranspiration (ET) as a function of region and degradation. Monthly averages correspond to the 1980–2016 period, simulated by ED-2.2 for (a) Paracou (GYF), (b) Belterra (BTE), (c) Paragominas (PRG), (d) Feliz Natal (FZN), and (e) Tanguro (TAN), aggregated by degradation history within each region (lines). Grey rectangles in the background correspond to the average dry season.

457 not exceed  $1.1 \text{ kgC m}^{-2} \text{ yr}^{-1}$  during the wettest months (Figures 7a–7c), whereas the range  
 458 of GPP reaches  $0.7 \text{ kgC m}^{-2} \text{ yr}^{-1}$  at the short dry-season at GYF and exceeds  $2.0 \text{ kgC m}^{-2} \text{ yr}^{-1}$   
 459 during the dry season at the most degraded and driest sites (Figures 7e and 7f). Sim-

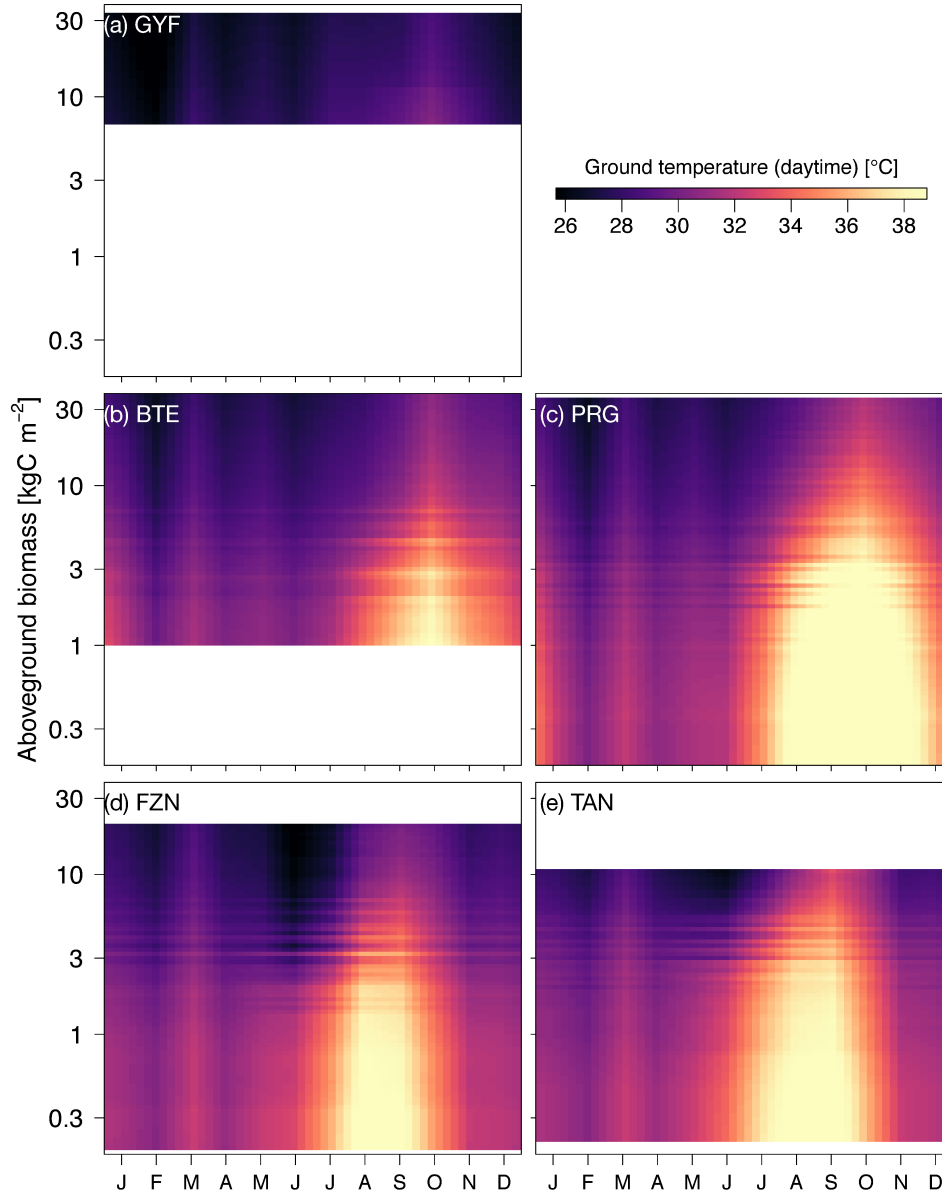


**Figure 6.** Monthly mean daytime ground temperature as a function of region and local (patch) aboveground biomass. Monthly averages correspond to the 1980–2016 period, simulated by ED-2.2 for (a) Paracou (GYF), (b) Belterra (BTE), (c) Paragominas (PRG), (d) Feliz Natal (FZN), and (e) Tanguro (TAN), and the y axis corresponds to the aboveground biomass for each patch, linearly interpolated for visualization. White areas are outside the range of biomass of each region and thus excluded.

460 ilar effects were observed in evapotranspiration, where differences along biomass are the  
 461 strongest during the dry season (Figure S12).

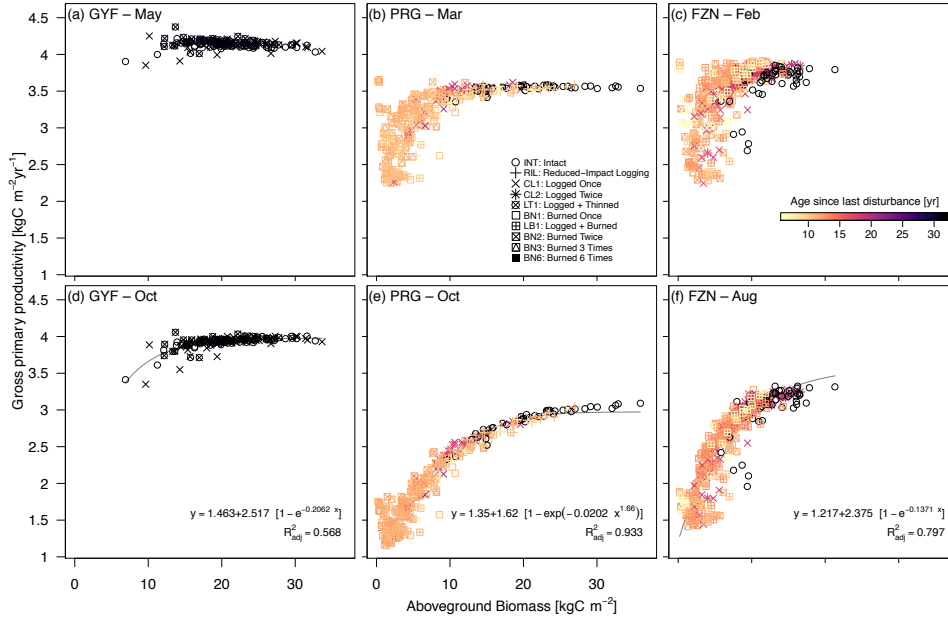


**Figure 7.** Variability of gross primary productivity (GPP) as a function of local (patch) aboveground biomass (AGB). Scatter plot of AGB ( $x$  axis) and GPP ( $y$  axis) at sites (a,d) Paracou (GYF), (b,e) Paragominas (PRG), (c,f) Feliz Natal (FZN), for (a-c) the peak of wet season — May (GYF), March (PRG), and February (FZN) — and (d-f) peak of dry season — October (GYF and PRG), and August (FZN). Each point represents the 1980–2016 average GPP of each patch solved by ED-2.2; point shapes correspond to the disturbance history, and point colors represent the time between the last disturbance (undetermined for intact forests) and lidar data acquisition. Curves correspond to non-linear least squares fits of the most parsimonious function, defined from Bayesian Information Criterion (Schwarz, 1978), between shifted exponential or shifted Weibull functions. Only fits that produced  $R_{adj}^2 > 0.5$  were included.

### 3.3 Degradation impacts on forest flammability

The impact of forest degradation on ecosystem functioning showed important year-to-year variability, and differences between intact and degraded forests were generally larger during typical years than during extreme droughts. For this section, we calculate the monthly water deficit based on the difference between potential evapotranspiration (calculated following Priestley & Taylor, 1972) and rainfall, and relate the 12-month running averages of multiple response variables with the maximum cumulative water deficit over the previous 12 months, and define drought length as the number of consecutive months in water deficit exceeds 20 mm. Using region PRG as an example, as the region has the

471 broadest range of recent disturbances and maximum cumulative water deficit, we found  
472 that, during typical rainfall periods, evapotranspiration in logged forests and burned forests  
473 were 3–6% and 11–22% lower than intact forests, respectively (Figure 8a); this differ-  
474 ence was significantly reduced or even reversed during severe droughts, when evapotran-  
475 spiration of degraded forests were up to 4% higher than in intact forests (Figure 8a). De-  
476 graded forests have a lower proportion of shade-tolerant, late-successional trees, and typ-  
477 ical stomatal conductance is higher by 19–34% in burned forests and by 5–13% in logged  
478 forests (Figure 8b). This result indicates that the reduced typical evapotranspiration re-  
479 sults from degraded forests having lower leaf area index relative to intact forests, as lo-  
480 cal leaf area index is related to local aboveground biomass (Figure S13). In addition, ex-  
481 treme droughts did not substantially reduce the differences in stomatal conductance be-  
482 tween degraded and intact forests (Figure 8b). While evapotranspiration was generally  
483 lower in degraded forests, total evaporation (from ground and canopy intercepted wa-  
484 ter) was higher in most degraded forests, with burned forests experiencing 3–26% more  
485 evaporation in typical years and 0–14% during severe droughts (Figure 8c). The com-  
486 bination of higher evaporation and relatively shorter canopy (shallower roots) in degraded  
487 forests were typically translated into slightly drier near-surface soils (Figure 8d): dur-  
488 ing typical years, soil water availability at the top 30 cm layers was 1.2–12% lower in burned  
489 forests than intact forests, whereas the differences were more modest in logged forests  
490 (0.2–3%) and even reversed during extreme droughts (Figure 8d). Carbon and energy  
491 fluxes showed similar behavior. Gross primary productivity in intact forests steadily de-  
492 creased with increased drought severity, and the depletion of productivity caused by degra-  
493 dation is most marked during typical years but is reduced during severe droughts (Fig-  
494 ure S14a). While ground temperature is always higher in degraded forests (Figure S14b),  
495 differences in sensible heat fluxes and outgoing longwave radiation also diminish during  
496 extreme drought conditions (Figure S14c,d).

497 Degraded forests show drier near-surface soils (Figure 8d) and warmer surface tem-  
498 peratures (Figure S14) than intact forests for most years, yet the interannual variabil-  
499 ity of climate also modulates the differences in water, carbon, and energy cycles between  
500 degraded and intact forests (Figures 8 and S14). Therefore, both degradation and cli-  
501 mate may influence the flammability of forests. The average flammable area predicted  
502 by ED-2.2 (Section 2.4) shows large variation across regions, ranging from nearly zero  
503 at GYF forests (the wettest region) to over 25% yr<sup>-1</sup> at some of the forests in TAN (the

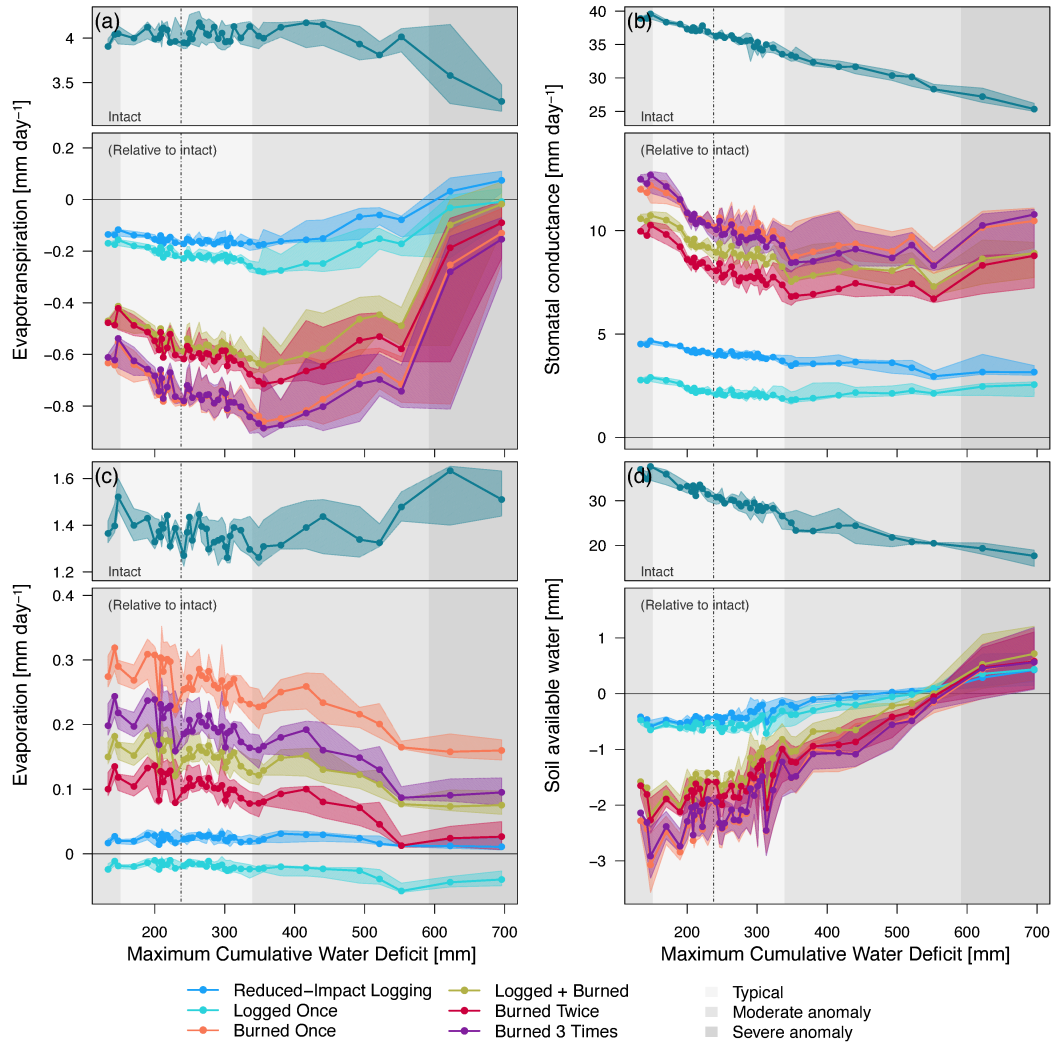


**Figure 8.** Response of the water cycle components across a forest degradation gradient and drought severity in Paragominas (PRG). Selected components: (a) Total water vapor flux, (b) stomatal conductance, averaged by leaf area, (c) evaporation, and (d) soil available water (i.e. in excess of permanent wilting point) of the top 30 cm. Points correspond to the median value of 12-month running averages, aggregated into 40 quantiles along the range of maximum cumulative water deficit (MCWD). Bands around the points correspond to the 95% range within each MCWD bin. Top panels are the absolute value for intact forests, and bottom panels are the absolute difference between degraded and intact forests. Background shades denote the MCWD anomaly: light gray – 68% range around the median (dot-dash vertical line); intermediate gray – 95% range; dark gray – anomalies exceeding the 95% range.

504 driest region) (Figure 9a). Within each region (i.e. under the same prescribed climate),  
505 the model generally predicted higher flammability for the shortest forests ( $< 10$  m), al-  
506 though predictions also indicate large within-region variability of flammable area for forests  
507 with intermediate canopy height (10–25 m) (Figure 9a). For most forests, flammable con-  
508 ditions were predicted mostly during moderate or severe droughts, regardless of the degra-  
509 dation history, as exemplified by region PRG (Figure 9b). While the time series of flammable  
510 area were synchronized across degradation types, ED-2.2 predictions of flammable area  
511 were generally higher for burned forests than intact or lightly logged forests (Figures 9b  
512 and S15). The one exception was the driest region (TAN), where forests that burned mul-  
513 tiple times experienced lower flammability than intact forests (Figure S15d); at TAN,  
514 even intact forests were relatively short (Figure 9a), which caused ED-2.2 to predict lim-  
515 ited access to deeper soils and increased desiccation.

## 516 **4 Discussion**

### 517 **4.1 Initialization of forest structure from remote sensing**

518 Our method to derive the vertical structure of the canopy from high-resolution air-  
519 borne lidar successfully characterized the diversity of forest structures of the Amazon,  
520 captured differences in forest structure variability along a precipitation gradient, and de-  
521 scribed the within-region variability in forest structure caused by forest degradation (Fig-  
522 ures 3 and S2-S3). Previous studies have used forest structure derived from remote-sensing  
523 data to initialize vegetation demography models in tropical forests (e.g., Hurtt et al., 2004;  
524 Antonarakis et al., 2011; Rödig et al., 2018). However, these studies often assume a re-  
525 lationship between forest structure and canopy height with stand age. While this assump-  
526 tion has been successfully applied to intact and second-growth tropical forests (Hurtt  
527 et al., 2004; Antonarakis et al., 2011), the association between forest structure and suc-  
528 cession is unlikely to be preserved in degraded forests. For example, understory fires pro-  
529 portionally kill more smaller trees than large trees (Uhl & Kauffman, 1990; Brando et  
530 al., 2012; Silva et al., 2018), and selectively logging creates complex mosaics of forest struc-  
531 ture, with substantial losses of large trees from harvesting, and extensive damage to smaller  
532 trees in skid trails (Feldpausch et al., 2005). In contrast, our approach accounts for the  
533 entire vertical profile at local (50-m) scale, similarly to Antonarakis et al. (2014), which  
534 does not require any assumption on the successional stage of the forest. Importantly, our  
535 approach requires only the vertical distribution of returns, and could be adapted to large-

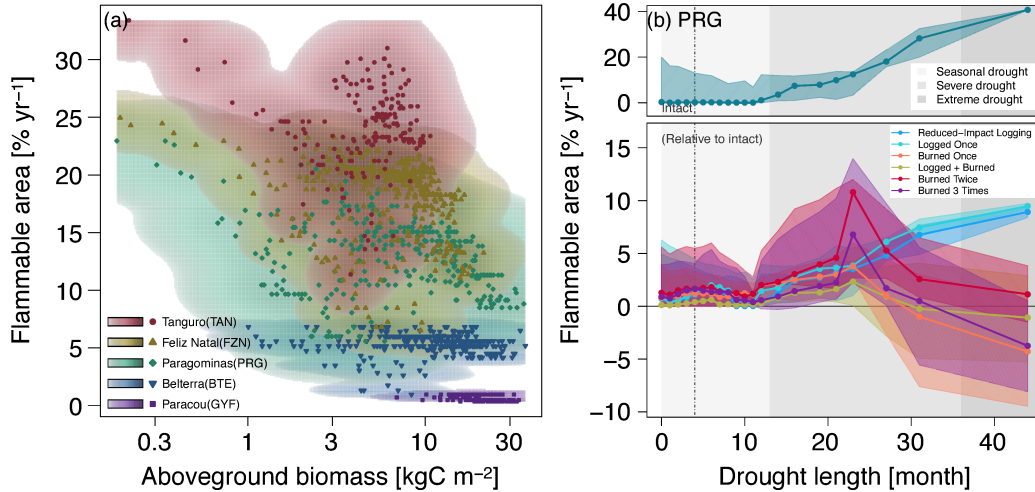


**Figure 9.** Average flammability as functions of degradation and climate variability. (a) Scatter plot shows the average flammable area (1980–2016) for each simulated patch across all regions, as a function of canopy height. Density cloud (background color) was produced through a bi-dimensional kernel density estimator; points are the averages used to generate each density cloud. Color ramps (logarithmic) range from 0.1 – 100% of the maximum computed scale. (b) Flammable area at region PRG, as a function of degradation history and drought length (number of consecutive months with water deficit in excess of 20 mm). Points correspond to the median value of 12-month running averages, aggregated into quantiles along the drought length. Bands around the points correspond to the 95% range within each drought length bin. Top panels are the absolute value for intact forests, and bottom panels are the absolute difference between degraded and intact forests. Background shades denote drought-length classes used in the text: seasonal (light gray, less than 12 months); severe (intermediate gray, 12–36 months); extreme (dark gray; more than 36 months). Flammability response to degradation and drought duration for other regions are shown in Figure S15.

536 footprint, airborne or spaceborne lidar data, including the NASA’s Global Ecosystem  
 537 Dynamics Investigation (GEDI, Hancock et al., 2019).

538 We demonstrated that the initialization from airborne lidar profiles captures most  
 539 of the variability across and within regions, yet it has important assumptions and lim-  
 540 itations. First, our approach relies on allometric equations to determine both the diam-  
 541 eter at breast height (DBH), and the individual leaf area ( $L_i$ , Text S3.3). These equa-  
 542 tions have either large uncertainties (DBH) or limited number of samples (Figure S16).

543 The use of allometric equations that account for regional variation (e.g., Feldpausch et  
544 al., 2011, 2012), and the expansion of open-source databases, such as the Biomass And  
545 Allometry Database (BAAD, Falster et al., 2015) used in our study, could further im-  
546 prove the characterization of the vertical structure. In addition, the increased availabil-  
547 ity of terrestrial laser scanning (TLS) and high-resolution, low-altitude unmanned aerial  
548 vehicle lidar could substantially increase the data availability and thus improve the over-  
549 all quality of allometric equations (Calders et al., 2015; Stovall et al., 2018; Schneider  
550 et al., 2019). Alternatively, techniques that extract individual tree crowns from lidar point  
551 clouds readily provide highly accurate local stem density and local size-frequency dis-  
552 tributions (e.g., tree height or crown size; Ferraz et al., 2016). These distributions can  
553 be used to attribute DBH to individuals and generate initial conditions akin to forest  
554 inventory to the ED-2.2 model, and data-model fusion techniques that leverage the grow-  
555 ing availability of data could reduce uncertainties on many model parameters, includ-  
556 ing allometry (F. J. Fischer et al., 2019). Finally, ED-2.2 overestimated the seasonality  
557 of gross primary productivity and evapotranspiration at the driest region (TAN) (Fig-  
558 ures S4 and S6). This result suggests that simulated rooting depth for TAN was under-  
559 estimated in the model. Rooting profiles in tropical forests remain largely uncertain: some  
560 site studies have sought to relate individual tree size with rooting depth using isotopic  
561 measurements (e.g., Stahl et al., 2013; Brum et al., 2019), whereas regional studies that  
562 provide spatial distribution of rooting depth still show important discrepancies in the  
563 tropics (e.g., Yang et al., 2016; Fan et al., 2017). Constraining the below-ground allo-  
564 cation of tropical ecosystems should be a priority in future studies.

565 In our study we inferred the functional diversity from forest structure obtained from  
566 existing forest inventory plots. The functional group attribution captured the general  
567 characteristics of functional composition along degradation gradients (Figure S1), includ-  
568 ing the more frequent occurrence of early-successional individuals in degraded forests,  
569 consistent with field-based studies (Both et al., 2019); nonetheless, uncertainties in func-  
570 tional attribution from field measurements are high. The increased availability of coor-  
571 dinated airborne laser scanning (ALS) and airborne imaging spectroscopy (AIS) data  
572 in mid-latitudes has lead to opportunities to link structural variability with functional  
573 diversity (e.g., Antonarakis et al., 2014; Schneider et al., 2017), and previous studies have  
574 successfully integrated ALS and AIS data to attribute functional groups in the ED-2 model  
575 (e.g., Antonarakis et al., 2014; Bogan et al., 2019). Overlapping ALS and AIS data over

576 tropical forests are becoming increasingly common (Asner et al., 2014; de Almeida et al.,  
577 2019; Laybros et al., 2019) and could provide new opportunities to reduce uncertainties  
578 in functional attribution in future studies. Likewise, ongoing and upcoming spaceborne  
579 missions at the International Space Station such as GEDI (Hancock et al., 2019), and  
580 the Hyperspectral Imaging Suite (HISUI, Matsunaga et al., 2017) will allow for large-  
581 scale characterization of structure and function of ecosystems at global scale (Stavros  
582 et al., 2017; Schimel et al., 2019).

## 583 **4.2 Degradation impacts on ecosystem functioning**

584 In addition to carbon losses and structural changes, degradation has substantial  
585 impacts on energy and water cycles in Amazonian forests, especially in severely degraded  
586 forests with marked dry season. According to the ED-2.2 simulations, ground temper-  
587 ature of logged forests ranged from nearly-identical to intact forests (low-impact logging  
588 or old logging disturbances) to 0.7°C warmer (recently logged forests), whereas severely  
589 burned forests experienced daytime near-surface temperatures increases of as much as  
590 4°C (Figure S10), and differences between the lowest and highest biomass patches ex-  
591 ceeded 9°C (Figure 6). Observed differences in understory temperatures show large vari-  
592 ability, but they generally agree with the ED-2.2 results. For example, results of tem-  
593 perature differences between logged and intact areas in the wet forests of Sabah, Malaysia,  
594 ranged from negligible to 1.2°C for average maximum temperature (Senior et al., 2018;  
595 Jucker et al., 2018). The predicted warmer daytime understory temperatures at recur-  
596 rently burned forests also yielded drier near-surface conditions: daytime ground vapor  
597 pressure deficit was on average 15–25 hPa greater than in intact forests (equivalent to  
598 5–15% reduction in relative humidity), which is within the range observed after the most  
599 damaging experimental fire at TAN in 2007 (Brando et al., 2014), and similar to differ-  
600 ences in understory relative humidity reported in the dry season between open-canopy  
601 seasonally flooded forests and closed-canopy upland forests in the Central Amazon (de  
602 Resende et al., 2014).

603 ED-2.2 showed various degrees of agreement with the few existing observational  
604 studies comparing changes in evapotranspiration due to degradation. Evapotranspira-  
605 tion response to reduced-impact logging was minor (–1.9% reduction relative to intact  
606 in BTE), consistent with eddy covariance tower estimates in a logging experiment in the  
607 same region (–3.7% reduction after accounting for site differences and interannual vari-

608 ability, S. D. Miller et al., 2011). The model results for the experimental fire at TAN,  
609 however, suggested similar wet-season ET between burned and intact forests ( $\Delta ET =$   
610  $ET_{\text{Brn}} - ET_{\text{Int}} = 0.002 \text{ mm day}^{-1}$ ), with stronger depletion of ET in burned forests  
611 during the dry season ( $\Delta ET = -0.31 \text{ mm day}^{-1}$ ) (Figures 5 and S6). In contrast, Brando,  
612 Silvério, et al. (2019) found higher ET in burned forests over a period of 4 years, albeit  
613  $\Delta ET$  also showed significant interannual variability. A few other studies suggest that the  
614 significant decline in dry-season ET in burned forests may be expected in some areas:  
615 for example, Hirano et al. (2015) found that evapotranspiration of drained and burned  
616 peatlands with second-growth vegetation in Central Kalimantan (Indonesia) was  $0.43 \text{ mm day}^{-1}$   
617 lower than drained forests; Quesada et al. (2004) inferred ET changes from soil water  
618 budget in savannas and found significant reductions following fires in a savanna site in  
619 Central Brazil. The advent of high-resolution remote sensing products that quantify en-  
620 ergy, water, and carbon fluxes, such as the ECOSystem Spaceborne Thermal Radiome-  
621 ter Experiment on Space Station (ECOSTRESS) and the Orbiting Carbon Observatory  
622 3 (OCO-3), will provide new opportunities to quantify the role of tropical forest degra-  
623 dation on ecosystem functioning at regional scale (Schimel et al., 2019), as well as to pro-  
624 vide new benchmark data for ecosystem models.

625 Our model results indicate that severe degradation substantially alters the mag-  
626 nitude and seasonality of energy, water, and carbon fluxes (Figures 5-7 and S10-S12).  
627 In our study, we disabled the vegetation dynamics in ED-2.2 to ensure that predicted  
628 differences in ecosystem functioning could be unequivocally attributed to structural di-  
629 versity, but the differences in ecosystem functioning between degraded and intact forests  
630 may diminish over time as the forest recovers from previous disturbance. This pathway  
631 is consistent with the relatively small differences in ET and surface temperature (Fig-  
632 ures 5-6) observed at logged forests at GYF (25 years since last disturbance) and burned  
633 forests at BTE (15 years since last disturbance). However, the recovery trajectory is one  
634 out of multiple possible pathways: degraded forests may be more prone to subsequent  
635 disturbances (Silvério et al., 2019; Hérault & Piponirot, 2018); the recovery dynamics can  
636 be long or not attainable if multiple stable states exist or if succession is arrested (Mesquita  
637 et al., 2015; Ghazoul & Chazdon, 2017), potentially prolonging the impacts of forest degra-  
638 dation on energy and water cycles; and feedbacks on precipitation caused by degrada-  
639 tion could affect the spatial distribution of rainfall similarly to the effect observed with

640 deforestation (Spracklen et al., 2018), although to our knowledge this impact has not yet  
641 been quantified for degraded forests.

### 642 **4.3 Interactions between forest degradation and climate variability**

643 The predicted reductions in evapotranspiration (ET) in the most degraded areas  
644 during the dry season suggest that land-use change impacts on the water cycle may be  
645 more widespread and pervasive than indicated by earlier studies. Previous model-based  
646 studies showed that biome-wide deforestation could cause ET to decrease by 25–40% rel-  
647 ative to intact forests in the Amazon during the dry season (e.g., von Randow et al., 2004;  
648 Zemp et al., 2017). These reductions are comparable to the ET reductions predicted by  
649 ED-2.2 at the most degraded forests (21–32%, Figure 5). Because tropical forest degra-  
650 dation affects an area comparable to deforestation in the Amazon (Tyukavina et al., 2017),  
651 it may further reduce the strength of the Amazon water vapor source to the atmosphere.  
652 In our study, we focused on understanding how climate and structure variability impacts  
653 the water and energy fluxes, but degradation-driven changes in these fluxes are likely to  
654 feed back into the atmosphere. For example, changes in evapotranspiration and sensi-  
655 ble heat flux associated with deforestation are known to either redistribute or reduce to-  
656 tal rainfall in tropical forests (Spracklen et al., 2018, and references therein), and a sub-  
657 stantial fraction of South American precipitation water comes from evapotranspiration  
658 from Amazonian forests (van der Ent et al., 2010). Recent estimates of ET for the Ama-  
659 zon Basin from the Gravity Recovery and Climate Experiment (GRACE) suggest that  
660 the basin-wide ET (including intact forests) has decreased by 1.7% between 2002 and  
661 2015 (Swann & Koven, 2017). In addition, several studies suggest that the dry season  
662 in the Amazon is becoming longer (Fu et al., 2013; Sena et al., 2018), and land use change  
663 is one of the main drivers of the drying trend (Barkhordarian et al., 2018). The role of  
664 forest degradation on ongoing and future changes in climate across the Amazon remains  
665 uncertain and deserves further investigation, potentially with coupled biosphere-atmosphere  
666 models that represent heterogeneity in forest structure and functioning (Swann et al.,  
667 2015; Knox et al., 2015; Wu et al., 2017).

668 Our results show that structural changes resulting from forest degradation make  
669 the forest surface drier and warmer (Figures 5-8 and S10). Drier and warmer conditions  
670 near the surface increase flammability (Brando, Paolucci, et al., 2019, and references therein),  
671 and it has been long suggested that forest degradation and canopy opening make forests

672 more likely to burn (e.g., Uhl & Buschbacher, 1985; Cochrane et al., 1999; Ray et al.,  
673 2005; A. A. C. Alencar et al., 2015). The ED-2.2 simulations indeed predicted higher flamma-  
674 bility in degraded (more open-canopy) forests on any given year (Figures 9 and S15). How-  
675 ever, our results also suggest that climate strongly drives the variability of flammable  
676 area across most of our study regions (Figures 9b and S15), which is consistent with the  
677 significant increases in forest fires in the Amazon during extreme drought years (Morton  
678 et al., 2013; Aragão et al., 2018). Moreover, our results indicate that differences in flammable  
679 area between intact and degraded forests are reduced or even reversed during extreme  
680 droughts, which indicates that under extreme conditions, the level of degradation is less  
681 critical to create flammable conditions. This effect was predicted for most years at TAN,  
682 which typically experiences severe and longer dry seasons compared to the other study  
683 regions (Figure S15).

684 Previous studies suggest that parts of the Eastern Amazon could become drier by  
685 the end of the century and experience more extreme events, including droughts (IPCC,  
686 2014; Duffy et al., 2015), and thus potentially more susceptible to future fires (De Faria  
687 et al., 2017; Brando et al., 2020). However, how tropical forest flammability will respond  
688 in the long-term to ongoing changes in climate and land use is still uncertain, and re-  
689 cent studies have shown that either climate (Le Page et al., 2017) or land use (Fonseca  
690 et al., 2019) could be dominant on predicted shifts in fire regime. Importantly, while our  
691 analysis focused on flammability, and ED-2.2 fire model captures the general patterns  
692 of fire disturbance across the Amazon (Longo, Knox, Levine, et al., 2019), it does not  
693 represent many mechanisms and processes that are critical to describe fire dynamics in  
694 tropical forests, such as anthropogenic ignitions, diurnal cycle of fire intensity, and fire  
695 termination, therefore we could not quantify the effects of fire on further forest degra-  
696 dation. The use of process-based fire disturbance models within the ED-2.2 (e.g., Thon-  
697 icke et al., 2010; Le Page et al., 2015) framework could contribute to further improve our  
698 understanding of interactions between forest degradation, climate, and flammability across  
699 the Amazon.

## 700 **5 Conclusion**

701 Our study showed that tropical forest degradation can markedly modify the ecosys-  
702 tem functioning in the Amazon, with substantial reductions in evapotranspiration (ET)  
703 and gross primary productivity (GPP), and increase in surface temperature (Figures 5-

8). Within the regions included in our study, the effects of degradation on energy, water, and carbon cycles were the strongest in the Eastern and Southern Amazon, where the dry season is more pronounced. Notably, in areas where severe forest degradation resulted in substantial changes in forest structure, reductions in dry-season evapotranspiration are similar to those found in deforested areas (Figure 5; von Randow et al., 2004). The area of the Amazon forest impacted by degradation is comparable to the deforested area (Asner et al., 2005; Morton et al., 2013; Souza Jr. et al., 2013; Tyukavina et al., 2017), and thus degradation-driven changes in water, energy, and carbon cycles are potentially important. However, the extent to which degradation affects the biophysical and biogeochemical cycles at regional scale ultimately depends on (1) annual degradation rates; (2) recovery time of degraded forests; and (3) the likelihood that degraded forests are cleared. For example, (Brando, Silvério, et al., 2019) found that ET in burned forests was indistinguishable from intact forests 7 years after the last fire. While their result suggests fast recovery of degraded forests, the impacts of degradation on ET can still be regionally relevant if degradation rates are sufficiently high to maintain low average age since last disturbance in degraded forests. Moreover, we found that the impacts of tropical forest degradation on energy, water, and carbon cycles and on flammability are more pronounced during typical years than during extreme droughts (when all forests become flammable), which highlights the complex interactions between climate and forest structure. To understand and reduce uncertainties of climate-structure interactions, it would be valuable to leverage the recent advances in remote sensing of forest structure, including the recently launched GEDI mission (Hancock et al., 2019), and terrestrial biosphere models that can represent complex and heterogeneous ecosystems (Fisher et al., 2018). Our study, while focusing on airborne lidar data, has demonstrated the opportunities to integrate remote sensing and terrestrial biosphere models even in regions with complex forest structure such as degraded forests.

## Acknowledgments

Airborne lidar and forest inventory data were obtained from Sustainable Landscapes Brazil (2019), dos-Santos et al. (2019) (Brazil) and Paracou Portal (2016) (French Guiana). MERRA-2 reanalyses are available from GMAO (2015a, 2015b, 2015c, 2015d) and MSWEP-2.2 data were downloaded from <http://www.gloh2o.org>. The ED-2.2 model used in this study is available at Longo et al. (2019) and the scripts and ED-2.2 output are perma-

736 nently stored at Longo et al. (2020). Trait data are available at the TRY initiative on  
737 plant traits (<http://www.try-db.org>), request 2751; at Gu et al. (2016); or as support-  
738 ing information from the cited references (I. J. Wright et al., 2004; Santiago & Wright,  
739 2007; Bahar et al., 2017).

740 The research was carried out at the Jet Propulsion Laboratory, California Insti-  
741 tute of Technology, under a contract with the National Aeronautics and Space Admin-  
742 istration (80NM0018D004), and supported by NASA Earth Sciences grant (NNH16ZDA001N-  
743 IDS). Data recorded at the Guyaflux tower were obtained thanks to the support of two  
744 *Investissement d'avenir* grants from the Agence Nationale de la Recherche (CEBA, ref  
745 ANR-10-LABX-25-01; ARBRE, ref. ANR-11-LABX-0002-01). Data in Brazil were ac-  
746 quired by the Sustainable Landscapes Brazil project supported by the Brazilian Agri-  
747 cultural Research Corporation (EMBRAPA), the U.S. Forest Service, and USAID, and  
748 the U.S. Department of State. The study has been supported by the TRY initiative on  
749 plant traits, which is hosted, developed and maintained by J. Kattge and G. Bönisch (Max  
750 Planck Institute for Biogeochemistry, Jena, Germany). TRY is currently supported by  
751 DIVERSITAS/Future Earth and the German Centre for Integrative Biodiversity Research  
752 (iDiv) Halle-Jena-Leipzig.

753 We thank Xiangtao Xu for sharing the trait plasticity algorithm and discussions  
754 on model results; Divino Silvério for processing and sharing the data from Tanguro; Hylke  
755 Beck for sharing the MSWEP-2.2 data; and Marcos Scaranello, Fabian Schneider, Alexan-  
756 dra Konings, and A. Anthony Bloom for discussions on the lidar initialization algorithm  
757 and interpretation of model results. The model simulations were carried out at the Odyssey  
758 cluster, supported by the FAS Division of Science, Research Computing Group at Har-  
759 vard University; and at the Brazilian National Laboratory for Scientific Computing (LNCC).  
760 M.L. was supported by the São Paulo State Research Foundation (FAPESP, 2015/07227-  
761 6) and by the NASA Postdoctoral Program, administered by Universities Space Research  
762 Association under contract with NASA. M.K. was supported in part by the Next Gen-  
763 eration Ecosystem Experiments-Tropics, funded by the U.S. Department of Energy, Of-  
764 fice of Science, Office of Biological and Environmental Research.

## 765 **References**

766 Achard, F., Beuchle, R., Mayaux, P., Stibig, H.-J., Bodart, C., Brink, A., . . . Simon-

- 767 etti, D. (2014, Aug). Determination of tropical deforestation rates and related  
768 carbon losses from 1990 to 2010. *Glob. Change Biol.*, *20*(8), 2540–2554. doi:  
769 10.1111/gcb.12605
- 770 Alamgir, M., Campbell, M. J., Turton, S. M., Pert, P. L., Edwards, W., & Laurance,  
771 W. F. (2016, Jul). Degraded tropical rain forests possess valuable carbon stor-  
772 age opportunities in a complex, forested landscape. *Sci. Rep.*, *6*(30012). doi:  
773 10.1038/srep30012
- 774 Alencar, A., Nepstad, D., & Vera Diaz, M. C. (2006, Feb). Forest understory fire in  
775 the Brazilian Amazon in ENSO and non-ENSO years: Area burned and com-  
776 mitted carbon emissions. *Earth Interact.*, *10*(6), 1–17. doi: 10.1175/EI150.1
- 777 Alencar, A. A. C., Brando, P. M., Asner, G. P., & Putz, F. E. (2015, Sep). Land-  
778 scape fragmentation, severe drought and the new Amazon forest fire regime.  
779 *Ecol. Appl.*, *25*(6), 1493–1505. doi: 10.1890/14-1528.1
- 780 Antonarakis, A. S., Munger, J. W., & Moorcroft, P. R. (2014, Jul). Imaging  
781 spectroscopy- and lidar-derived estimates of canopy composition and struc-  
782 ture to improve predictions of forest carbon fluxes and ecosystem dynamics.  
783 *Geophys. Res. Lett.*, *41*(7), 2535–2542. doi: 10.1002/2013GL058373
- 784 Antonarakis, A. S., Saatchi, S. S., Chazdon, R. L., & Moorcroft, P. R. (2011,  
785 Jun). Using lidar and radar measurements to constrain predictions of for-  
786 est ecosystem structure and function. *Ecol. Appl.*, *21*(4), 1120–1137. doi:  
787 10.1890/10-0274.1
- 788 Aragão, L. E. O. C., Anderson, L. O., Fonseca, M. G., Rosan, T. M., Vedovato,  
789 L. B., Wagner, F. H., ... Saatchi, S. (2018, Feb). 21<sup>st</sup> century drought-related  
790 fires counteract the decline of Amazon deforestation carbon emissions. *Nature*  
791 *Comm.*, *9*(1), 536. doi: 10.1038/s41467-017-02771-y
- 792 Aragão, L. E. O. C., Poulter, B., Barlow, J. B., Anderson, L. O., Malhi, Y., Saatchi,  
793 S., ... Gloor, E. (2014, Nov). Environmental change and the carbon balance  
794 of Amazonian forests. *Biol. Rev.*, *89*(4), 913–931. doi: 10.1111/brv.12088
- 795 Asner, G. P., Broadbent, E. N., Oliveira, P. J. C., Keller, M., Knapp, D. E., & Silva,  
796 J. N. M. (2006, Aug). Condition and fate of logged forests in the Brazil-  
797 ian Amazon. *Proc. Natl. Acad. Sci. U. S. A.*, *103*(34), 12947–12950. doi:  
798 10.1073/pnas.0604093103
- 799 Asner, G. P., Knapp, D. E., Broadbent, E. N., Oliveira, P. J. C., Keller, M., &

- 800 Silva, J. N. (2005, Oct). Selective logging in the Brazilian Amazon. *Science*,  
801 310(5747), 480–482. doi: 10.1126/science.1118051
- 802 Asner, G. P., Martin, R. E., Tupayachi, R., Anderson, C. B., Sinca, F., Carranza-  
803 Jiménez, L., & Martinez, P. (2014, Apr). Amazonian functional diversity from  
804 forest canopy chemical assembly. *Proc. Natl. Acad. Sci. U. S. A.*, 111(15),  
805 5604–5609. doi: 10.1073/pnas.1401181111
- 806 Asner, G. P., Powell, G. V. N., Mascaro, J., Knapp, D. E., Clark, J. K., Jacobson,  
807 J., ... Hughes, R. F. (2010, Sep). High-resolution forest carbon stocks and  
808 emissions in the Amazon. *Proc. Natl. Acad. Sci. U. S. A.*, 107(38), 16738-  
809 16742. doi: 10.1073/pnas.1004875107
- 810 Baccini, A., Walker, W., Carvalho, L., Farina, M., Sulla-Menashe, D., & Houghton,  
811 R. A. (2017, Oct). Tropical forests are a net carbon source based on above-  
812 ground measurements of gain and loss. *Science*, 358(6360), 230–234. doi:  
813 10.1126/science.aam5962
- 814 Bahar, N. H. A., Ishida, F. Y., Weerasinghe, L. K., Guerrieri, R., O’Sullivan, O. S.,  
815 Bloomfield, K. J., ... Atkin, O. K. (2017, May). Leaf-level photosynthetic ca-  
816 pacity in lowland Amazonian and high-elevation Andean tropical moist forests  
817 of Peru. *New Phytol.*, 214(3), 1002–1018. doi: 10.1111/nph.14079
- 818 Baraloto, C., Paine, C. E. T., Poorter, L., Beauchene, J., Bonal, D., Domen-  
819 ach, A.-M., ... Chave, J. (2010, Nov). Decoupled leaf and stem eco-  
820 nomics in rain forest trees. *Ecol. Lett.*, 13(11), 1338–1347. doi: 10.1111/  
821 j.1461-0248.2010.01517.x
- 822 Barkhordarian, A., von Storch, H., Behrangi, A., Loikith, P. C., Mechoso, C. R.,  
823 & Detzer, J. (2018, Jun). Simultaneous regional detection of land-  
824 use changes and elevated GHG levels: the case of spring precipitation in  
825 tropical South America. *Geophys. Res. Lett.*, 45(12), 6262–6271. doi:  
826 10.1029/2018GL078041
- 827 Barlow, J., Lennox, G. D., Ferreira, J., Berenguer, E., Lees, A. C., Mac Nally, R.,  
828 ... Gardner, T. A. (2016, Jul). Anthropogenic disturbance in tropical forests  
829 can double biodiversity loss from deforestation. *Nature*, 535, 144–147. doi:  
830 10.1038/nature18326
- 831 Beck, H. E., Wood, E. F., Pan, M., Fisher, C. K., Miralles, D. G., van Dijk, A. I.,  
832 ... Adler, R. F. (2019, Mar). MSWEP V2 global 3-hourly 0.1° precipitation:

- 833 methodology and quantitative assessment. *Bull. Am. Meteorol. Soc.*, *100*(3),  
834 473–500. doi: 10.1175/BAMS-D-17-0138.1
- 835 Berenguer, E., Ferreira, J., Gardner, T. A., Aragão, L. E. O. C., de Camargo, P. B.,  
836 Cerri, C. E., . . . Barlow, J. (2014, Dec). A large-scale field assessment of  
837 carbon stocks in human-modified tropical forests. *Glob. Change Biol.*, *20*(12),  
838 3713–3726. doi: 10.1111/gcb.12627
- 839 Blair, J. B., & Hofton, M. A. (1999, Aug). Modeling laser altimeter return wave-  
840 forms over complex vegetation using high-resolution elevation data. *Geophys.*  
841 *Res. Lett.*, *26*(16), 2509–2512. doi: 10.1029/1999GL010484
- 842 Blanc, L., Echard, M., Herault, B., Bonal, D., Marcon, E., Chave, J., & Baraloto, C.  
843 (2009, Sep). Dynamics of aboveground carbon stocks in a selectively logged  
844 tropical forest. *Ecol. Appl.*, *19*(6), 1397–1404. doi: 10.1890/08-1572.1
- 845 Bogan, S. A., Antonarakis, A. S., & Moorcroft, P. R. (2019, Jul). Imag-  
846 ing spectrometry-derived estimates of regional ecosystem composition for  
847 the Sierra Nevada, California. *Remote Sens. Environ.*, *228*, 14–30. doi:  
848 10.1016/j.rse.2019.03.031
- 849 Bonal, D., Bosc, A., Ponton, S., Goret, J.-Y., Burban, B., Gross, P., . . . Granier,  
850 A. (2008, Aug). Impact of severe dry season on net ecosystem exchange  
851 in the Neotropical rainforest of French Guiana. *Glob. Change Biol.*, *14*(8),  
852 1917–1933. doi: 10.1111/j.1365-2486.2008.01610.x
- 853 Both, S., Riutta, T., Paine, C. E. T., Elias, D. M. O., Cruz, R. S., Jain, A., . . .  
854 Burslem, D. F. R. P. (2019, Feb). Logging and soil nutrients independently ex-  
855 plain plant trait expression in tropical forests. *New Phytol.*, *221*(4), 1853–1865.  
856 doi: 10.1111/nph.15444
- 857 Brando, P. M., Balch, J. K., Nepstad, D. C., Morton, D. C., Putz, F. E., Coe,  
858 M. T., . . . Soares-Filho, B. S. (2014, Apr). Abrupt increases in Amazonian  
859 tree mortality due to drought–fire interactions. *Proc. Natl. Acad. Sci. U. S. A.*,  
860 *111*(17), 6347–6352. doi: 10.1073/pnas.1305499111
- 861 Brando, P. M., Nepstad, D. C., Balch, J. K., Bolker, B., Christman, M. C., Coe, M.,  
862 & Putz, F. E. (2012, Feb). Fire-induced tree mortality in a neotropical forest:  
863 the roles of bark traits, tree size, wood density and fire behavior. *Glob. Change*  
864 *Biol.*, *18*(2), 630–641. doi: 10.1111/j.1365-2486.2011.02533.x
- 865 Brando, P. M., Paolucci, L., Ummenhofer, C. C., Ordway, E. M., Hartmann, H.,

- 866 Cattau, M. E., ... Balch, J. (2019, May). Droughts, wildfires, and forest  
867 carbon cycling: A pantropical synthesis. *Annu. Rev. Earth Pl. Sc.*, *47*(1),  
868 555–581. doi: 10.1146/annurev-earth-082517-010235
- 869 Brando, P. M., Silvério, D., Maracahipes-Santos, L., Oliveira-Santos, C., Levick,  
870 S. R., Coe, M. T., ... Trumbore, S. E. (2019, Sep). Prolonged tropical forest  
871 degradation due to compounding disturbances: implications for CO<sub>2</sub> and H<sub>2</sub>O  
872 fluxes of an experimental forest. *Glob. Change Biol.*, *25*(9), 2855–2868. doi:  
873 10.1111/gcb.14659
- 874 Brando, P. M., Soares Filho, B., Rodrigues, L., Assunção, A., Morton, D., Tuch-  
875 schneider, D., ... Coe, M. T. (2020, Jan). The gathering firestorm in southern  
876 Amazonia. *Sci. Adv.*, *6*(2), eaay1632. doi: 10.1126/sciadv.aay1632
- 877 Brum, M., Vadeboncoeur, M. A., Ivanov, V., Asbjornsen, H., Saleska, S., Alves,  
878 L. F., ... Oliveira, R. S. (2019, Jan). Hydrological niche segregation defines  
879 forest structure and drought tolerance strategies in a seasonal Amazon forest.  
880 *J. Ecol.*, *107*(1), 318–333. doi: 10.1111/1365-2745.13022
- 881 Bustamante, M. M. C., Roitman, I., Aide, T. M., Alencar, A., Anderson, L., Aragão,  
882 L., ... Vieira, I. C. (2016, Jan). Towards an integrated monitoring frame-  
883 work to assess the effects of tropical forest degradation and recovery on  
884 carbon stocks and biodiversity. *Glob. Change Biol.*, *22*(1), 92–109. doi:  
885 10.1111/gcb.13087
- 886 Calders, K., Newnham, G., Burt, A., Murphy, S., Raunonen, P., Herold, M., ...  
887 Kaasalainen, M. (2015, Feb). Nondestructive estimates of above-ground  
888 biomass using terrestrial laser scanning. *Methods Ecol. Evol.*, *6*(2), 198–208.  
889 doi: 10.1111/2041-210X.12301
- 890 Chave, J., Condit, R., Aguilar, S., Hernandez, A., Lao, S., & Perez, R. (2004, Mar).  
891 Error propagation and scaling for tropical forest biomass estimates. *Philos.*  
892 *Trans. R. Soc. B-Biol. Sci.*, *359*(1443), 409–420. doi: 10.1098/rstb.2003.1425
- 893 Chave, J., Coomes, D., Jansen, S., Lewis, S. L., Swenson, N. G., & Zanne, A. E.  
894 (2009, Apr). Towards a worldwide wood economics spectrum. *Ecol. Lett.*,  
895 *12*(4), 351–366. doi: 10.1111/j.1461-0248.2009.01285.x
- 896 Chave, J., Réjou-Méchain, M., Búrquez, A., Chidumayo, E., Colgan, M. S., Delitti,  
897 W. B., ... Vieilledent, G. (2014, Oct). Improved allometric models to esti-  
898 mate the aboveground biomass of tropical trees. *Glob. Change Biol.*, *20*(10),

- 899 3177–3190. doi: 10.1111/gcb.12629
- 900 Cochrane, M. A., Alencar, A., Schulze, M. D., Souza, C. M., Nepstad, D. C., Lefeb-  
901 vre, P., & Davidson, E. A. (1999, Jun). Positive feedbacks in the fire dy-  
902 namic of closed canopy tropical forests. *Science*, *284*(5421), 1832–1835. doi:  
903 10.1126/science.284.5421.1832
- 904 Davidson, E. A., de Araújo, A. C., Artaxo, P., Balch, J. K., Brown, I. F., Bus-  
905 tamante, M. M. C., ... Wofsy, S. C. (2012, Jan). The Amazon basin in  
906 transition. *Nature*, *481*(7381), 321–328. doi: 10.1038/nature10717
- 907 de Almeida, C. T., Galvão, L. S., Aragão, L. E. d. O. C. e., Ometto, J. P. H. B., Ja-  
908 con, A. D., Pereira, F. R. d. S., ... Longo, M. (2019, Oct). Combining LiDAR  
909 and hyperspectral data for aboveground biomass modeling in the Brazilian  
910 Amazon using different regression algorithms. *Remote Sens. Environ.*, *232*,  
911 111323. doi: 10.1016/j.rse.2019.111323
- 912 De Faria, B. L., Brando, P. M., Macedo, M. N., Panday, P. K., Soares Filho, B. S.,  
913 & Coe, M. T. (2017, Sep). Current and future patterns of fire-induced  
914 forest degradation in Amazonia. *Environ. Res. Lett.*, *12*(9), 095005. doi:  
915 10.1088/1748-9326/aa69ce
- 916 de Resende, A. F., Nelson, B. W., Flores, B. M., & de Almeida, D. R. (2014, Nov).  
917 Fire damage in seasonally flooded and upland forests of the Central Amazon.  
918 *Biotropica*, *46*(6), 643–646. doi: 10.1111/btp.12153
- 919 d’Oliveira, M. V. N., Reutebuch, S. E., McGaughey, R. J., & Andersen, H.-E.  
920 (2012, Sep). Estimating forest biomass and identifying low-intensity log-  
921 ging areas using airborne scanning lidar in Antimary State Forest, Acre  
922 state, western Brazilian Amazon. *Remote Sens. Environ.*, *124*, 479–491.  
923 doi: 10.1016/j.rse.2012.05.014
- 924 dos-Santos, M., Keller, M., & Morton, D. (2019, Dec). *LiDAR surveys over se-*  
925 *lected forest research sites, Brazilian Amazon, 2008–2018*. Retrieved 31 Jan  
926 2020, from [https://daac.ornl.gov/cgi-bin/dsviewer.pl?ds\\_id=1644](https://daac.ornl.gov/cgi-bin/dsviewer.pl?ds_id=1644) doi:  
927 10.3334/ORNLDAAC/1644
- 928 Duffy, P. B., Brando, P., Asner, G. P., & Field, C. B. (2015, Oct). Projections of fu-  
929 ture meteorological drought and wet periods in the Amazon. *Proc. Natl. Acad.*  
930 *Sci. U. S. A.*, *112*(43), 13172–13177. doi: 10.1073/pnas.1421010112
- 931 Erb, K.-H., Fetzl, T., Plutzer, C., Kastner, T., Lauk, C., Mayer, A., ... Haberl, H.

- 932 (2016, Sep). Biomass turnover time in terrestrial ecosystems halved by land  
 933 use. *Nature Geosci.*, *9*(9), 674–678. doi: 10.1038/ngeo2782
- 934 Erb, K.-H., Kastner, T., Plutzer, C., Bais, A. L. S., Carvalhais, N., Fetzel, T., ...  
 935 Luysaert, S. (2018, Jan). Unexpectedly large impact of forest management  
 936 and grazing on global vegetation biomass. *Nature*, *553*(7686), 73–76. doi:  
 937 10.1038/nature25138
- 938 Falster, D. S., Duursma, R. A., Ishihara, M. I., Barneche, D. R., FitzJohn, R. G.,  
 939 Vårhammar, A., ... York, R. A. (2015, May). BAAD: a biomass and  
 940 allometry database for woody plants. *Ecology*, *96*(5), 1445–1445. doi:  
 941 10.1890/14-1889.1
- 942 Falster, D. S., FitzJohn, R. G., Brännström, Å., Dieckmann, U., & Westoby, M.  
 943 (2016, Feb). **plant**: A package for modelling forest trait ecology and evolution.  
 944 *Methods Ecol. Evol.*, *7*(2), 136–146. doi: 10.1111/2041-210X.12525
- 945 Fan, Y., Miguez-Macho, G., Jobbágy, E. G., Jackson, R. B., & Otero-Casal, C.  
 946 (2017, Oct). Hydrologic regulation of plant rooting depth. *Proc. Natl. Acad.*  
 947 *Sci. U. S. A.*, *114*(40), 10572–10577. doi: 10.1073/pnas.1712381114
- 948 Feldpausch, T. R., Banin, L., Phillips, O. L., Baker, T. R., Lewis, S. L., Quesada,  
 949 C. A., ... Lloyd, J. (2011, May). Height-diameter allometry of tropical forest  
 950 trees. *Biogeosciences*, *8*(5), 1081–1106. doi: 10.5194/bg-8-1081-2011
- 951 Feldpausch, T. R., Jirka, S., Passos, C. A. M., Jasper, F., & Riha, S. J. (2005,  
 952 11). When big trees fall: Damage and carbon export by reduced impact log-  
 953 ging in southern Amazonia. *Forest Ecol. Manag.*, *219*(2–3), 199–215. doi:  
 954 10.1016/j.foreco.2005.09.003
- 955 Feldpausch, T. R., Lloyd, J., Lewis, S. L., Brienien, R. J. W., Gloor, M., Mon-  
 956 teagudo Mendoza, A., ... Phillips, O. L. (2012, Aug). Tree height integrated  
 957 into pantropical forest biomass estimates. *Biogeosciences*, *9*(8), 3381–3403.  
 958 doi: 10.5194/bg-9-3381-2012
- 959 Ferraz, A., Saatchi, S., Mallet, C., & Meyer, V. (2016, Sep). Lidar detection of indi-  
 960 vidual tree size in tropical forests. *Remote Sens. Environ.*, *183*, 318–333. doi:  
 961 10.1016/j.rse.2016.05.028
- 962 Ferraz, A., Saatchi, S., Xu, L., Hagen, S., Chave, J., Yu, Y., ... Ganguly, S. (2018,  
 963 Sep). Carbon storage potential in degraded forests of Kalimantan, Indonesia.  
 964 *Environ. Res. Lett.*, *13*(9), 095001. doi: 10.1088/1748-9326/aad782

- 965 Fischer, F. J., Maréchaux, I., & Chave, J. (2019). Improving plant allometry by fus-  
 966 ing forest models and remote sensing. *New Phytol.* (advance online publica-  
 967 tion) doi: 10.1111/nph.15810
- 968 Fischer, R., Bohn, F., de Paula, M. D., Dislich, C., Groeneveld, J., Gutiérrez, A. G.,  
 969 ... Huth, A. (2016, Apr). Lessons learned from applying a forest gap model to  
 970 understand ecosystem and carbon dynamics of complex tropical forests. *Ecol.*  
 971 *Model.*, *326*, 124–133. doi: 10.1016/j.ecolmodel.2015.11.018
- 972 Fisher, R. A., Koven, C. D., Anderegg, W. R. L., Christoffersen, B. O., Dietze,  
 973 M. C., Farnier, C., ... Moorcroft, P. (2018, Jan). Vegetation demographics in  
 974 Earth system models: a review of progress and priorities. *Glob. Change Biol.*,  
 975 *24*(1), 35–54. doi: 10.1111/gcb.13910
- 976 Fonseca, M. G., Alves, L. M., Aguiar, A. P. D., Arai, E., Anderson, L. O., Rosan,  
 977 T. M., ... de Aragão, L. E. O. e. C. (2019). Effects of climate and land-use  
 978 change scenarios on fire probability during the 21<sup>st</sup> century in the Brazilian  
 979 Amazon. *Glob. Change Biol.* doi: 10.1111/gcb.14709
- 980 Friedlingstein, P., Jones, M. W., O’Sullivan, M., Andrew, R. M., Hauck, J., Peters,  
 981 G. P., ... Zaehle, S. (2019, Dec). Global carbon budget 2019. *Earth Syst. Sci.*  
 982 *Data*, *11*(4), 1783–1838. doi: 10.5194/essd-11-1783-2019
- 983 Fu, R., Yin, L., Li, W., Arias, P. A., Dickinson, R. E., Huang, L., ... Myneni, R. B.  
 984 (2013, Nov). Increased dry-season length over southern Amazonia in recent  
 985 decades and its implication for future climate projection. *Proc. Natl. Acad.*  
 986 *Sci. U. S. A.*, *110*(45), 18110–18115. doi: 10.1073/pnas.1302584110
- 987 Gelaro, R., McCarty, W., Suárez, M. J., Todling, R., Molod, A., Takacs, L., ...  
 988 Zhao, B. (2017, Jul). The Modern-Era Retrospective analysis for Research  
 989 and Applications, version 2 (MERRA-2). *J. Climate*, *30*(14), 5419–5454. doi:  
 990 10.1175/JCLI-D-16-0758.1
- 991 Ghazoul, J., & Chazdon, R. (2017, Oct). Degradation and recovery in changing for-  
 992 est landscapes: A multiscale conceptual framework. *Ann. Rev. Environ. Res.*,  
 993 *42*(1), 161–188. doi: 10.1146/annurev-environ-102016-060736
- 994 GMAO. (2015a). *MERRA-2 tavg1\_2d\_flux\_Nx: 2d, 1-hourly, time-averaged,*  
 995 *single-level, assimilation, surface flux diagnostics V5.12.4.* Retrieved 06  
 996 Sep 2018, from <https://doi.org/10.5067/7MCPBJ41Y0K6> doi: 10.5067/  
 997 7MCPBJ41Y0K6

- 998 GMAO. (2015b). *MERRA-2 tavg1\_2d\_lnd\_Nx: 2d, 1-hourly, time-averaged,*  
 999 *single-level, assimilation, land surface diagnostics V5.12.4.* Retrieved  
 1000 06 Sep 2018, from <https://doi.org/10.5067/RKPHT8KC1Y1T> doi:  
 1001 10.5067/RKPHT8KC1Y1T
- 1002 GMAO. (2015c). *MERRA-2 tavg1\_2d\_rad\_Nx: 2d, 1-hourly, time-averaged, single-*  
 1003 *level, assimilation, radiation diagnostics V5.12.4.* Retrieved 06 Sep 2018, from  
 1004 <https://doi.org/10.5067/Q9QMY5PBNV1T> doi: 10.5067/Q9QMY5PBNV1T
- 1005 GMAO. (2015d). *MERRA-2 tavg1\_2d\_slv\_Nx: 2d, 1-hourly, time-averaged,*  
 1006 *single-level, assimilation, single-level diagnostics V5.12.4.* Retrieved 06  
 1007 Sep 2018, from <https://doi.org/10.5067/VJAFPLI1CSIV> doi: 10.5067/  
 1008 VJAFPLI1CSIV
- 1009 Gourlet-Fleury, S., Ferry, B., Molino, J.-F., Petronelli, P., & Schmitt, L. (2004).  
 1010 Experimental plots: Key features. In S. Gourlet-Fleury, J.-M. Guehl, &  
 1011 O. Laroussinie (Eds.), *Ecology and management of a Neotropical rainforest:*  
 1012 *Lessons drawn from Paracou, a long-term experimental research site in French*  
 1013 *Guiana* (pp. 3–60). Paris: Elsevier.
- 1014 Grace, J., Mitchard, E., & Gloor, E. (2014, Oct). Perturbations in the carbon bud-  
 1015 get of the tropics. *Glob. Change Biol.*, *20*(10), 3238–3255. doi: 10.1111/gcb  
 1016 .12600
- 1017 Gu, L., Norby, R., Haworth, I., Jensen, A., Turner, B., Walker, A., . . . Winter, K.  
 1018 (2016). *Photosynthetic parameters and nutrient content of trees at the Panama*  
 1019 *crane sites. 1.0. NGEE Tropics data collection.* Retrieved 12 Sep 2019, from  
 1020 <https://ngt-data.1bl.gov> doi: 10.15486/NGT/1255260
- 1021 Haddad, N. M., Brudvig, L. A., Clobert, J., Davies, K. F., Gonzalez, A., Holt,  
 1022 R. D., . . . Townshend, J. R. (2015, Mar). Habitat fragmentation and its  
 1023 lasting impact on Earth’s ecosystems. *Science Advances*, *1*(2), e1500052. doi:  
 1024 10.1126/sciadv.1500052
- 1025 Hancock, S., Armston, J., Hofton, M., Sun, X., Tang, H., Duncanson, L. I., . . .  
 1026 Dubayah, R. (2019, Feb). The GEDI simulator: A large-footprint waveform  
 1027 lidar simulator for calibration and validation of spaceborne missions. *Earth*  
 1028 *Space Sci.*, *6*(2), 290–310. doi: 10.1029/2018EA000506
- 1029 Hansen, M. C., Potapov, P. V., Moore, R., Hancher, M., Turubanova, S. A.,  
 1030 Tyukavina, A., . . . Townshend, J. R. G. (2013, Nov). High-resolution global

- 1031 maps of 21st-century forest cover change. *Science*, *342*(6160), 850–853. doi:  
 1032 10.1126/science.1244693
- 1033 Harris, N. L., Brown, S., Hagen, S. C., Saatchi, S. S., Petrova, S., Salas, W., ...  
 1034 Lotsch, A. (2012, Jun). Baseline map of carbon emissions from deforestation in  
 1035 tropical regions. *Science*, *336*(6088), 1573–1576. doi: 10.1126/science.1217962
- 1036 Hayek, M. N., Longo, M., Wu, J., Smith, M. N., Restrepo-Coupe, N., Tapajós,  
 1037 R., ... Wofsy, S. C. (2018, Aug). Carbon exchange in an Amazon  
 1038 forest: from hours to years. *Biogeosciences*, *15*(15), 4833–4848. doi:  
 1039 10.5194/bg-15-4833-2018
- 1040 Hérault, B., & Piponiot, C. (2018, Feb). Key drivers of ecosystem recovery after dis-  
 1041 turbance in a neotropical forest. *Forest Ecosyst.*, *5*(1), 2. doi: 10.1186/s40663  
 1042 -017-0126-7
- 1043 Hess, L. L., Melack, J. M., Affonso, A. G., Barbosa, C., Gastil-Buhl, M., & Novo,  
 1044 E. M. L. M. (2015, Aug). Wetlands of the lowland Amazon Basin: Ex-  
 1045 tent, vegetative cover, and dual-season inundated area as mapped with  
 1046 JERS-1 synthetic aperture radar. *Wetlands*, *35*(4), 745–756. doi: 10.1007/  
 1047 s13157-015-0666-y
- 1048 Hirano, T., Kusin, K., Limin, S., & Osaki, M. (2015, May). Evapotranspiration of  
 1049 tropical peat swamp forests. *Glob. Change Biol.*, *21*(5), 1914–1927. doi: 10  
 1050 .1111/gcb.12653
- 1051 Hosonuma, N., Herold, M., De Sy, V., De Fries, R. S., Brockhaus, M., Verchot, L.,  
 1052 ... Romijn, E. (2012, Apr). An assessment of deforestation and forest degra-  
 1053 dation drivers in developing countries. *Environ. Res. Lett.*, *7*(4), 044009. doi:  
 1054 10.1088/1748-9326/7/4/044009
- 1055 Huang, M., & Asner, G. P. (2010, Sep). Long-term carbon loss and recovery fol-  
 1056 lowing selective logging in Amazon forests. *Global Biogeochem. Cycles*, *24*(3),  
 1057 GB3028. doi: 10.1029/2009GB003727
- 1058 Huang, M., Asner, G. P., Keller, M., & Berry, J. A. (2008, Mar). An ecosystem  
 1059 model for tropical forest disturbance and selective logging. *J. Geophys. Res.-*  
 1060 *Biogeosci.*, *113*(G1), G01002. doi: 10.1029/2007JG000438
- 1061 Hunter, M. O., Keller, M., Vitoria, D., & Morton, D. C. (2013, Dec). Tree height  
 1062 and tropical forest biomass estimation. *Biogeosciences*, *10*(6), 10491–10529.  
 1063 doi: 10.5194/bg-10-8385-2013

- 1064 Hurtt, G. C., Dubayah, R., Drake, J., Moorcroft, P. R., Pacala, S. W., Blair, J. B.,  
 1065 & Fearon, M. G. (2004, Jun). Beyond potential vegetation: combining lidar  
 1066 data and a height-structured model for carbon studies. *Ecol. Appl.*, *14*(3),  
 1067 873–883. doi: 10.1890/02-5317
- 1068 INMET. (2019, May). *Normais climatológicas do Brasil: 1981-2010*. Retrieved 15  
 1069 May 2019, from [http://www.inmet.gov.br/portal/index.php?r=clima/  
 1070 normaisClimatologicas](http://www.inmet.gov.br/portal/index.php?r=clima/normaisClimatologicas) (In Portuguese)
- 1071 IPCC. (2014). *Climate change 2014: impacts, adaptation, and vulnerability. part b:  
 1072 regional aspects. contribution of working group ii to the fifth assessment report  
 1073 of the Intergovernmental Panel on Climate Change* (V. R. Barros et al., Eds.).  
 1074 Cambridge, UK and New York, NY, USA: Cambridge Univ. Press.
- 1075 Jucker, T., Caspersen, J., Chave, J., Antin, C., Barbier, N., Bongers, F., ...  
 1076 Coomes, D. A. (2017, Jan). Allometric equations for integrating remote  
 1077 sensing imagery into forest monitoring programmes. *Glob. Change Biol.*, *23*(1),  
 1078 177–190. doi: 10.1111/gcb.13388
- 1079 Jucker, T., Hardwick, S. R., Both, S., Elias, D. M., Ewers, R. M., Milodowski, D. T.,  
 1080 ... Coomes, D. A. (2018, Nov). Canopy structure and topography jointly con-  
 1081 strain the microclimate of human-modified tropical landscapes. *Glob. Change  
 1082 Biol.*, *24*(11), 5243–5258. doi: 10.1111/gcb.14415
- 1083 Kapos, V. (1989, May). Effects of isolation on the water status of forest  
 1084 patches in the brazilian amazon. *J. Trop. Ecol.*, *5*(2), 173–185. doi:  
 1085 10.1017/S0266467400003448
- 1086 Kattge, J., Bönisch, G., Díaz, S., Lavorel, S., Prentice, I. C., Leadley, P., ... Wirth,  
 1087 C. (2020, Jan). TRY plant trait database — enhanced coverage and open  
 1088 access. *Glob. Change Biol.*, *26*(1), 119–188. doi: 10.1111/gcb.14904
- 1089 Kattge, J., Díaz, S., Lavorel, S., Prentice, I. C., Leadley, P., Bönisch, G., ... Wirth,  
 1090 C. (2011, Sep). TRY – a global database of plant traits. *Glob. Change Biol.*,  
 1091 *17*(9), 2905–2935. doi: 10.1111/j.1365-2486.2011.02451.x
- 1092 Kattge, J., Knorr, W., Raddatz, T., & Wirth, C. (2009, Apr). Quantifying pho-  
 1093 tosynthetic capacity and its relationship to leaf nitrogen content for global-  
 1094 scale terrestrial biosphere models. *Glob. Change Biol.*, *15*(4), 976–991. doi:  
 1095 10.1111/j.1365-2486.2008.01744.x
- 1096 Keenan, T. F., & Niinemets, Ü. (2016, Dec). Global leaf trait estimates biased due

- 1097 to plasticity in the shade. *Nat. Plants*, 3, 16201. doi: 10.1038/nplants.2016  
1098 .201
- 1099 Knox, R. G., Longo, M., Swann, A. L. S., Zhang, K., Levine, N. M., Moorcroft,  
1100 P. R., & Bras, R. L. (2015, Jan). Hydrometeorological effects of historical  
1101 land-conversion in an ecosystem-atmosphere model of Northern South Amer-  
1102 ica. *Hydrol. Earth Syst. Sci.*, 19(1), 241–273. doi: 10.5194/hess-19-241-2015
- 1103 Laybros, A., Schläpfer, D., Féret, J.-B., Descroix, L., Bedeau, C., Lefevre, M.-J., &  
1104 Vincent, G. (2019, Apr). Across date species detection using airborne imaging  
1105 spectroscopy. *Remote Sens.*, 11(7), 789. doi: 10.3390/rs11070789
- 1106 Lees, J. M. (2017). RSEIS: Seismic time series analysis tools [Computer software  
1107 manual]. Retrieved from <https://CRAN.R-project.org/package=RSEIS> (R  
1108 package version 3.7-4)
- 1109 Leitold, V., Keller, M., Morton, D., Cook, B., & Shimabukuro, Y. (2015, Feb).  
1110 Airborne lidar-based estimates of tropical forest structure in complex terrain:  
1111 opportunities and trade-offs for REDD+. *Carbon Balance Manage.*, 10(1), 3.  
1112 doi: 10.1186/s13021-015-0013-x
- 1113 Le Page, Y., Morton, D., Bond-Lamberty, B., Pereira, J. M. C., & Hurtt, G. (2015,  
1114 Feb). HESFIRE: a global fire model to explore the role of anthropogenic and  
1115 weather drivers. *Biogeosciences*, 12(3), 887–903. doi: 10.5194/bg-12-887-2015
- 1116 Le Page, Y., Morton, D., Hartin, C., Bond-Lamberty, B., Pereira, J. M. C., Hurtt,  
1117 G., & Asrar, G. (2017, Dec). Synergy between land use and climate change  
1118 increases future fire risk in Amazon forests. *Earth Syst. Dynam.*, 8(4), 1237–  
1119 1246. doi: 10.5194/esd-8-1237-2017
- 1120 Levine, N. M., Zhang, K., Longo, M., Baccini, A., Phillips, O. L., Lewis, S. L., ...  
1121 Moorcroft, P. R. (2016, Jan). Ecosystem heterogeneity determines the re-  
1122 siliance of the Amazon to climate change. *Proc. Natl. Acad. Sci. U. S. A.*,  
1123 113(3), 793–797. doi: 10.1073/pnas.1511344112
- 1124 Lewis, S. L., Edwards, D. P., & Galbraith, D. (2015, Aug). Increasing human dom-  
1125 inance of tropical forests. *Science*, 349(6250), 827–832. doi: 10.1126/science  
1126 .aaa9932
- 1127 Lloyd, J., Patiño, S., Paiva, R. Q., Nardoto, G. B., Quesada, C. A., Santos, A. J. B.,  
1128 ... Mercado, L. M. (2010, Jun). Optimisation of photosynthetic carbon gain  
1129 and within-canopy gradients of associated foliar traits for Amazon forest trees.

- 1130 *Biogeosciences*, 7(6), 1833–1859. doi: 10.5194/bg-7-1833-2010
- 1131 Lombardozzi, D. L., Smith, N. G., Cheng, S. J., Dukes, J. S., Sharkey, T. D.,  
 1132 Rogers, A., ... Bonan, G. B. (2018, Jul). Triose phosphate limitation in  
 1133 photosynthesis models reduces leaf photosynthesis and global terrestrial carbon  
 1134 storage. *Environ. Res. Lett.*, 13(7), 074025. doi: 10.1088/1748-9326/aacf68
- 1135 Longo, M., Keller, M., dos-Santos, M. N., Morton, D., Moorcroft, P. R., Vincent, G.,  
 1136 ... Saatchi, S. (2020, Feb). Supporting dataset for “Impacts of degradation  
 1137 on water, energy, and carbon cycling of the Amazon tropical forests”. *Zenodo*.  
 1138 doi: 10.5281/zenodo.3634131
- 1139 Longo, M., Keller, M., dos Santos, M. N., Leitold, V., Pinagé, E. R., Baccini, A., ...  
 1140 Morton, D. C. (2016, Nov). Aboveground biomass variability across intact and  
 1141 degraded forests in the Brazilian Amazon. *Global Biogeochem. Cycles*, 30(11),  
 1142 1639–1660. doi: 10.1002/2016GB005465
- 1143 Longo, M., Knox, R., Medvigy, D. M., Levine, N. M., Dietze, M., Swann, A. L. S.,  
 1144 ... Moorcroft, P. (2019, Aug). Ecosystem Demography model, version 2.2  
 1145 (ed-2.2). *Zenodo*. doi: 10.5281/zenodo.3365659
- 1146 Longo, M., Knox, R. G., Levine, N. M., Swann, A. L. S., Medvigy, D. M., Dietze,  
 1147 M. C., ... Moorcroft, P. R. (2019, Oct). The biophysics, ecology, and bio-  
 1148 geochemistry of functionally diverse, vertically and horizontally heterogeneous  
 1149 ecosystems: the Ecosystem Demography model, version 2.2 – part 2: Model  
 1150 evaluation for tropical South America. *Geosci. Model Dev.*, 12(10), 4347–4374.  
 1151 doi: 10.5194/gmd-12-4347-2019
- 1152 Longo, M., Knox, R. G., Medvigy, D. M., Levine, N. M., Dietze, M. C., Kim, Y., ...  
 1153 Moorcroft, P. R. (2019, Oct). The biophysics, ecology, and biogeochemistry  
 1154 of functionally diverse, vertically and horizontally heterogeneous ecosystems:  
 1155 the Ecosystem Demography model, version 2.2 – part 1: Model description.  
 1156 *Geosci. Model Dev.*, 12(10), 4309–4346. doi: 10.5194/gmd-12-4309-2019
- 1157 MacArthur, R. H., & Horn, H. S. (1969, Sep). Foliage profile by vertical measure-  
 1158 ments. *Ecology*, 50(5), 802–804. doi: 10.2307/1933693
- 1159 Maréchaux, I., & Chave, J. (2017, Nov). An individual-based forest model to jointly  
 1160 simulate carbon and tree diversity in Amazonia: description and applications.  
 1161 *Ecol. Monogr.*, 87(4), 632–664. doi: 10.1002/ecm.1271
- 1162 Martins, F. S. R. V., Xaud, H. A. M., dos Santos, J. R., & Galvão, L. S. (2012,

- 1163 Nov). Effects of fire on above-ground forest biomass in the northern Brazilian  
 1164 Amazon. *J. Trop. Ecol.*, *28*(6), 591–601. doi: 10.1017/S0266467412000636
- 1165 Marvin, D. C., Asner, G. P., Knapp, D. E., Anderson, C. B., Martin, R. E., Sinca,  
 1166 F., & Tupayachi, R. (2014, Dec). Amazonian landscapes and the bias in  
 1167 field studies of forest structure and biomass. *Proc. Natl. Acad. Sci. U. S. A.*,  
 1168 *111*(48), E5224–E5232. doi: 10.1073/pnas.1412999111
- 1169 Mascaro, J., Litton, C. M., Hughes, R. F., Uowolo, A., & Schnitzer, S. A. (2011,  
 1170 Nov). Minimizing bias in biomass allometry: Model selection and log-  
 1171 transformation of data. *Biotropica*, *43*(6), 649–653. doi: 10.1111/  
 1172 j.1744-7429.2011.00798.x
- 1173 Matsunaga, T., Iwasaki, A., Tsuchida, S., Iwao, K., Tanii, J., Kashimura, O., . . .  
 1174 Tachikawa, T. (2017, Jul). Current status of hyperspectral imager suite  
 1175 (HISUI) onboard international space station (ISS). In *2017 IEEE interna-*  
 1176 *tional geoscience and remote sensing symposium (IGARSS)* (pp. 443–446). doi:  
 1177 10.1109/IGARSS.2017.8126989
- 1178 Mauya, E., Hansen, E., Gobakken, T., Bollandas, O., Malimbwi, R., & Næs-  
 1179 set, E. (2015, May). Effects of field plot size on prediction accuracy of  
 1180 aboveground biomass in airborne laser scanning-assisted inventories in trop-  
 1181 ical rain forests of Tanzania. *Carbon Balance Manage.*, *10*(1), 10. doi:  
 1182 10.1186/s13021-015-0021-x
- 1183 Medvigy, D. M., Wofsy, S. C., Munger, J. W., Hollinger, D. Y., & Moorcroft, P. R.  
 1184 (2009, Jan). Mechanistic scaling of ecosystem function and dynamics in  
 1185 space and time: Ecosystem demography model version 2. *J. Geophys. Res.-*  
 1186 *Biogeosci.*, *114*(G1), G01002. doi: 10.1029/2008JG000812
- 1187 Meister, K., Ashton, M. S., Craven, D., & Griscom, H. (2012). Carbon dynamics  
 1188 of tropical forests. In M. S. Ashton, M. L. Tyrrell, D. Spalding, & B. Gentry  
 1189 (Eds.), (pp. 51–75). Dordrecht, Netherlands: Springer Netherlands. doi: 10  
 1190 .1007/978-94-007-2232-3\_4
- 1191 Mesquita, R. d. C. G., Massoca, P. E. d. S., Jakovac, C. C., Bentos, T. V., &  
 1192 Williamson, G. B. (2015, Aug). Amazon rain forest succession: Stochasticity  
 1193 or land-use legacy? *BioScience*, *65*(9), 849–861. doi: 10.1093/biosci/biv108
- 1194 Meyer, V., Saatchi, S., Ferraz, A., Xu, L., Duque, A., García, M., & Chave, J. (2019,  
 1195 Mar). Forest degradation and biomass loss along the Chocó region of Colom-

- 1196           bia. *Carbon Balance Manage.*, *14*(1), 2. doi: 10.1186/s13021-019-0117-9
- 1197 Meyer, V., Saatchi, S. S., Chave, J., Dalling, J. W., Bohlman, S., Fricker, G. A., ...
- 1198           Hubbell, S.   (2013, Aug).   Detecting tropical forest biomass dynamics from
- 1199           repeated airborne lidar measurements. *Biogeosciences*, *10*(8), 5421–5438. doi:
- 1200           10.5194/bg-10-5421-2013
- 1201 Miller, A. J. (1984, Nov). Selection of subsets of regression variables. *J. R. Stat. Soc.*
- 1202           *A-Gen.*, *147*(3), 389–425. doi: 10.2307/2981576
- 1203 Miller, S. D., Goulden, M. L., Hutryra, L. R., Keller, M., Saleska, S. R., Wofsy, S. C.,
- 1204           ... de Camargo, P. B.   (2011, Nov).   Reduced impact logging minimally alters
- 1205           tropical rainforest carbon and energy exchange. *Proc. Natl. Acad. Sci. U. S.*
- 1206           *A.*, *108*(48), 19431–19435. doi: 10.1073/pnas.1105068108
- 1207 Moorcroft, P. R., Hurtt, G. C., & Pacala, S. W.   (2001, Nov).   A method for scaling
- 1208           vegetation dynamics: The Ecosystem Demography model (ED). *Ecol. Monogr.*,
- 1209           *71*(4), 557–586.   doi: 10.1890/0012-9615(2001)071{[\$]}0557:AMFSVD{[\$]}2.0
- 1210           .CO;2
- 1211 Morton, D. C.   (2016, Apr).   Forest carbon fluxes: A satellite perspective. *Nature*
- 1212           *Clim. Change*, *6*(4), 346–348. doi: 10.1038/nclimate2978
- 1213 Morton, D. C., Le Page, Y., DeFries, R. S., Collatz, G. J., & Hurtt, G. C.   (2013,
- 1214           Jun).   Understorey fire frequency and the fate of burned forests in southern
- 1215           Amazonia. *Philos. Trans. R. Soc. B-Biol. Sci.*, *368*(1619), 20120163.   doi:
- 1216           10.1098/rstb.2012.0163
- 1217 Ni-Meister, W., Jupp, D., & Dubayah, R.   (2001, Sep).   Modeling lidar waveforms
- 1218           in heterogeneous and discrete canopies. *IEEE T. Geosci. Remote Sens.*, *39*(9),
- 1219           1943–1958. doi: 10.1109/36.951085
- 1220 Norby, R. J., Gu, L., Haworth, I. C., Jensen, A. M., Turner, B. L., Walker, A. P.,
- 1221           ... Winter, K.   (2017, Sep).   Informing models through empirical relationships
- 1222           between foliar phosphorus, nitrogen and photosynthesis across diverse woody
- 1223           species in tropical forests of Panama. *New Phytol.*, *215*(4), 1425–1437.   doi:
- 1224           10.1111/nph.14319
- 1225 Oleson, K. W., Lawrence, D. M., Bonan, G. B., Drewniak, B., Huang, M., Koven,
- 1226           C. D., ... Yang, Z.-L.   (2013).   *Technical description of version 4.5 of the*
- 1227           *community land model (CLM)* (Technical Report Nos. NCAR/TN-503+STR).
- 1228           Boulder, CO: NCAR. (420pp.) doi: 10.5065/D6RR1W7M

- 1229 Olson, D. M., Dinerstein, E., Wikramanayake, E. D., Burgess, N. D., Powell,  
 1230 G. V. N., Underwood, E. C., . . . Kassem, K. R. (2001, Nov). Terrestrial  
 1231 ecoregions of the world: A new map of life on Earth. *BioScience*, *51*(11),  
 1232 933–938. doi: 10.1641/0006-3568(2001)051[0933:TEOTWA]2.0.CO;2
- 1233 Paracou Portal. (2016, Dec). *Paracou research station, a large-scale forest distur-*  
 1234 *bance experiment in Amazonia*. Retrieved 31 Jan 2020, from [https://paracou](https://paracou.cirad.fr)  
 1235 [.cirad.fr](https://paracou.cirad.fr)
- 1236 Pearson, T. R. H., Brown, S., Murray, L., & Sidman, G. (2017, Feb). Greenhouse  
 1237 gas emissions from tropical forest degradation: an underestimated source. *Car-*  
 1238 *bon Balance Manage.*, *12*(1), 3. doi: 10.1186/s13021-017-0072-2
- 1239 Pellegrini, A. F. A., Franco, A. C., & Hoffmann, W. A. (2016, Mar). Shifts in  
 1240 functional traits elevate risk of fire-driven tree dieback in tropical savanna and  
 1241 forest biomes. *Glob. Change Biol.*, *22*(3), 1235–1243. doi: 10.1111/gcb.13110
- 1242 Pinagé, E. R., Keller, M., Duffy, P., Longo, M., dos Santos, M. N., & Morton, D. C.  
 1243 (2019, Mar). Long-term impacts of selective logging on Amazon forest dy-  
 1244 namics from multi-temporal airborne LiDAR. *Remote Sens.*, *11*(6), 709. doi:  
 1245 10.3390/rs11060709
- 1246 Pinto, A., Amaral, P., Souza Jr., C. M., Veríssimo, A., Salomão, R., Gomes,  
 1247 G., & Balieiro, C. (2009). *Diagnóstico socioeconômico e florestal*  
 1248 *do município de Paragominas* (Technical Report). Belém,  
 1249 PA, Brazil: Instituto do Homem e Meio Ambiente da Amazônia  
 1250 (Imazon). (Available at [http://amazon.org.br/publicacoes/](http://amazon.org.br/publicacoes/diagnostico-socioeconomico-e-florestal-do-municipio-de-paragominas/)  
 1251 [diagnostico-socioeconomico-e-florestal-do-municipio-de-paragominas/](http://amazon.org.br/publicacoes/diagnostico-socioeconomico-e-florestal-do-municipio-de-paragominas/)  
 1252 )
- 1253 Popescu, S. C., Zhao, K., Neuenschwander, A., & Lin, C. (2011, Nov). Satellite lidar  
 1254 vs. small footprint airborne lidar: Comparing the accuracy of aboveground  
 1255 biomass estimates and forest structure metrics at footprint level. *Remote Sens.*  
 1256 *Environ.*, *115*(11), 2786–2797. doi: 10.1016/j.rse.2011.01.026
- 1257 Potapov, P., Hansen, M. C., Laestadius, L., Turubanova, S., Yaroshenko, A., Thies,  
 1258 C., . . . Esipova, E. (2017, Jan). The last frontiers of wilderness: Tracking loss  
 1259 of intact forest landscapes from 2000 to 2013. *Sci. Adv.*, *3*(1), e1600821. doi:  
 1260 10.1126/sciadv.1600821
- 1261 Powell, T. L., Galbraith, D. R., Christoffersen, B. O., Harper, A., Imbuzeiro,

- 1262 H. M. A., Rowland, L., . . . Moorcroft, P. R. (2013, Oct). Confronting model  
1263 predictions of carbon fluxes with measurements of Amazon forests subjected to  
1264 experimental drought. *New Phytol.*, *200*(2), 350–365. doi: 10.1111/nph.12390
- 1265 Powers, J. S., & Tiffin, P. (2010, Aug). Plant functional type classifications in trop-  
1266 ical dry forests in Costa Rica: leaf habit versus taxonomic approaches. *Funct.*  
1267 *Ecol.*, *24*(4), 927–936. doi: 10.1111/j.1365-2435.2010.01701.x
- 1268 Priestley, C. H. B., & Taylor, R. J. (1972, Feb). On the assessment of surface heat  
1269 flux and evaporation using large-scale parameters. *Mon. Wea. Rev.*, *100*(2),  
1270 81–92. doi: 10.1175/1520-0493(1972)100<0081:OTAOSH>2.3.CO;2
- 1271 PRODES-INPE. (2018, Nov). *Taxas anuais de desmatamento*. Retrieved 9 Jan 2019,  
1272 from <http://www.obt.inpe.br/prodes/index.php> (In Portuguese)
- 1273 Purves, D., & Pacala, S. (2008, Jun). Predictive models of forest dynamics. *Science*,  
1274 *320*(5882), 1452–1453. doi: 10.1126/science.1155359
- 1275 Pütz, S., Groeneveld, J., Henle, K., Knogge, C., Martensen, A. C., Metz, M., . . .  
1276 Huth, A. (2014, Oct). Long-term carbon loss in fragmented Neotropical  
1277 forests. *Nat. Commun.*, *5*. doi: 10.1038/ncomms6037
- 1278 Quesada, C. A., Miranda, A. C., Hodnett, M. G., Santos, A. J. B., Miranda, H. S.,  
1279 & Breyer, L. M. (2004, Aug). Seasonal and depth variation of soil moisture in  
1280 a burned open savanna (campo sujo) in central Brazil. *Ecol. Appl.*, *14*(sp4),  
1281 33–41. doi: 10.1890/01-6017
- 1282 R Core Team. (2019). R: A language and environment for statistical computing  
1283 [Computer software manual]. Vienna, Austria. Retrieved from [http://www.R](http://www.R-project.org/)  
1284 [-project.org/](http://www.R-project.org/)
- 1285 Rappaport, D., Morton, D., Longo, M., Keller, M., Dubayah, R., & dos-Santos,  
1286 M. N. (2018, Jun). Quantifying long-term changes in carbon stocks and forest  
1287 structure from Amazon forest degradation. *Environ. Res. Lett.*, *13*(6), 065013.  
1288 doi: 10.1088/1748-9326/aac331
- 1289 Ray, D., Nepstad, D., & Moutinho, P. (2005, Oct). Micrometeorological and canopy  
1290 controls of fire susceptibility in a forested Amazon landscape. *Ecol. Appl.*,  
1291 *15*(5), 1664–1678. doi: 10.1890/05-0404
- 1292 Rödiger, E., Cuntz, M., Rammig, A., Fischer, R., Taubert, F., & Huth, A. (2018,  
1293 Apr). The importance of forest structure for carbon fluxes of the Amazon rain-  
1294 forest. *Environ. Res. Lett.*, *13*(5), 054013. doi: 10.1088/1748-9326/aabc61

- 1295 Russo, S., & Kitajima, K. (2016, Mar). The ecophysiology of leaf lifespan in  
1296 tropical forests: Adaptive and plastic responses to environmental hetero-  
1297 geneity. In G. Goldstein & L. S. Santiago (Eds.), *Tropical tree physiol-  
1298 ogy: Adaptations and responses in a changing environment* (Vol. 6, pp.  
1299 357–383). Cham, Switzerland: Springer International Publishing. doi:  
1300 10.1007/978-3-319-27422-5\_17
- 1301 Sabine, C. L., Heimann, M., Artaxo, P., Bakker, D. C. E., Chen, C.-T. A., Field,  
1302 C. B., . . . Valentini, R. (2004). Current status and past trends of the global  
1303 carbon cycle. In C. B. Field & M. R. Raupach (Eds.), *The global carbon cy-  
1304 cle: integrating humans, climate, and the natural world* (Vol. 62, pp. 17–44).  
1305 Washington, DC, USA: Island Press.
- 1306 Santiago, L. S., & Wright, S. J. (2007, Feb). Leaf functional traits of tropical forest  
1307 plants in relation to growth form. *Funct. Ecol.*, *21*(1), 19–27. doi: 10.1111/j  
1308 .1365-2435.2006.01218.x
- 1309 Schimel, D., Schneider, F., & JPL Carbon and Ecosystem Participants. (2019). Flux  
1310 towers in the sky: global ecology from space. *New Phytol.* (advance online  
1311 publication) doi: 10.1111/nph.15934
- 1312 Schneider, F. D., Kükenbrink, D., Schaepman, M. E., Schimel, D. S., & Morsdorf,  
1313 F. (2019, Apr). Quantifying 3D structure and occlusion in dense tropical  
1314 and temperate forests using close-range LiDAR. *Agric. For. Meteorol.*, *268*,  
1315 249–257. doi: 10.1016/j.agrformet.2019.01.033
- 1316 Schneider, F. D., Morsdorf, F., Schmid, B., Petchey, O. L., Hueni, A., Schimel,  
1317 D. S., & Schaepman, M. E. (2017, Nov). Mapping functional diversity from  
1318 remotely sensed morphological and physiological forest traits. *Nat. Commun.*,  
1319 *8*(1), 1441. doi: 10.1038/s41467-017-01530-3
- 1320 Schwarz, G. (1978, Mar). Estimating the dimension of a model. *Ann. Stat.*, *6*(2),  
1321 461–464. doi: 10.1214/aos/1176344136
- 1322 Sena, E. T., Silva Dias, M. A. F., Carvalho, L. M. V., & Silva Dias, P. L. (2018,  
1323 Dec). Reduced wet-season length detected by satellite retrievals of cloudiness  
1324 over Brazilian Amazonia: A new methodology. *J. Climate*, *31*(24), 9941–9964.  
1325 doi: 10.1175/JCLI-D-17-0702.1
- 1326 Senior, R. A., Hill, J. K., Benedick, S., & Edwards, D. P. (2018, Mar). Tropical  
1327 forests are thermally buffered despite intensive selective logging. *Glob. Change*

- 1328 *Biol.*, 24(3), 1267–1278. doi: 10.1111/gcb.13914
- 1329 Shao, G., Stark, S. C., de Almeida, D. R., & Smith, M. N. (2019, Feb). Towards  
1330 high throughput assessment of canopy dynamics: The estimation of leaf area  
1331 structure in Amazonian forests with multitemporal multi-sensor airborne lidar.  
1332 *Remote Sens. Environ.*, 221(221), 1–13. doi: 10.1016/j.rse.2018.10.035
- 1333 Silva, C. V. J., Aragão, L. E. O. C., Barlow, J., Espírito-Santo, F., Young, P. J.,  
1334 Anderson, L. O., . . . Xaud, H. A. M. (2018, Nov). Drought-induced Ama-  
1335 zonian wildfires instigate a decadal-scale disruption of forest carbon dy-  
1336 namics. *Philos. Trans. R. Soc. B-Biol. Sci.*, 373(1760), 20180043. doi:  
1337 10.1098/rstb.2018.0043
- 1338 Silvério, D. V., Brando, P. M., Bustamante, M. M., Putz, F. E., Marra, D. M.,  
1339 Levick, S. R., & Trumbore, S. E. (2019, Mar). Fire, fragmentation, and wind-  
1340 storms: a recipe for tropical forest degradation. *J. Ecol.*, 107(2), 656–667. doi:  
1341 10.1111/1365-2745.13076
- 1342 Souza Jr., C. M., Siqueira, J., Sales, M. H., Fonseca, A., Ribeiro, J., Numat, . . .  
1343 Barlow, J. B. (2013, Oct). Ten-year Landsat classification of deforestation and  
1344 forest degradation in the Brazilian Amazon. *Remote Sens.*, 5(11), 5493–5513.  
1345 doi: 10.3390/rs5115493
- 1346 Spracklen, D., Baker, J., Garcia-Carreras, L., & Marsham, J. (2018, Oct). The ef-  
1347 fects of tropical vegetation on rainfall. *Ann. Rev. Environ. Res.*, 43(1), 193–  
1348 218. doi: 10.1146/annurev-environ-102017-030136
- 1349 Stahl, C., Hérault, B., Rossi, V., Burban, B., Bréchet, C., & Bonal, D. (2013,  
1350 Dec). Depth of soil water uptake by tropical rainforest trees during dry  
1351 periods: does tree dimension matter? *Oecologia*, 173(4), 1191–1201. doi:  
1352 10.1007/s00442-013-2724-6
- 1353 Stark, S. C., Leitold, V., Wu, J. L., Hunter, M. O., de Castilho, C. V., Costa,  
1354 F. R. C., . . . Saleska, S. R. (2012, Dec). Amazon forest carbon dynamics  
1355 predicted by profiles of canopy leaf area and light environment. *Ecol. Lett.*,  
1356 15(12), 1406–1414. doi: 10.1111/j.1461-0248.2012.01864.x
- 1357 Stavros, E. N., Schimel, D., Pavlick, R., Serbin, S., Swann, A., Duncanson, L., . . .  
1358 Wennberg, P. (2017, Jun). ISS observations offer insights into plant function.  
1359 *Nature Ecol. Evol.*, 1, 0194. doi: 10.1038/s41559-017-0194
- 1360 Stovall, A. E., Anderson Teixeira, K. J., & Shugart, H. H. (2018, Nov). Assessing

- 1361 terrestrial laser scanning for developing non-destructive biomass allometry.  
 1362 *Forest Ecol. Manag.*, 427, 217–229. doi: 10.1016/j.foreco.2018.06.004
- 1363 Sustainable Landscapes Brazil. (2019, Nov). Retrieved 9 Jan 2019, from [https://](https://www.paisagenslidar.cnptia.embrapa.br/webgis/)  
 1364 [www.paisagenslidar.cnptia.embrapa.br/webgis/](https://www.paisagenslidar.cnptia.embrapa.br/webgis/)
- 1365 Swann, A. L. S., & Koven, C. D. (2017, Aug). A direct estimate of the seasonal  
 1366 cycle of evapotranspiration over the Amazon Basin. *J. Hydrometeor.*, 18(8),  
 1367 2173–2185. doi: 10.1175/JHM-D-17-0004.1
- 1368 Swann, A. L. S., Longo, M., Knox, R. G., Lee, E., & Moorcroft, P. R. (2015,  
 1369 Dec). Future deforestation in the Amazon and consequences for South  
 1370 American climate. *Agric. For. Meteorol.*, 214–215, 12–24. doi: 10.1016/  
 1371 j.agrformet.2015.07.006
- 1372 Tang, H., & Dubayah, R. (2017, Mar). Light-driven growth in Amazon evergreen  
 1373 forests explained by seasonal variations of vertical canopy structure. *Proc.*  
 1374 *Natl. Acad. Sci. U. S. A.*, 114(10), 2640–2644. doi: 10.1073/pnas.1616943114
- 1375 Thonicke, K., Spessa, A., Prentice, I. C., Harrison, S. P., Dong, L., & Carmona-  
 1376 Moreno, C. (2010, Jun). The influence of vegetation, fire spread and fire  
 1377 behaviour on biomass burning and trace gas emissions: results from a process-  
 1378 based model. *Biogeosciences*, 7(6), 1991–2011. doi: 10.5194/bg-7-1991-2010
- 1379 Tyukavina, A., Hansen, M. C., Potapov, P. V., Krylov, A. M., & Goetz, S. J. (2016,  
 1380 Feb). Pan-tropical hinterland forests: mapping minimally disturbed forests.  
 1381 *Global Ecol. Biogeogr.*, 25(2), 151–163. doi: 10.1111/geb.12394
- 1382 Tyukavina, A., Hansen, M. C., Potapov, P. V., Stehman, S. V., Smith-Rodriguez,  
 1383 K., Okpa, C., & Aguilar, R. (2017, Apr). Types and rates of forest distur-  
 1384 bance in Brazilian Legal Amazon, 2000–2013. *Sci. Adv.*, 3(4), e1601047. doi:  
 1385 10.1126/sciadv.1601047
- 1386 Uhl, C., & Buschbacher, R. (1985, Dec). A disturbing synergism between cattle  
 1387 ranch burning practices and selective tree harvesting in the eastern Amazon.  
 1388 *Biotropica*, 17(4), 265–268. doi: 10.2307/2388588
- 1389 Uhl, C., & Kauffman, J. B. (1990, Apr). Deforestation, fire susceptibility, and poten-  
 1390 tial tree responses to fire in the Eastern Amazon. *Ecology*, 71(2), 437–449. doi:  
 1391 10.2307/1940299
- 1392 van der Ent, R. J., Savenije, H. H. G., Schaeffli, B., & Steele-Dunne, S. C. (2010,  
 1393 Sep). Origin and fate of atmospheric moisture over continents. *Water Resour.*

- 1394 *Res.*, 46(9), W09525. doi: 10.1029/2010WR009127
- 1395 VanWey, L. K., D’Antona, A. O., & Brondízio, E. S. (2007, Jan). Household de-  
1396 mographic change and land use/land cover change in the Brazilian Amazon.  
1397 *Popul. Environ.*, 28(3), 163–185. doi: 10.1007/s11111-007-0040-y
- 1398 Veríssimo, A., Barreto, P., Mattos, M., Tarifa, R., & Uhl, C. (1992, Dec). Logging  
1399 impacts and prospects for sustainable forest management in an old Amazonian  
1400 frontier: The case of Paragominas. *Forest Ecol. Manag.*, 55(1–4), 169–199. doi:  
1401 10.1016/0378-1127(92)90099-U
- 1402 Vincent, G., Antin, C., Laurans, M., Heurtebize, J., Durrieu, S., Lavalley, C., &  
1403 Dautzat, J. (2017, Sep). Mapping plant area index of tropical evergreen for-  
1404 est by airborne laser scanning. a cross-validation study using LAI2200 optical  
1405 sensor. *Remote Sens. Environ.*, 198, 254–266. doi: 10.1016/j.rse.2017.05.034
- 1406 von Caemmerer, S. (2000). *Biochemical models of leaf photosynthesis* (No. 2).  
1407 Collingwood, VIC, Australia: CSIRO Publishing. doi: 10.1006/anbo.2000  
1408 .1296
- 1409 von Randow, C., Manzi, A. O., Kruijt, B., de Oliveira, P. J., Zanchi, F. B., Silva,  
1410 R. L., ... Kabat, P. (2004, Jun). Comparative measurements and sea-  
1411 sonal variations in energy and carbon exchange over forest and pasture  
1412 in south west amazonia. *Theor. Appl. Climatol.*, 78(1–3), 5–26. doi:  
1413 10.1007/s00704-004-0041-z
- 1414 Wagner, F., Rossi, V., Stahl, C., Bonal, D., & Hérault, B. (2013, Nov). Asyn-  
1415 chronism in leaf and wood production in tropical forests: a study combining  
1416 satellite and ground-based measurements. *Biogeosciences*, 10(11), 7307–7321.  
1417 doi: 10.5194/bgd-10-8247-2013
- 1418 Walker, W. S., Gorelik, S. R., Baccini, A., Aragon-Osejo, J. L., Josse, C., Meyer,  
1419 C., ... Schwartzman, S. (2020). The role of forest conversion, degradation,  
1420 and disturbance in the carbon dynamics of Amazon indigenous territories and  
1421 protected areas. *Proc. Natl. Acad. Sci. U. S. A.* (advance online publication)  
1422 doi: 10.1073/pnas.1913321117
- 1423 Wright, I. J., Reich, P. B., Westoby, M., Ackerly, D. D., Baruch, Z., Bongers, F.,  
1424 ... Villar, R. (2004, Apr). The worldwide leaf economics spectrum. *Nature*,  
1425 428(6985), 821–827. doi: 10.1038/nature02403
- 1426 Wright, J. S., Fu, R., Worden, J. R., Chakraborty, S., Clinton, N. E., Risi, C., ...

- 1427 Yin, L. (2017, Aug). Rainforest-initiated wet season onset over the south-  
1428 ern Amazon. *Proc. Natl. Acad. Sci. U. S. A.*, *114*(32), 8481–8486. doi:  
1429 10.1073/pnas.1621516114
- 1430 Wu, M., Schurgers, G., Ahlström, A., Rummukainen, M., Miller, P. A., Smith, B.,  
1431 & May, W. (2017, May). Impacts of land use on climate and ecosystem pro-  
1432 ductivity over the Amazon and the South American continent. *Environ. Res.*  
1433 *Lett.*, *12*(5), 054016. doi: 10.1088/1748-9326/aa6fd6
- 1434 Yang, Y., Donohue, R. J., & McVicar, T. R. (2016, Oct). Global estimation of ef-  
1435 fective plant rooting depth: Implications for hydrological modeling. *Water Re-*  
1436 *sour. Res.*, *52*(10), 8260–8276. doi: 10.1002/2016WR019392
- 1437 Zemp, D. C., Schleussner, C.-F., Barbosa, H. M. J., Hirota, M., Montade, V., Sam-  
1438 paio, G., . . . Rammig, A. (2017, Mar). Self-amplified Amazon forest loss  
1439 due to vegetation-atmosphere feedbacks. *Nat. Commun.*, *8*, 14681. doi:  
1440 10.1038/ncomms14681
- 1441 Zhang, K., Castanho, A. D. d. A., Galbraith, D. R., Moghim, S., Levine, N., Bras,  
1442 R. L., . . . Moorcroft, P. R. (2015, Jul). The fate of Amazonian ecosystems  
1443 over the coming century arising from changes in climate, atmospheric CO<sub>2</sub> and  
1444 land-use. *Glob. Change Biol.*, *21*(7), 2569–2587. doi: 10.1111/gcb.12903

1 Supporting Information for "Impacts of Degradation  
2 on Water, Energy, and Carbon Cycling of the  
3 Amazon Tropical Forests"

Marcos Longo<sup>1</sup>, Sassan Saatchi<sup>2,3</sup>, Michael Keller<sup>2,4,5</sup>, Kevin Bowman<sup>2</sup>, Antonio

Ferraz<sup>2,3</sup>, Paul R. Moorcroft<sup>6</sup>, Douglas C Morton<sup>7</sup>, Damien Bonafant<sup>8</sup>, Paulo

Brando<sup>9,10,11</sup>, Benoît Burbanck<sup>12</sup>, Geraldine Derroire<sup>13</sup>, Maiza N

dos-Santos<sup>5</sup>, Victoria Meyer<sup>2</sup>, Scott Saleska<sup>14</sup>, Susan Trumbore<sup>15</sup>, Gregoire

Vincent<sup>16</sup>

4 <sup>1</sup>NASA Postdoctoral Program Fellow, Jet Propulsion Laboratory, California Institute of Technology, Pasadena CA, United States

5 <sup>2</sup>Jet Propulsion Laboratory, California Institute of Technology, Pasadena, CA, United States

6 <sup>3</sup>Institute of Environment and Sustainability, University of California, Los Angeles, CA, United States

7 <sup>4</sup>International Institute of Tropical Forestry, USDA Forest Service, Rio Piedras, Puerto Rico

8 <sup>5</sup>Embrapa Informatica Agropecuaria, Campinas, SP, Brazil

9 <sup>6</sup>Department of Organismic and Evolutionary Biology, Harvard University, Cambridge, MA, United States

10 <sup>7</sup>NASA Goddard Space Flight Center, Greenbelt, MD, United States

11 <sup>8</sup>Universite de Lorraine, INRAE, AgroParisTech, UMR Silva, F-54000 Nancy, France

12 <sup>9</sup>Department of Earth System Science, University of California, Irvine, CA, United States

13 <sup>10</sup>Woods Hole Research Center, Woods Hole, MA, United States

14 <sup>11</sup>Instituto de Pesquisa Ambiental da Amazonia, Brasilia, DF, Brazil

15 <sup>12</sup>INRAE, UMR 0745 EcoFoG, Campus Agronomique, Kourou 97379, France

16 <sup>13</sup>CIRAD, UMR EcoFoG (AgroParisTech, CNRS, INRAE, Univ. Antilles, Univ. Guyane), Kourou 97379, France

17 <sup>14</sup>University of Arizona, Tucson, AZ, United States

18 <sup>15</sup>Max-Planck-Institut für Biochemie, Jena, Germany

## Contents to this file

- 20 1. Text S1 to S3
- 21 2. Figures S1 to S21
- 22 3. Table S1 to S4

## Additional Supporting Information (Files uploaded separately)

- 23 1. Captions for Dataset S1

## Introduction

24 This supporting material provides additional information on the study sites, methodol-  
25 ogy, and results in the main text. Text S1 contains additional information on the airborne  
26 lidar and forest inventory plot data used in this study. Text S2 summarizes changes in  
27 the ED-2.2 model to improve the representation of forest structure and ecosystem func-  
28 tioning. Text S3 describes in detail the steps needed to obtain ED-2.2 initial conditions  
29 from airborne lidar.

30 Figure S1, S2 and S3 provide additional evaluation of the airborne lidar initialization,  
31 specifically the distribution of functional groups, the vertical leaf area index profile, and  
32 the evaluation of plots affected by reduced-impact logging in region BTE. Figure S4-  
33 S9 complement the ED-2.2 model evaluation against eddy covariance towers, comparing

---

34 fortnightly averages for multiple energy, water, and carbon cycle variables. Figure S10  
35 shows the differences in the average seasonal cycle of daytime ground temperature for  
36 all the regions simulated by ED-2.2, as functions of the degradation history. Figure S11  
37 shows the ED-2.2 predictions of average seasonal cycle of gross primary productivity as  
38 functions of local (patch) aboveground biomass for all focus regions. Figure S12 shows  
39 the distribution of evapotranspiration as function of local (patch) biomass and age since  
40 last disturbance, during the wet and dry seasons, for three selected regions across the  
41 precipitation gradient. Figure S13 shows the local (patch) distribution of leaf area index  
42 as a function of aboveground biomass for all the focus regions. Figure S14 shows the  
43 drought severity response of intact and degraded forests in region PRG, for multiple carbon  
44 and energy variables. Figure S15 complements Figure 9 shows how forest flammability  
45 varies as a function of drought length across degradation gradients at additional regions.  
46 Figure S16 is part of Text S2 and shows the fitted allometric models relating height,  
47 diameter at breast height, and individual leaf area, which are used by both the model  
48 initialization and model simulations. Figure S17 and S18 are also part of Text S2 and  
49 show multiple trait relationships derived from multiple data sets and implemented in the  
50 ED-2.2 model. Figure S19 is part of Text S3 and shows an example of how the vertical  
51 distribution of lidar returns is processed to obtain cohorts that are provided to the ED-  
52 2.2 model. Figure S19 is also part of Text S3 and shows the results of cross-validation of  
53 airborne lidar initialization using aggregated forest inventory plot metrics as benchmarks.  
54 Figure S21 is also part of Text S3 and summarizes the distribution of scaling factors to  
55 adjust the non-dimensional leaf area density profiles.

56 Table S1 shows a selection of metrics to assess the ED-2.2 model performance against  
57 multiple energy, water, and carbon cycle variables obtained from the eddy covariance  
58 towers. Table S2 is part of Text S1 and provides additional information of data used for  
59 the ve focus regions and the ancillary regions. Table S3 is part of Text S2 and provides  
60 detailed information on ED-2.2 model settings. Table S4 is part of Text S3 and lists  
61 multiple goodness-of- t statistics for the tted models that relate airborne lidar metrics  
62 and aggregated, area-based forest properties.

#### S1. Additional information on airborne lidar and forest inventory plots

63 Some of the study regions comprised multiple sites, for which airborne lidar data and  
64 disturbance history data were available. Many of these sites also contained forest inven-  
65 tory plots, and have been previously used in studies that quanti ed carbon losses due to  
66 degradation in the Amazon and plant area index estimation (Longo et al., 2016; Vincent  
67 et al., 2017; Rappaport et al., 2018). Table S2 provides additional information on each  
68 speci c site. Further information on plots can be found in Gourlet-Fleury, Ferry, Molino,  
69 Petronelli, and Schmitt (2004) (site PRC), Bonal et al. (2008) (site GFE), Brando et  
70 al. (2012) (site TGE), and Longo et al. (2016), Sustainable Landscapes Brazil (2019) and  
71 dos-Santos, Keller, and Morton (2019) (other sites). To reduce the di erences among plots  
72 regarding size and sampling e ort, we considered only living individuals (trees, lianas, and  
73 palms) with diameter at breast height  $D \geq 10$  cm, and split larger plots (05 6:25 ha)  
74 into sub-plots that were as close to 0.25 ha as possible. The location of all inventories in  
75 Brazil were geo-registered with sub-meter accuracy using di erential Global Navigation  
76 Satellite Systems (GeoXH6000); forest inventories in French Guiana were geo-referenced  
77 with handheld Global Positioning System, with nominal accuracy of 2 m.

78 For the study areas in Brazil, airborne lidar data were collected between 2012 and 2017,  
79 and surveys used Optech ALTM instruments onboard an aircraft flying at average height  
80 of 850m above ground; the sensor scan angle was restricted to 5°-nadir and an average  
81 swath sidelap between flight lines of 65% (Longo et al., 2016); the point cloud data are  
82 publicly available (Sustainable Landscapes Brazil, 2019). Airborne lidar data at GYF  
83 were collected in 2013; the aircraft flew at a height of 550m above ground carrying a Riegl  
84 LMSQ560; the scan angle was capped in 20°-nadir, and the flight line sidelap was near  
85 60% (Vincent et al., 2017). To ensure that the terrain elevation was well characterized,  
86 flights had to meet a minimum return density of 4 m<sup>-2</sup> of 99.5% of the area (except water  
87 bodies and pastures), following previous recommendations for tropical forests (Leitold et  
88 al., 2015).

89 Some of the regions were only used to assist the calibration of the statistical models  
90 (Section S3.2), but not used in the simulations. Because our goal was to characterize  
91 the impacts of degradation on forest structure and ecosystem functioning, we did not  
92 include simulations from MAO, where all surveyed forests were intact, nor did we include  
93 JAM and FST, where all forests were logged (albeit using reduced-impact techniques).  
94 Forests in SFX were not included because the disturbance history based on Landsat  
95 analysis was uncertain due to widespread presence of vines. Finally, at RBR, none of the  
96 surveyed forests could be considered intact or logged using reduced-impact techniques,  
97 which precluded us to have a minimally-disturbed forest as reference.

## S2. Additional ED-2.2 developments

### S2.1. Allometric relations

To obtain an allometric equation for diameter at breast height ( $D$ , cm) as a function of tree height ( $H$ , m), we used all individual tree measurements from the plots included in steps 1 and 2 that were from living trees (excluding lianas and palms), and had field measurements of both  $D$  and  $H$  ( $n = 15865$ ). Because the sampling effort was not even across tree sizes, and to reduce the effects of variability in tree measurements of height along the  $D$  range on local biases, we followed the approach by Jucker et al. (2017) and binned the data into 50 evenly spaced  $\log_e(D)$  classes between  $D = 5$  and  $D = 200$  cm (the range of  $D$  measurements). The binned data were fitted using standardized major axis regression. This choice ensures that the arithmetic inverse relationship (i.e. height as a function of  $D$ ) could be also used in the ED-2.2 model:

$$\log_e(D) = \left\{ \frac{2.01}{\log_e(d_1)} \right\} + \left\{ \frac{1.68}{d_2} \right\} \log_e(H); \quad (\text{S1})$$

where  $H$  should be in m, and  $D$  should be in cm. The model fit is shown in Figure S16a.

We did not have any measurement of individual leaf area ( $m^2_{\text{Leaf plant}^{-1}}$ ) at the study sites, therefore we developed an allometric equation based on the Biomass And Allometry Database (BAAD; Falster et al., 2015). Similar to many allometric equations for aboveground and leaf biomass (e.g., Chave et al., 2014), we used  $D^2(H)$  as the predictor. Because we did not seek a reversible equation, we fitted the model using minimum least squares with heteroskedastic distribution of residuals (Mascaro et al., 2011; Longo et al.,

2016). The fitted model was:

$$L_i = \left( \underbrace{0.234}_{z_1} \underbrace{0.012}_{z_1} \right) D^2 H \left( \underbrace{0.641}_{z_2} \underbrace{0.011}_{z_2} \right) + E_N \quad h = 0; \quad = 0.241 \quad 0.026 L_i^{1.001} \quad 0.056^i; \quad (S2)$$

99 where coefficients are presented in the form Expected Value Standard Error; units for  
 100 the empirical equation should be D in cm, H in m, and  $L_i$  in  $m^2_{\text{Leaf}} \text{plant}^{-1}$ . The model  
 101 fit is shown in Figure S16b.

In ED-2.2, the carbon stocks ( $\text{kgC plant}^{-1}$ ) of different tissues | leaves ( $C_L$ ), fine roots  
 ( $C_R$ ), sapwood ( $C_S$ ), bark ( $C_B$ ) and heartwood ( $C_H$ ) | are defined through allometric  
 equations. Leaf biomass ( $C_L$ ) is obtained from Equation (S2):

$$C_L = \frac{L_i}{\text{SLA}}; \quad (S3)$$

102 where SLA ( $m^2_{\text{Leaf}} \text{kgC}^{-1}$ ) is the individual plant's specific leaf area. Fine-root biomass and  
 103 sapwood biomass are derived from leaf biomass, using the same relationships described in  
 104 Moorcroft, Hurtt, and Pacala (2001). Bark biomass followed a parameterization similar  
 105 to sapwood:

$$C_R = q_R C_L; \quad (S4)$$

$$C_S = q_S H C_L; \quad (S5)$$

$$C_B = q_B H C_L; \quad (S6)$$

106 where  $q_R = 1$  for all plant functional types, following Moorcroft et al. (2001). The leaf-to-  
 107 sapwood ( $q_S$ ) and leaf-to-bark ( $q_B$ ) scaling factors ( $m^{-1}$ ) are determined using the same  
 108 formulation as Falster, FitzJohn, Brannstrom, Dieckmann, and Westoby (2016):

$$q_S = \frac{c_{\text{SLA}} \text{SLA}_w 1000}{A_{L:S}}; \quad (S7)$$

$$q_B = \frac{c \text{SLA}_B 1000}{A_{L:B}} \quad (\text{S8})$$

109 where  $c$  is an empirical shape parameter based on Falster et al. (2016) parameterization  
 110 for broadleaf trees;  $A_{L:S}$  and  $A_{L:B}$  ( $m_{\text{Leaf}}^2 m_{\text{Bark}}^2$ ) are the leaf:sapwood and leaf:bark area  
 111 ratios, respectively;  $w$  and  $\rho_B$  ( $\text{g cm}^{-3}$ ) are the wood and bark densities, respectively;  
 112  $\rho = 2:0 \text{ kg kgC}^{-1}$  is the oven-dry:carbon biomass ratio; and the factor 1000 is included for  
 113 unit conversion. Values of these parameters are shown in Table S3.

114 The allometric equation for heartwood biomass ( $C_H$ ) was obtained using both the  
 115 pantropical allometric equation for aboveground biomass ( $C_{AG}$ ,  $\text{kgC plant}^{-1}$ ; Chave et  
 116 al., 2014), and that total aboveground biomass is the sum of the biomass of the following  
 117 tissues:

$$C_{AG} = \frac{1}{0:0673} w D^2 H^{0:976} \quad (\text{from Chave et al., 2014}) \quad (\text{S9})$$

$$C_{AG} = C_L + f_{AG} (C_S + C_B + C_H); \quad (\text{S10})$$

where  $f_{AG}$  is the fraction of biomass above ground;  $\rho = 2:0 \text{ kg kgC}^{-1}$  is the oven-  
 dry:carbon biomass ratio; and units for S9 should be:  $w$  in  $\text{g cm}^{-3}$ ,  $D$  in cm,  $H$  in  
 m, and  $C_{AG}$  in  $\text{kgC plant}^{-1}$ . To simplify the implementation of  $C_H$  in ED-2.2, we used  
 Equations (S9), (S10) and (S1) to find  $C_H$  at  $D = 10$  cm (typical minimum diameter  
 measured in inventories) and at  $H = 46$  m (maximum height allowed for tropical trees)  
 and derive a function for  $C_H$  with the same form and units as Equation (S9):

$$C_H = \frac{1}{0:0608} w D^2 H^{1:004}; \quad (\text{S11})$$

## S2.2. Changes in the photosynthesis module

118 The photosynthesis module in ED-2.2 has been previously described in detail in (Longo,  
 119 Knox, Medvigy, et al., 2019); here we show only a brief overview and highlight the

120 main modifications. Similarly to previous versions, the net CO<sub>2</sub> assimilation rate (A,  
121 molCO<sub>2</sub>m<sup>-2</sup>s<sup>-1</sup>) for C<sub>3</sub> plants is defined as:

$$A = V_c - \frac{1}{2}V_o - R; \quad (S12)$$

$$V_o = \frac{2}{\Gamma} V_c; \quad (S13)$$

$$= \frac{\Gamma}{2}; \quad (S14)$$

122 where V<sub>c</sub>, V<sub>o</sub>, and R (molCO<sub>2</sub>m<sup>-2</sup>s<sup>-1</sup>) are the carboxylation, oxygenation (photorespira-  
123 tion) and day respiration rates, respectively; Γ (molCO<sub>2</sub>mol<sup>-1</sup>) is the CO<sub>2</sub> compensation  
124 point; Γ<sub>i</sub> (molCO<sub>2</sub>mol<sup>-1</sup>) is the intercellular CO<sub>2</sub> concentration; Γ<sub>o</sub> = 0.209 molO<sub>2</sub>mol<sup>-1</sup> is the oxygen mixing  
125 ratio; and R is the carboxylase:oxygenase ratio. The terms V<sub>c</sub>, V<sub>o</sub>, and R are calculated the  
126 same way as in (Longo, Knox, Medvigy, et al., 2019). The carboxylation rate V<sub>c</sub> depends  
127 on environmental constraints, which ultimately limits the net assimilation rate A.

The maximum carboxylation rate given temperature V<sub>c</sub><sup>max</sup> is defined as in Longo,  
Knox, Medvigy, et al. (2019):

$$V_c^{\max} = \frac{V_{c15}^{\max} Q_V^{\frac{T - T_{15}}{10}}}{f1 + \exp[-f(T - T_c)]g f1 + \exp[+f(T - T_h)]g}; \quad (S15)$$

128 where V<sub>c15</sub><sup>max</sup> (mol m<sup>-2</sup>s<sup>-1</sup>) is V<sub>c</sub><sup>max</sup> at temperature T<sub>15</sub> = 288.15 K (15 C); T (K) is the  
129 leaf temperature; Q<sub>V</sub> determines the steepness of the temperature dependence of V<sub>c</sub><sup>max</sup>; f ,  
130 T<sub>c</sub>, and T<sub>h</sub> are phenomenological parameters that reduce V<sub>c</sub><sup>max</sup> at extreme temperatures,  
131 following the same formulation used in previous ED versions (Moorcroft et al., 2001;  
132 Longo, Knox, Medvigy, et al., 2019).

The maximum carboxylation rate can never be achieved because CO<sub>2</sub> inhibits oxygena-  
tion, and O<sub>2</sub> inhibits carboxylation (von Caemmerer, 2000). The carboxylation rate at

saturated Ribulose-1,5-Biphosphate (RuBP) conditions ( $V_c^{RuBP}$ ) is determined as:

$$V_c^{RuBP} = V_c^{max} \frac{C_i}{C_i + K_c \left(1 + \frac{O}{K_o}\right)}; \quad (S16)$$

where  $K_c$  ( $\text{molCO}_2 \text{mol}^{-1}$ ) and  $K_o$  ( $\text{molO}_2 \text{mol}^{-1}$ ) are the Michaelis constants for carboxylation and oxygenation, respectively, and are also calculated as in (Longo, Knox, Medvigy, et al., 2019). Equation (S16) is the same described in (Longo, Knox, Medvigy, et al., 2019).

The RuBP regeneration depends on the electric transport rate ( $J$  ( $\text{mol m}^{-2} \text{s}^{-1}$ )), which in turns depends on the absorbed irradiance ( $I$  ( $\text{mol m}^{-2} \text{s}^{-1}$ )). If  $I$  is relatively low, then RuBP pools may decline, limiting the carboxylation rate. The RuBP-limited (also known as light-limited) carboxylation rate ( $V_c^{PAR}$ ) is defined as in von Caemmerer (2000):

$$V_c^{PAR} = \frac{J}{4 + 8 \frac{J}{C_i}}; \quad (S17)$$

and  $J$  is determined from an empirical quadratic equation (von Caemmerer, 2000; Oleson et al., 2013):

$$J = \frac{(I_{PSII} + J^{max})^h (I_{PSII} + J^{max})^2 - 4 I_{PSII} J^{max} i^{\frac{1}{2}}}{2 i}; \quad (S18)$$

$$J^{max} = \frac{J_{15}^{max} Q_J \frac{T - T_{15}}{10}}{f_1 + \exp[-f_c (T - T_c)] g f_1 + \exp[+f_h (T - T_h)] g}; \quad (S19)$$

$$I_{PSII} = \frac{1}{2} \phi_{PSII} I; \quad (S20)$$

where  $J^{max}$  ( $\text{mol m}^{-2} \text{s}^{-1}$ ) is the temperature-dependent maximum electron transport rate;  $J_{15}^{max}$  and  $Q_J$  are the equivalent of  $V_{c15}^{max}$  and  $Q_V$  for the electron transport rate, respectively;  $I_{PSII}$  ( $\text{mol m}^{-2} \text{s}^{-1}$ ) is the light effectively used by the photosystem II;  $i = 0.7$  is an empirical curvature parameter (von Caemmerer, 2000; Oleson et al., 2013);  $\phi_{PSII} = 0.85$  is the quantum yield of the photosystem II (von Caemmerer, 2000; Oleson et al., 2013);

and  $T_c$ ,  $T_h$ ,  $f_c$ , and  $f_h$  are empirical parameters to downscale photosynthetic activity at extreme temperatures (Table S3). Unlike the original implementation  $\alpha f_c^{PAR}$  (Moorcroft et al., 2001; Longo, Knox, Medvigy, et al., 2019) the explicit representation on electron transport rate is advantageous because it accounts for the differences in temperature dependence of  $J^{max}$  and  $V_c^{max}$  (von Caemmerer, 2000), and the saturation behavior of  $A$  becomes non-limiting.

In addition to light limitation, carboxylation rates may be limited by the triose phosphate utilization (TPU) for synthesizing sugars and starch (von Caemmerer, 2000). The TPU limitation typically occurs when both  $CO_2$  mixing ratio and irradiance are high, or when temperature is low (von Caemmerer, 2000; Lombardozzi et al., 2018), and is expected to become more important as atmospheric  $CO_2$  increases (Lombardozzi et al., 2018). The TPU-limited carboxylation rate ( $V_c^{TPU}$ ) is defined as:

$$V_c^{TPU} = 3 E_{TP} \frac{C_i}{C_s}; \quad (S21)$$

where  $E_{TP}$  ( $\text{mol m}^{-2} \text{s}^{-1}$ ) is the export rate of triose phosphate from chloroplasts, and is normally parameterized as a function of  $V_c^{max}$  ( $E_{TP} = \epsilon E V_c^{max}$ ; von Caemmerer, 2000; Oleson et al., 2013; Lombardozzi et al., 2018).

Similar to previous versions of ED-2, the net assimilation rate is determined through a law of minimum:

$$A = \min \left( A^{RuBP}; A^{PAR}; A^{TPU} \right) \quad (S22)$$

where each of the cases on the right-hand side are calculated from Equations (S12) and (S13), by replacing  $V_c$  with each of the cases (Equations (S16), (S17), and (S21)), and using the algorithm described in Longo, Knox, Medvigy, et al. (2019).

Both  $J_{15}^{\max}$  and  $E_{TP}$  are assumed to be proportional to  $V_{c15}^{\max}$ . To obtain the proportionality ratios, we used the data collected at multiple sites in Panama (Gu et al., 2016; Norby et al., 2017). Even though the Norby et al. (2017) provided  $\alpha$ s relating these quantities, we refitted the functions to eliminate the intercept, and corrected for the fact that Norby et al. (2017) provides values at 25°C and ED-2.2 needs the reference at 15°C:

$$V_c^{\max} (J_{15}^{\max} = \alpha_J V_{c15}^{\max})$$

The values of  $\alpha_J$  and  $\alpha_E$  are determined from the data collected at multiple sites in Panama and described in Norby et al. (2017). Although Norby et al. (2017) provided empirical  $\alpha$ s relating  $V_c^{\max}$ ,  $J^{\max}$  and  $E_{TP}$ , we obtained the relationships using standardized major axis (SMA) to account for the variability on both variables, and corrected for the fact that Norby et al. (2017) values use a different reference temperature (25°C):

$$\alpha_J = \frac{J_{25}^{\max}}{V_{c25}^{\max}} \frac{Q_V}{Q_J}; \quad (S23)$$

$$\alpha_E = \frac{E_{TP}}{V_{c25}^{\max}}; \quad (S24)$$

where  $J_{25}^{\max}$  and  $V_{c25}^{\max}$  are the values at 25°C, obtained directly from Gu et al. (2016). The SMA line, coefficients  $\alpha_J^0$  and  $\alpha_E$  and the  $R^2$  are shown in Figure S17.

### S2.3. Updated trait and trade-off relationships

In ED-2.2, we represent the functional diversity within ecosystems by defining multiple plant functional types (PFTs). PFTs are defined by both morphological characteristics (e.g. tree or grass) and by a set of traits that determine a variety of life strategies within the ecosystems. Many traits and trade-offs of tropical forest PFTs had not been changed since the original ED-1.0 release (Moorcroft et al., 2001), despite the increase in data availability for the tropics. Here, we aggregated data from multiple trait-based studies

and trait data bases such as GLOPNET and TRY (Wright et al., 2004; Santiago & Wright, 2007; Chave et al., 2009; Kattge et al., 2009, 2011, 2020; Baraloto et al., 2010; Powers & Ti n, 2010; Bahar et al., 2017; Norby et al., 2017), to revise the values associated with each PFT. To remove confounding factors such as canopy position, we only used data for sun leaves, or individuals that were either emergent or canopy trees.

Wood density was the most widely available trait in our data base, and also the indicative trait used to define PFTs in ED-1.0 (Moorcroft et al., 2001). To re-define the PFTs, we used the data from all forest inventory plots available, attributed wood density for each individual using the wood density data base compiled by Chave et al. (2009). We then calculated the probability distribution function of wood density (weighted by basal area), and split the distribution based on quantiles (the lower, middle, and upper 33% of the distribution associated with early-successional, mid-successional, and late-successional trees, respectively). The expected values of wood density for each PFT was assumed to be the mid-point within each quantile (i.e. 16.67%, 50%, and 83.33% quantiles, respectively).

To determine the trade-off axes between traits, we fitted standardized major axes (SMA). Because most wood density data came from the Chave et al. (2009) compilation (only wood density data were available), we aggregated data to species to seek relationships between wood density and other traits. Most traits were not correlated with wood density: leaf turnover rate showed the most significant, yet weak correlation with wood density (Figure S18a). For leaf traits, we were able to obtain large number of paired observations (i.e. two trait measurements from the same individual) between specific leaf area (SLA) and the other traits, and thus we fitted the standardized major axes using SLA as one of the variables (Figure S18b, S18c, and S18d).

198 The revised trait values for the plant functional types used in these simulations are  
199 shown in Table S3.

### S3. ED-2.2 initial conditions using airborne lidar

200 The approach to obtain initial conditions for ED-2 using airborne lidar data is summa-  
201 rized in three steps: (1) derivation of unscaled vertical profiles of leaf area density from the  
202 vertical distribution of returns, and the height-dependent proportion of leaf area density  
203 allocated to each plant functional type; (2) estimation of plot-level properties of the forest  
204 (biomass, basal area, and individual's stem density) from airborne lidar; (3) optimization  
205 of scaling factors to obtain absolute leaf area density profiles and the initial conditions for  
206 ED-2. This approach requires only representative, geo-referenced forest inventory plots  
207 for calibration, and small-footprint, discrete-return airborne lidar point cloud data with  
208 high density of returns, in addition to knowledge of individual-based allometric equations  
209 that relate diameter at breast height ( $D$ ) to tree height, above-ground biomass and leaf  
210 biomass.

#### S3.1. Vertical foliage profiles

211 To obtain vertical profiles of leaf area density (Figure 2, Box 1) across the areas surveyed  
212 by airborne lidar, we first clipped the full point cloud domain into 50 × 50 m columns. For  
213 each column, we simulated a pseudo-waveform from the discrete point clouds to create a  
214 continuous and smooth distribution of return energy in the vertical (see one example in  
215 Figure S19a). Our simulated waveform function  $E(z)$  is based on the algorithm described  
216 by Popescu, Zhao, Neuenschwander, and Lin (2011) and Hancock et al. (2019):

$$E(h_i) = X(h) Z(h; h_i); \quad (\text{S25})$$

$$X(h) = \begin{cases} 1 & \text{if } h_n \in [h - \frac{h}{2}, h + \frac{h}{2}] \\ 0 & \text{otherwise} \end{cases} \quad (S26)$$

$$Z(h; h_i) = \frac{1}{h} \exp\left(-\frac{(h - h_i)^2}{2 \frac{h}{h}}\right) \quad (S27)$$

217 where  $h_i$  is the mean elevation of each bin;  $h = 10$  cm is the thickness of each bin layer;  
 218  $X(h)$  is the energy distribution function across the laser beam trajectory (horizontal);  
 219  $Z(h)$  is the energy distribution function in the vertical (i.e. along the laser beam trajec-  
 220 tory);  $\sigma_z$  is the pulse width in the vertical, which controls the smoothness of the simulated  
 221 waveform; and  $\otimes$  is the convolution operator. Similar to Hancock et al. (2019), we binned  
 222 the return counts before applying the convolution to improve computational efficiency.  
 223 When the goal is to simulate the signal of large-footprint waveform lidar (e.g. GLAS or  
 224 GEDI), the energy distribution function across the laser beam trajectory is frequently  
 225 assumed Gaussian (Blair & Hofton, 1999; Popescu et al., 2011; Hancock et al., 2019). In  
 226 our case, however, we sought to characterize the average vegetation profile for the entire  
 227 column and assumed a uniform (rectangular) distribution across the entire column area  
 228 instead (Eq. S26). In addition, as we will discuss in later in this text, it is important  
 229 that the waveform is not excessively noisy to obtain realistic leaf area index, yet it should  
 230 retain sufficient features to ensure the vegetation structure is not overly aggregated (Fig-  
 231 ure S19a). We defined  $h_n = 50$  cm which resulted in a good compromise in preliminary  
 232 tests. Finally, following Hancock et al. (2019), we calculated the waveform functions for  
 233 vegetation ( $E_v$ ) and ground ( $E_g$ ) returns separately, in order to obtain the integrated  
 234 return energy ( $R_v$  and  $R_g$ ):

$$R_v(h_i) = \sum_{j=i}^{N_i} E_v(h_j); \quad (S28)$$

$$R_g = \sum_{j=1}^{N_l} E_g(h_j); \quad (S29)$$

where  $N_l$  is the total number of layers. In our case, we defined layers up to  $h_T = 70$  m to ensure that the tallest sampled trees would be completely characterized.

To obtain the relative vertical distribution of leaf area density ( $\rho(h)$ ;  $m^2_{Leaf} m^{-2}$ ), we applied the Beer-Lambert light extinction approach, following the approach originally developed by MacArthur and Horn (1969) and adapted for lidar profiles (e.g., Ni-Meister et al., 2001; Stark et al., 2012; Antonarakis et al., 2014). In this approach,  $\rho(h)$  is a function of the gap probability ( $P$ , non-dimensional):

$$\rho(h) = \frac{\cos^2 \theta}{G(h; \theta)} \frac{1}{P(h; \theta)} \frac{\partial P(h; \theta)}{\partial h}; \quad (S30)$$

where  $h$  is the height,  $\theta$  is the angle of incident light, and  $G(h; \theta)$  is the leaf area projection factor. For most lidar surveys used in this study, the maximum  $\theta$ -nadir scan angle was 5:5 (Longo et al., 2016); the only exception was Paracou (GYF), where the  $\theta$ -nadir angle was 20 (Vincent et al., 2017). As a first approximation, we assumed  $\theta = 0$ , and thus  $P(h; \theta) = P(h)$ , but we acknowledge that this introduces an error (5–8% for 10% of the points at GYF). The leaf area projection factor is dependent upon the mean leaf orientation. For simplicity, we assumed isotropic (random) orientation, i.e.  $G(h; \theta) = 0.5$  (Ni-Meister et al., 2001; Vincent et al., 2017).

Following Ni-Meister et al. (2001), the vertical profile of gap probability can be described by the integral of the lidar return energy [ $R_v(h)$ ] between height  $h$  and the top canopy height ( $h_T$ ):

$$\frac{dR_v(h)}{dh} = J_{0r_v} \frac{dP(h)}{dh}; \quad (S31)$$

where  $J_0$  is the irradiance emitted by the lidar sensor and  $r_v$  is the canopy reflectivity. Using the boundary conditions at the top canopy  $R_v(h_T) = 0$ ;  $P(h_T) = 1$ ] and that the total energy reflected by the ground is proportional to the total gap fraction, we obtain:

$$R_v(h_i) = J_0 r_v [1 - P(h_i)]; \quad (S32)$$

$$R_{v0} = J_0 r_v [1 - P(h = 0)]; \quad (S33)$$

$$R_g = J_0 r_g P(h = 0); \quad (S34)$$

where  $r_g$  is the soil reflectivity and  $R_{v0} = R_v(h = 0)$ . The irradiance emitted by the sensor ( $J_0$ ) is not provided in the data set, however it is possible to combine Equations (S32)-(S34) to suppress  $J_0$  from the definition of  $P(h)$ :

$$P(h_i) = 1 - \frac{R_v(h_i)}{R_{v0} + k_r R_g}; \quad (S35)$$

where  $k_r = \frac{r_v}{r_g}$ , the ratio between vegetation and ground reflectivities. By substituting Equations (S31), (S33), and (S35) into Equation (S30) for the  $\theta = 0$ ;  $G = 0.5$  case, we obtain:

$$h = 2 \frac{d}{dh} \ln [R_{v0} + k_r R_g - R_v(h)]; \quad (S36)$$

It is possible to determine  $k_r$  from airborne lidar surveys that have reflectance data (Antonarakis et al., 2014), or from optimization using independent local measurements of leaf area index (Stark et al., 2012). Neither information is easily obtained for large areas, and thus we assumed  $k_r = 1.03$ , following Tang and Dubayah (2017). We found that the results are not sensitive to small variations in  $k_r$ , particularly when the gap fraction is low. On the other hand, the approximation of return counts is only a proxy to the return energy, and therefore, we assumed that the profile obtained from Equation (S36) was considered unscaled, and will be referred as  $\hat{s}^2(h)$ . Following Shao, Stark, de Almeida,

270 and Smith (2019), we excluded the profile below 5 m, as estimates of leaf area density  
271 near the surface often show large uncertainty due to the limited fraction of returns near  
272 the surface in denser canopies.

273 Cohorts in ED-2 are defined as discrete groups of individuals with similar size and same  
274 life strategy (plant functional type; PFT). To separate the vertical profile into discrete  
275 layers of similar size, we assumed that the layers with the most significant population can  
276 be identified by local maxima, or by local saddle points when the layers are not completely  
277 separated, as shown in Figure S19b. The boundary between consecutive layers is defined as  
278 either the local minima or inflection points that are not saddle points (Figure S19b). These  
279 features were automatically determined based on the function peaks (package RSEIS, Lees,  
280 2017), which was modified to capture inflection points and local minima.

281 The last stage of step 1 was to attribute the fraction of each plant functional type  
282 in each vertical layer, which was used to define the cohorts (Figure S19c). Because the  
283 airborne lidar data was from a single band, we could not use spectral mixture analyses  
284 (e.g., Antonarakis et al., 2014). To overcome this limitation, we also simulated waveforms  
285 for all plots that had complete overlap with airborne lidar data in all of the study sites,  
286 and complemented with data from the Sustainable Landscapes Brazil project (Longo et  
287 al., 2016; Sustainable Landscapes Brazil, 2019; dos-Santos et al., 2019) (total of 817  
288 0.25 ha plots). For each plot, we determined the expected relative proportion of each  
289 PFT  $p$  (early-successional, ETR; mid-successional, MTR; and late-successional, LTR) as  
290 a function of height ( $q_p(h)$ ) and the associated profile of return heights and built a look-up  
291 table. The normalized profile of each column was compared with the normalized profile of  
292 all plots in the look-up table using the Kolmogorov-Smirnov test, and the least dissimilar

pro le found in the look-up table was used to determine the relative proportion of PFTs  
in the column of interest (Figure S19c).

### S3.2. Statistical models for plot-level properties

For the second step (Figure 2, Box 2), we developed parametric statistical models that related summary metrics describing the distribution of return heights with four plot-level properties ( $D \leq 10$  cm): aboveground biomass carbon density (ABCD,  $\text{kg m}^{-2}$ ), basal area (BA,  $\text{cm}^2 \text{m}^{-2}$ ), (maximum, allometry-based) leaf area index (LAI,  $\text{m}^2_{\text{Leaf}} \text{m}^{-2}$ ), and stem number density (ND,  $\text{m}^{-2}$ ). Similar to Step 1 (Section S3.1), we considered again all plots that were entirely within the areas surveyed by airborne lidar (total of 817:05 ha plots, Section 3). For each plot-level property, we selected the most informative yet simple model using the subset selection of regression method method (Miller, 1984). Additionally, we only considered models that did not show strong signs of multicollinearity, quantified by the variance inflation factor ( $\text{VIF} < 4$ ). The selected model was fitted assuming heteroskedastic distribution of residuals (Mascaro et al., 2011; Longo et al., 2016). Field inventory above-ground biomass was determined using the same models as in Longo et al. (2016). Individual-based maximum leaf area was determined using an allometric model derived from the Biomass And Allometry Database (BAAD; Falster et al., 2015) and presented in Section S3.3.

We obtained the following models:

$$\begin{aligned}
 \text{ABCD}_{\text{ALS}} &= 0.132^{+0.072}_{-0.045} h^{1.59^{+0.14}_{-0.14}} \\
 + E_N &= 0; \quad = 0.95^{+0.35}_{-0.25} \text{ABCD}_{\text{ALS}}^{0.49^{+0.15}_{-0.13}}; \quad (\text{S37}) \\
 \text{BA}_{\text{ALS}} &= 1.81^{+1.19}_{-0.65} \exp^{h} 5.77^{+1.19}_{-0.94} f_1^{i} h_{75}^{0.85^{+0.12}_{-0.15}}
 \end{aligned}$$

$$+ E_N = 0; = 1:45^{+1:54}_{0:39} BA_{ALS}^{0:39^{0:16}}_{0:26}; \quad (S38)$$

$$LAI_{ALS} = 0:37^{+0:33}_{0:13} \exp^h 5:8^{+1:7}_{2:0} f_{1\ 2:5}^i h^{0:91^{+0:12}}_{0:20} \\ + E_N = 0; = 0:462^{+0:141}_{0:045} LAI_{ALS}^{0:49^{0:14}}_{0:22}; \quad (S39)$$

$$ND_{ALS} = 0:0337^{+0:0053}_{0:0083} \exp^h 8:5^{+2:0}_{1:8} f_{1\ 2:5} + 0:77^{+0:31}_{0:17} F_{7:5}^i \\ + E_N = 0; = 0:038^{+0:069}_{0:027} ND_{ALS}^{0:37^{0:26}}_{0:40}; \quad (S40)$$

311 where  $f_{1\ 2:5}$  is the fraction (range 00 1:0) of returns coming from the layer between 1  
 312 and 25 m;  $F_{7:5}$  is the fraction (range 00 1:0) of returns from above 75 m;  $h_{75}$  is the  
 313 third quartile of the distribution of return heights; and  $h$  is the mean of the distribution  
 314 of return heights. Numbers after the coefficients are the 68% range (equivalent to 1 if  
 315 the distribution was Gaussian) of 1000 replicates using a nested bootstrap sampling. We  
 316 separated the plots by study regions, then for each replicate, we first randomly selected  
 317 which study regions to include in the model fitting stage, then randomly selected plots  
 318 from the these regions. Plots from regions excluded from the model fitting stage were  
 319 used for cross-validation.

320 The fitted models for ABCD, BA, and LAI showed similar-quality fits, and both ex-  
 321 plained over 70% of the inventory-plot variance (Table S4), whereas the model for ND  
 322 explained 64% of the observed variance (Figure S20c; Table S4). Cross-validation assess-  
 323 ment show that all fitted models are robust: models show similar fraction of unexplained  
 324 variance, and none of them are significantly biased (Figure S20; Table S4).

### S3.3. Plot-specific scaling factors and absolute cohort demography

For the third step of this approach (Figure 2, box 3), the unscaled profiles obtained in step 1 were calibrated using the stem number density (ND), basal area (BA) and above-

ground biomass carbon density (ABCD) estimated from the parametric models developed in step 2. First, we obtain the unscaled leaf area index of each cohort layer ( $l_i$ ):

$$l_i = \int_{h_i}^{h_i^+} l(h) dh; \quad (\text{S41})$$

where  $h_i$ ;  $h_i^+$  are the lower and upper bounds of the discrete layer associated with cohort  $i$  (Figure S19). We then estimated the unscaled stem number density of cohort  $i$  ( $n_i$ ,  $\text{m}^{-2}$ ) following the same approach by Antonarakis et al. (2014), which assumes that the leaf area index is directly proportional to  $n_i$ , and individual leaf area ( $L_i$ ,  $\text{m}^2_{\text{Leaf plant}^{-1}}$ ), assumed to be a function of the tree size:

$$n_i = \frac{1}{L_i(D_i; H_{t_i})}; \quad (\text{S42})$$

325 where  $D_i$  (cm) is the diameter at breast height, and  $H$  (m) is the tree height. Neither  
 326  $L_i$  nor  $D_i$  can be directly retrieved by airborne lidar, therefore we developed allometric  
 327 equations based on available data. To be consistent with the ED-2.2 simulations, we used  
 328 the allometric equations for height and individual leaf area described in Supplement S2.1.  
 329 The unscaled stem number density of each cohort ( $n_i$ ) is obtained by substituting  
 330 Equations (S2) and (S1) into Equation (S42):

$$n_i = \frac{1}{L_i(H_i^2)}; \quad (\text{S43})$$

$$L_i = \frac{1}{d_1^2}; \quad (\text{S44})$$

$$H_i = (2d_2 + 1)^{-1}; \quad (\text{S45})$$

331 Once all  $n_i$  values are determined, it is possible to derive unscaled, column-aggregated  
 332 values of aboveground biomass carbon density (ABCD), basal area ( $BA$ ) and stem

number density (ND<sup>2</sup>):

$$ABCD^? = \sum_{i=1}^I n_i^? f_c a_1^n_{p(i)} [D(H)]^2 H^{o_2} ; \tag{S46}$$

$$BA^? = \sum_{i=1}^I n_i^? \frac{1}{4} [D(H)]^2 ; \tag{S47}$$

$$LAI^? = \sum_{i=1}^I f n_i^? g ; \tag{S48}$$

$$ND^? = \sum_{i=1}^I n_i^? ; \tag{S49}$$

where I is the total number of cohorts in the analyzed column, (ETR ; MTR ; LTR ) = (0:450; 0615; 0790) g cm<sup>3</sup> are the wood density values for each PFP(i), and (a<sub>1</sub>; a<sub>2</sub>) = (0:0673; 0976) are the empirical coefficients from the pantropical allometric equation developed by Chave et al. (2014). The unscaled values are compared with the properties estimated using the statistical model using airborne-lidar metrics (Section S3.2), denoted by ND ; BA ; LAI ; ABCD :

$$e_A = \frac{ABCD}{ABCD^?} ; \tag{S50}$$

$$e_B = \frac{BA}{BA^?} ; \tag{S51}$$

$$e_L = \frac{LAI}{LAI^?} ; \tag{S52}$$

$$e_N = \frac{ND}{ND^?} ; \tag{S53}$$

where (e<sub>A</sub>; e<sub>B</sub>; e<sub>L</sub>; e<sub>N</sub>) are the scaling factor that would match the estimates from the third step with estimates from the first step. The minimum overall error when taking all variables into account can be determined from the global minimum of function S based on the weighted least squares:

$$S(e) = \frac{w_A (e - e_A)^2 + w_B (e - e_B)^2 + w_L (e - e_L)^2 + w_N (e - e_N)^2}{w_A + w_B + w_L + w_N} ; \tag{S54}$$

where  $(w_A; w_B; w_L; w_N) = (0.279; 0.251; 0.292; 0.177)$  are the weights of ABCD, BA, LAI, and ND, respectively, and are proportional to the inverse of the fraction of unexplained variance for the full model (Table S4). The scaling factor that minimizes can be determined analytically:

$$e = \frac{w_A \epsilon_A + w_B \epsilon_B + w_L \epsilon_L + w_N \epsilon_N}{w_A + w_B + w_L + w_N}, \quad (\text{S55})$$

which is equivalent to the weighted average of the scaling factors. The scaled number density of each cohort is then assumed to be  $n_i = e n_i^?$ .

### S3.4. General scaling factor

The scaling factor in step 3 (Equation S55) could be obtained for any airborne lidar column, as it only relies on the local vertical profile of returns (Section S3.1) and statistical models based on airborne lidar metrics (Equations S37-S40). However, the statistical models (Equations S37-S40) are based on plots with  $D = 10$  cm, which is relatively high for the most degraded forests. Consequently, the statistical models cannot fully constrain the leaf area density profiles at the most degraded forests, because the return energy above 11 m (equivalent to  $D = 10$  cm) may represent a small fraction of the return energy. To overcome this limitation introduced by the lack of small trees in our forest inventory data set, we sought to define a characteristic scaling factor that could be applied to all lidar scenes. To do so, we used the results from the regional cross validation at all sites (Table S2) to analyze the distribution of scaling factors. The distribution of factors from all the plots are shown in Figure S21. The distribution has a well-defined peak, and the mode of the global distribution is close to the median value  $e_{50} = 1.357$ . Although

355 the distribution of factors vary by each site (Figure S21b), for simplicity we used a single  
356 factor equivalent to the median at all sites.

## References

- 357 Antonarakis, A. S., Munger, J. W., & Moorcroft, P. R. (2014, Jul). Imaging spectroscopy-  
358 and lidar-derived estimates of canopy composition and structure to improve predic-  
359 tions of forest carbon fluxes and ecosystem dynamics. *Geophys. Res. Lett.*, 41(7),  
360 2535-2542. doi: 10.1002/2013GL058373
- 361 Bahar, N. H. A., Ishida, F. Y., Weerasinghe, L. K., Guerrieri, R., O'Sullivan, O. S.,  
362 Bloomfield, K. J., ... Atkin, O. K. (2017, May). Leaf-level photosynthetic capacity  
363 in lowland Amazonian and high-elevation Andean tropical moist forests of Peru. *New  
364 Phytol.*, 214(3), 1002-1018. doi: 10.1111/nph.14079
- 365 Baraloto, C., Paine, C. E. T., Poorter, L., Beauchene, J., Bonal, D., Domenach, A.-M.,  
366 ... Chave, J. (2010, Nov). Decoupled leaf and stem economics in rain forest trees.  
367 *Ecol. Lett.*, 13(11), 1338-1347. doi: 10.1111/j.1461-0248.2010.01517.x
- 368 Blair, J. B., & Hofton, M. A. (1999, Aug). Modeling laser altimeter return waveforms  
369 over complex vegetation using high-resolution elevation data. *Geophys. Res. Lett.*,  
370 26(16), 2509-2512. doi: 10.1029/1999GL010484
- 371 Bonal, D., Bosc, A., Ponton, S., Goret, J.-Y., Burban, B., Gross, P., ... Granier,  
372 A. (2008, Aug). Impact of severe dry season on net ecosystem exchange in the  
373 Neotropical rainforest of French Guiana. *Glob. Change Biol.*, 14(8), 1917-1933. doi:  
374 10.1111/j.1365-2486.2008.01610.x
- 375 Brando, P. M., Nepstad, D. C., Balch, J. K., Bolker, B., Christman, M. C., Coe, M., &  
376 Putz, F. E. (2012, Feb). Fire-induced tree mortality in a neotropical forest: the roles

- 377 of bark traits, tree size, wood density and re behavior. *Glob. Change Biol.* 18(2),  
378 630{641. doi: 10.1111/j.1365-2486.2011.02533.x
- 379 Chave, J., Coomes, D., Jansen, S., Lewis, S. L., Swenson, N. G., & Zanne, A. E. (2009,  
380 Apr). Towards a worldwide wood economics spectrum. *Ecol. Lett.* 12(4), 351{366.  
381 doi: 10.1111/j.1461-0248.2009.01285.x
- 382 Chave, J., Rejou-Mechain, M., Burquez, A., Chidumayo, E., Colgan, M. S., Delitti,  
383 W. B., ... Vieilledent, G. (2014, Oct). Improved allometric models to estimate the  
384 aboveground biomass of tropical trees. *Glob. Change Biol.* 20(10), 3177{3190. doi:  
385 10.1111/gcb.12629
- 386 dos-Santos, M., Keller, M., & Morton, D. (2019, Dec). LIDAR surveys over selected forest  
387 research sites, Brazilian Amazon, 2008{2018. Retrieved 31 Jan 2020, from [https://](https://daac.ornl.gov/cgi-bin/dsviewer.pl?ds_id=1644)  
388 [daac.ornl.gov/cgi-bin/dsviewer.pl?ds\\_id=1644](https://daac.ornl.gov/cgi-bin/dsviewer.pl?ds_id=1644) doi: 10.3334/ORNLDAAC/  
389 1644
- 390 Falster, D. S., Duursma, R. A., Ishihara, M. I., Barneche, D. R., FitzJohn, R. G.,  
391 Varhammar, A., ... York, R. A. (2015, May). BAAD: a biomass and allometry  
392 database for woody plants. *Ecology* 96(5), 1445{1445. doi: 10.1890/14-1889.1
- 393 Falster, D. S., FitzJohn, R. G., Brannstrom, A., Dieckmann, U., & Westoby, M. (2016,  
394 Feb). plant: A package for modelling forest trait ecology and evolution. *Methods*  
395 *Ecol. Evol.*, 7(2), 136{146. doi: 10.1111/2041-210X.12525
- 396 Gourlet-Fleury, S., Ferry, B., Molino, J.-F., Petronelli, P., & Schmitt, L. (2004). Ex-  
397 perimental plots: Key features. In S. Gourlet-Fleury, J.-M. Guehl, & O. Laroussinie  
398 (Eds.), *Ecology and management of a Neotropical rainforest: Lessons drawn from*  
399 *Paracou, a long-term experimental research site in French Guiana* (60). Paris:

- 400 Elsevier.
- 401 Gu, L., Norby, R., Haworth, I., Jensen, A., Turner, B., Walker, A., ... Winter, K.  
 402 (2016). Photosynthetic parameters and nutrient content of trees at the Panama crane  
 403 sites. 1.O. NGEE Tropics data collection Retrieved 12 Sep 2019, from [https://](https://ngt-data.lbl.gov)  
 404 [ngt-data.lbl.gov](https://ngt-data.lbl.gov) doi: 10.15486/NGT/1255260
- 405 Hancock, S., Armston, J., Hofton, M., Sun, X., Tang, H., Duncanson, L. I., ... Dubayah,  
 406 R. (2019, Feb). The GEDI simulator: A large-footprint waveform lidar simulator for  
 407 calibration and validation of spaceborne missions *Earth Space Sci.* 6(2), 290{310.  
 408 doi: 10.1029/2018EA000506
- 409 Hunter, M. O., Keller, M., Vitoria, D., & Morton, D. C. (2013, Dec). Tree height  
 410 and tropical forest biomass estimation. *Biogeosciences* 10(6), 10491{10529. doi:  
 411 10.5194/bg-10-8385-2013
- 412 Jucker, T., Caspersen, J., Chave, J., Antin, C., Barbier, N., Bongers, F., ... Coomes,  
 413 D. A. (2017, Jan). Allometric equations for integrating remote sensing imagery into  
 414 forest monitoring programmes. *Glob. Change Biol.* 23(1), 177{190. doi: 10.1111/  
 415 [gcb.13388](https://doi.org/10.1111/gcb.13388)
- 416 Kattge, J., Bonisch, G., Daz, S., Lavorel, S., Prentice, I. C., Leadley, P., ... Wirth, C.  
 417 (2020, Jan). TRY plant trait database | enhanced coverage and open access *Glob.*  
 418 *Change Biol.* 26(1), 119{188. doi: 10.1111/[gcb.14904](https://doi.org/10.1111/gcb.14904)
- 419 Kattge, J., Daz, S., Lavorel, S., Prentice, I. C., Leadley, P., Bonisch, G., ... Wirth, C.  
 420 (2011, Sep). TRY { a global database of plant traits. *Glob. Change Biol.* 17(9),  
 421 2905{2935. doi: 10.1111/[j.1365-2486.2011.02451.x](https://doi.org/10.1111/j.1365-2486.2011.02451.x)
- 422 Kattge, J., Knorr, W., Raddatz, T., & Wirth, C. (2009, Apr). Quantifying pho-

423 tosynthetic capacity and its relationship to leaf nitrogen content for global-scale  
424 terrestrial biosphere models. *Glob. Change Biol.*, 15(4), 976{991. doi: 10.1111/  
425 j.1365-2486.2008.01744.x

426 Lees, J. M. (2017). RSEIS: Seismic time series analysis tools [Computer software manual].  
427 Retrieved from <https://CRAN.R-project.org/package=RSEIS> (R package version  
428 3.7-4)

429 Leitold, V., Keller, M., Morton, D., Cook, B., & Shimabukuro, Y. (2015, Feb). Airborne  
430 lidar-based estimates of tropical forest structure in complex terrain: opportunities  
431 and trade-offs for REDD+. *Carbon Balance Management* 10(1), 3. doi: 10.1186/s13021  
432 -015-0013-x

433 Lombardozzi, D. L., Smith, N. G., Cheng, S. J., Dukes, J. S., Sharkey, T. D., Rogers, A.,  
434 ... Bonan, G. B. (2018, Jul). Triose phosphate limitation in photosynthesis models  
435 reduces leaf photosynthesis and global terrestrial carbon storage. *Environ. Res. Lett.*,  
436 13(7), 074025. doi: 10.1088/1748-9326/aacf68

437 Longo, M., Keller, M., dos Santos, M. N., Leitold, V., Pinage, E. R., Baccini, A., ...  
438 Morton, D. C. (2016, Nov). Aboveground biomass variability across intact and  
439 degraded forests in the Brazilian Amazon. *Global Biogeochem. Cycle* 30(11), 1639{  
440 1660. doi: 10.1002/2016GB005465

441 Longo, M., Knox, R. G., Levine, N. M., Swann, A. L. S., Medvigy, D. M., Dietze, M. C.,  
442 ... Moorcroft, P. R. (2019, Oct). The biophysics, ecology, and biogeochemistry  
443 of functionally diverse, vertically and horizontally heterogeneous ecosystems: the  
444 Ecosystem Demography model, version 2.2 { part 2: Model evaluation for tropical  
445 South America. *Geosci. Model Dev.* 12(10), 4347{4374. doi: 10.5194/gmd-12-4347

446 -2019

- 447 Longo, M., Knox, R. G., Medvigy, D. M., Levine, N. M., Dietze, M. C., Kim, Y.,  
 448 ... Moorcroft, P. R. (2019, Oct). The biophysics, ecology, and biogeochemistry  
 449 of functionally diverse, vertically and horizontally heterogeneous ecosystems: the  
 450 Ecosystem Demography model, version 2.2 { part 1: Model description *Geosci.*  
 451 *Model Dev.* 12(10), 4309{4346. doi: 10.5194/gmd-12-4309-2019
- 452 MacArthur, R. H., & Horn, H. S. (1969, Sep). Foliage profile by vertical measurements.  
 453 *Ecology* 50(5), 802{804. doi: 10.2307/1933693
- 454 Mascaro, J., Litton, C. M., Hughes, R. F., Uowolo, A., & Schnitzer, S. A. (2011, Nov).  
 455 Minimizing bias in biomass allometry: Model selection and log-transformation of  
 456 data. *Biotropica* 43(6), 649{653. doi: 10.1111/j.1744-7429.2011.00798.x
- 457 Miller, A. J. (1984, Nov). Selection of subsets of regression variables. *J. R. Stat. Soc.*  
 458 *A-Gen.*, 147(3), 389{425. doi: 10.2307/2981576
- 459 Moorcroft, P. R., Hurtt, G. C., & Pacala, S. W. (2001, Nov). A method for scaling veg-  
 460 etation dynamics: The Ecosystem Demography model (EDM). *Ecol. Monogr.* 71(4),  
 461 557{586. doi: 10.1890/0012-9615(2001)071[0557:AMFSVDf]2.0.CO;2
- 462 Ni-Meister, W., Jupp, D., & Dubayah, R. (2001, Sep). Modeling lidar waveforms in  
 463 heterogeneous and discrete canopies. *IEEE T. Geosci. Remote Sens.* 39(9), 1943{  
 464 1958. doi: 10.1109/36.951085
- 465 Norby, R. J., Gu, L., Haworth, I. C., Jensen, A. M., Turner, B. L., Walker, A. P., ...  
 466 Winter, K. (2017, Sep). Informing models through empirical relationships between  
 467 foliar phosphorus, nitrogen and photosynthesis across diverse woody species in trop-  
 468 ical forests of Panama. *New Phytol.* 215(4), 1425{1437. doi: 10.1111/nph.14319

- 469 Oleson, K. W., Lawrence, D. M., Bonan, G. B., Drewniak, B., Huang, M., Koven, C. D.,  
470 ... Yang, Z.-L. (2013). Technical description of version 4.5 of the community land  
471 model (CLM)(Technical Report Nos. NCAR/TN-503+STR). Boulder, CO: NCAR.  
472 (420pp.) doi: 10.5065/D6RR1W7M
- 473 Popescu, S. C., Zhao, K., Neuenschwander, A., & Lin, C. (2011, Nov). Satellite lidar  
474 vs. small footprint airborne lidar: Comparing the accuracy of aboveground biomass  
475 estimates and forest structure metrics at footprint level. *Remote Sens. Environ.*  
476 115(11), 2786{2797. doi: 10.1016/j.rse.2011.01.026
- 477 Powers, J. S., & Ti n, P. (2010, Aug). Plant functional type classi cations in tropical  
478 dry forests in Costa Rica: leaf habit versus taxonomic approaches. *Funct. Ecol.*  
479 24(4), 927{936. doi: 10.1111/j.1365-2435.2010.01701.x
- 480 Rappaport, D., Morton, D., Longo, M., Keller, M., Dubayah, R., & dos-Santos, M. N.  
481 (2018, Jun). Quantifying long-term changes in carbon stocks and forest structure  
482 from Amazon forest degradation. *Environ. Res. Lett.*, 13(6), 065013. doi: 10.1088/  
483 1748-9326/aac331
- 484 Santiago, L. S., & Wright, S. J. (2007, Feb). Leaf functional traits of tropical forest  
485 plants in relation to growth form. *Funct. Ecol.*, 21(1), 19{27. doi: 10.1111/j.1365  
486 -2435.2006.01218.x
- 487 Schwarz, G. (1978, Mar). Estimating the dimension of a model. *Ann. Stat.*, 6(2),  
488 461{464. doi: 10.1214/aos/1176344136
- 489 Shao, G., Stark, S. C., de Almeida, D. R., & Smith, M. N. (2019, Feb). Towards high  
490 throughput assessment of canopy dynamics: The estimation of leaf area structure  
491 in Amazonian forests with multitemporal multi-sensor airborne lidar. *Remote Sens.*

- 492 Environ., 221(221), 1{13. doi: 10.1016/j.rse.2018.10.035
- 493 Stark, S. C., Leitold, V., Wu, J. L., Hunter, M. O., de Castilho, C. V., Costa, F. R. C.,  
494 ... Saleska, S. R. (2012, Dec). Amazon forest carbon dynamics predicted by pro les  
495 of canopy leaf area and light environment. *Ecol. Lett*, 15(12), 1406{1414. doi:  
496 10.1111/j.1461-0248.2012.01864.x
- 497 Sustainable Landscapes Brazil. (2019, Nov). Retrieved 9 Jan 2019, from [https://](https://www.paisagenslidar.cnptia.embrapa.br/webgis/)  
498 [www.paisagenslidar.cnptia.embrapa.br/webgis/](https://www.paisagenslidar.cnptia.embrapa.br/webgis/)
- 499 Tang, H., & Dubayah, R. (2017, Mar). Light-driven growth in Amazon evergreen forests  
500 explained by seasonal variations of vertical canopy structure. *Proc. Natl. Acad. Sci.*  
501 *U. S. A.* , 114(10), 2640{2644. doi: 10.1073/pnas.1616943114
- 502 Vincent, G., Antin, C., Laurans, M., Heurtebize, J., Durrieu, S., Lavalley, C., & Dauzat,  
503 J. (2017, Sep). Mapping plant area index of tropical evergreen forest by airborne  
504 laser scanning. a cross-validation study using LAI2200 optical sensor. *Remote Sens.*  
505 *Environ.*, 198 254{266. doi: 10.1016/j.rse.2017.05.034
- 506 von Caemmerer, S. (2000) *Biochemical models of leaf photosynthesis* (No. 2). Colling-  
507 wood, VIC, Australia: CSIRO Publishing. doi: 10.1006/anbo.2000.1296
- 508 Wright, I. J., Reich, P. B., Westoby, M., Ackerly, D. D., Baruch, Z., Bongers, F., ...  
509 Villar, R. (2004, Apr). The worldwide leaf economics spectrum. *Nature*, 428(6985),  
510 821{827. doi: 10.1038/nature02403

Figure S1. Assessment of basal area by plant functional types (PFTs), for different study regions and degradation levels. Plant functional types are early-successional tropical tree (ETR), mid-successional tropical tree (MTR) and late-successional tropical tree (LTR). Grey bars are obtained from forest inventory plots, and blue bars are obtained from the airborne lidar initialization using a 612-fold regional cross-validation (i.e. excluding all plots from region in the calibration stage). Whiskers correspond to the standard deviation either across all plots in the same category (inventory) or across all plots and replicates (lidar). Sites: GYF { Paracou, PRG { Paragominas, FZN { Feliz Natal, TAN { Tanguro. Disturbance classes: BNx { Burned twice or more, CL1 { conventional logging (once), LB1 { logged and burned once, LTH { logged and thinned, RIL { reduced-impact logging, INT { intact.

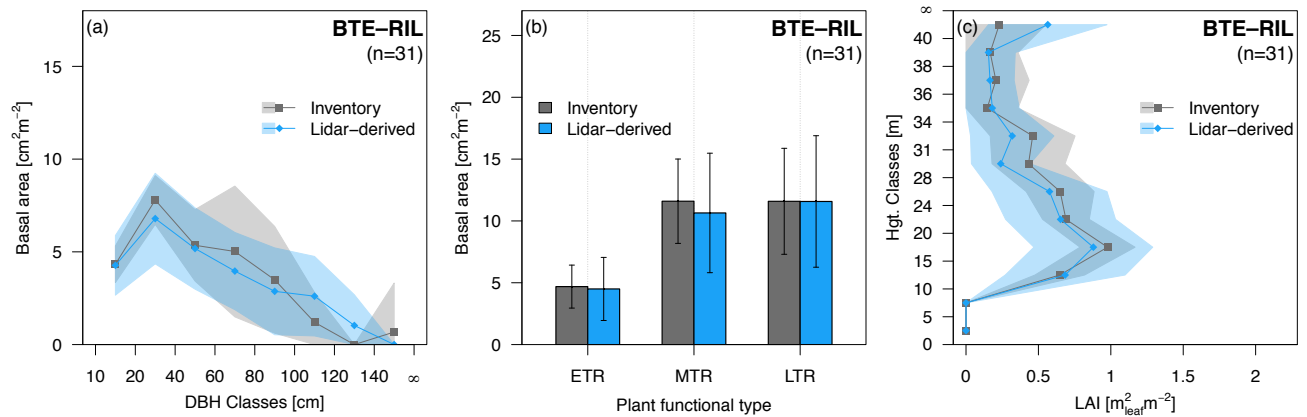


Figure S3. Assessment of airborne lidar initialization for Belterra (BTE). Comparison of (a) basal area distribution across diameter of breast height (DBH) classes, (b) basal area distribution among plant functional types (PFTs), and (c) leaf area index distribution as a function of height, for reduced-impact logging (RIL, the only disturbance type with > 20 plots in BTE). Plant functional types are early-successional tropical tree (ETR), mid-successional tropical tree (MTR) and late-successional tropical tree (LTR). Grey points and bars are obtained from forest inventory plots, and blue points and bars are obtained from the airborne lidar initialization using a 612-fold regional cross-validation (i.e. excluding all plots from region in the calibration stage). Bands around points and whiskers correspond to the standard deviation either across all plots in the same category (inventory) or across all plots and replicates (lidar).

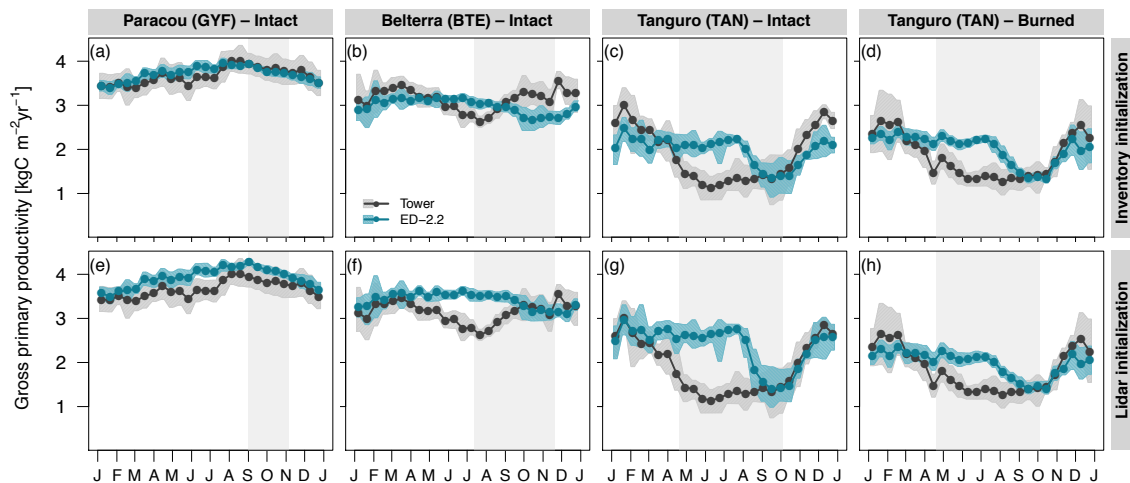


Figure S4. Model assessment of gross primary productivity. Fortnightly averages of gross primary productivity at (a,e) Paracou (GYF), intact forest; (b,f) Belterra (BTE), intact forests; (c,g) Tanguro (TAN), intact forests; (d,h) Tanguro (TAN), burned forests, initialized with (a-d) forest inventory plots and (e-h) airborne lidar. Fortnightly averages for both ED-2.2 and tower estimates were calculated using only hours with available data from the tower, and were integrated by obtaining the mean diurnal cycle then averaging the mean diurnal cycle to avoid biases due to data gaps. Bands around the averages correspond to the 95% confidence interval of the means, obtained through bootstrap. The grey rectangle in the background corresponds to the average dry season.

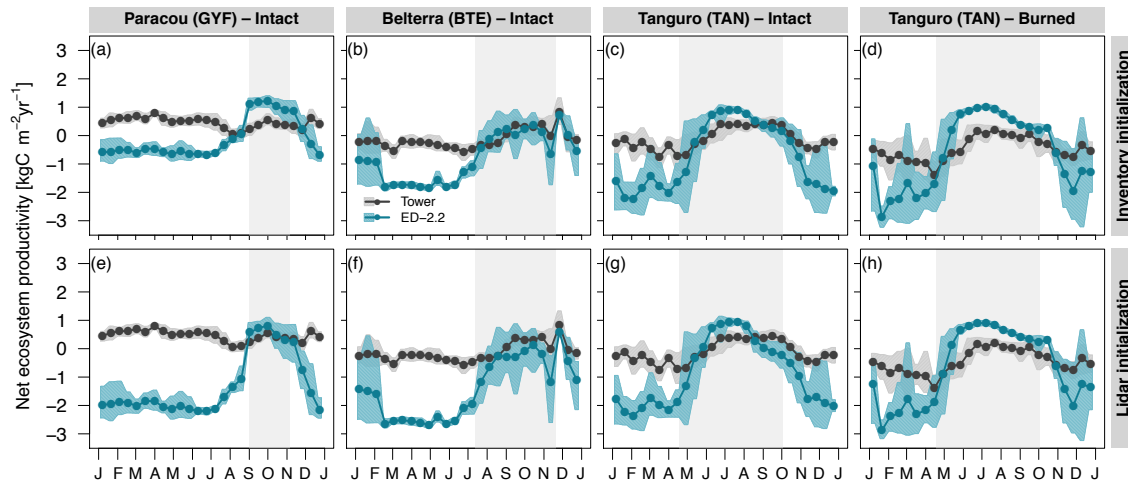


Figure S5. Model assessment of net ecosystem productivity. Fortnightly averages of net ecosystem productivity at (a,e) Paracou (GYF), intact forest; (b,f) Belterra (BTE), intact forests; (c,g) Tanguro (TAN), intact forests; (d,h) Tanguro (TAN), burned forests, initialized with (a-d) forest inventory plots and (e-h) airborne lidar. Positive fluxes mean net uptake. Fortnightly averages for both ED-2.2 and tower estimates were calculated using only hours with available data from the tower, and were integrated by obtaining the mean diurnal cycle then averaging the mean diurnal cycle to avoid biases due to data gaps. Bands around the averages correspond to the 95% confidence interval of the means, obtained through bootstrap. The grey rectangle in the background corresponds to the average dry season.

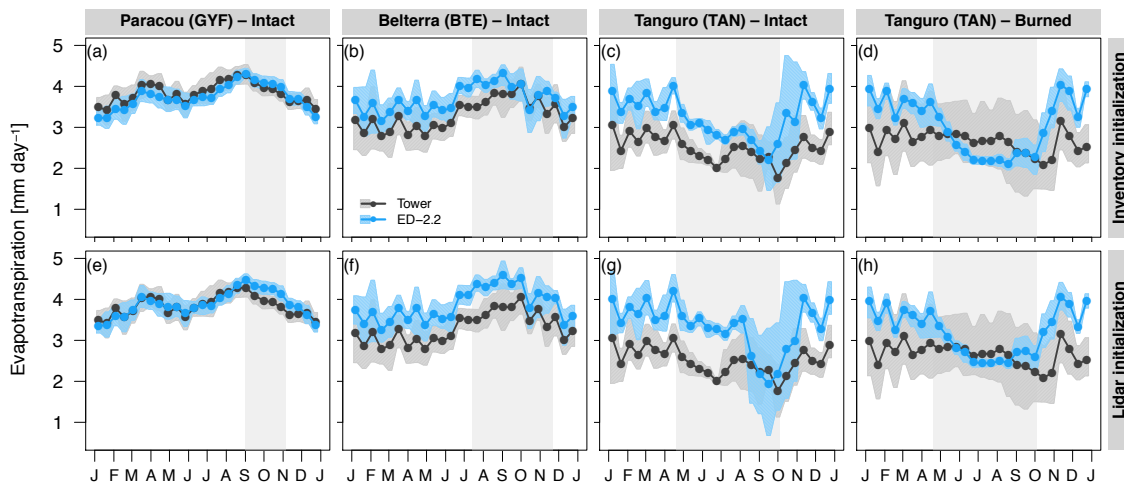


Figure S6. Model assessment of evapotranspiration. Fortnightly averages of water heat flux at (a,e) Paracou (GYF), intact forest; (b,f) Belterra (BTE), intact forests; (c,g) Tanguro (TAN), intact forests; (d,h) Tanguro (TAN), burned forests, initialized with (a-d) forest inventory plots and (e-h) airborne lidar. Fortnightly averages for both ED-2.2 estimates and tower measurements were calculated using only hours with available data from the tower, and were integrated by obtaining the mean diurnal cycle then averaging the mean diurnal cycle to avoid biases due to data gaps. Bands around the averages correspond to the 95% confidence interval of the means, obtained through bootstrap. The grey rectangle in the background corresponds to the average dry season.

Figure S7. Model assessment of sensible heat flux. Fortnightly averages of sensible heat flux at (a,e) Paracou (GYF), intact forest; (b,f) Belterra (BTE), intact forests; (c,g) Tanguro (TAN), intact forests; (d,h) Tanguro (TAN), burned forests, initialized with (a-d) forest inventory plots and (e-h) airborne lidar. Fortnightly averages for both ED-2.2 estimates and tower measurements were calculated using only hours with available data from the tower, and were integrated by obtaining the mean diurnal cycle then averaging the mean diurnal cycle to avoid biases due to data gaps. Bands around the averages correspond to the 95% confidence interval of the means, obtained through bootstrap. The grey rectangle in the background corresponds to the average dry season.

Figure S12. Variability of evapotranspiration (ET) as a function of local (patch) aboveground biomass (AGB). Scatter plot of AGB (x axis) and water flux (y axis) at sites (a,d) Paracou (GYF), (b,e) Paragominas (PRG), (c,f) Feliz Natal (FZN), for (a-c) the peak of wet season | May (GYF), March (PRG), and February (FZN) | and (d-f) peak of dry season | October (GYF and PRG), and August (FZN). Each point represents the 1980{2016 average ET of each patch solved by ED-2.2; point shapes correspond to the disturbance history, and point colors represent the time between the last disturbance (undetermined for intact forests) and lidar data acquisition. Curves correspond to non-linear least squares fits of the most parsimonious function, defined from Bayesian Information Criterion (Schwarz, 1978), between shifted exponential or shifted Weibull functions.

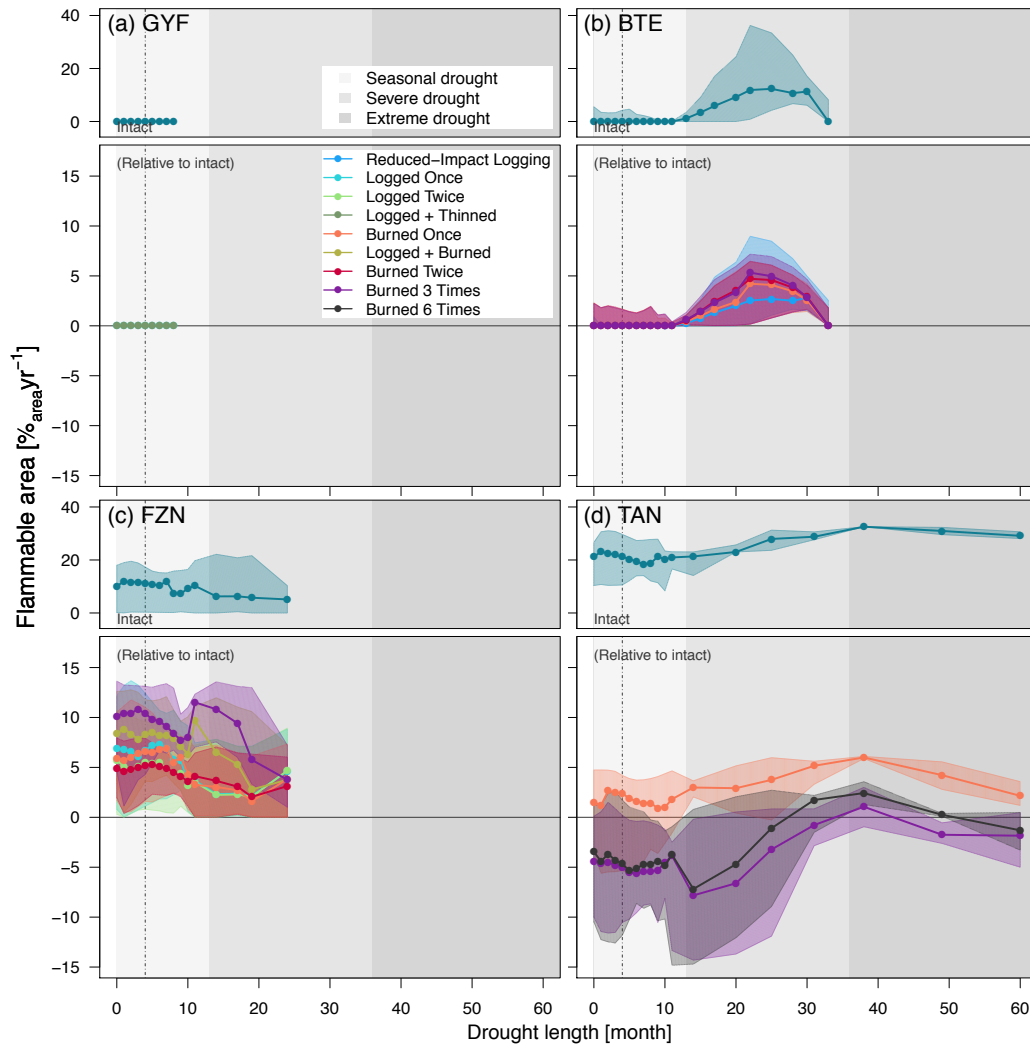


Figure S15. Flammable area as a function of degradation history and drought length (number of consecutive months with water deficit in excess of 20 mm) for regions (a) Paracou (GYF), (b) Belterra (BTE), (c) Feliz Natal (FZN), and (d) Tanguro (TAN). Points correspond to the median value of 12-month running averages, aggregated into quantiles along the drought length. Bands around the points correspond to the 95% range within each drought length bin. Top panels are the absolute value for intact forests, and bottom panels are the absolute difference between degraded and intact forests. Background shades denote drought-length classes used in the text: seasonal (light gray, less than 12 months); severe (intermediate gray, 12{36 months); extreme (dark gray; more than 36 months).

Figure S16. Fit of the allometric equations developed for the airborne lidar initialization and for ED-2.2 simulations. (a) Diameter at breast height ( $D$ ) as a function of tree height ( $H$ ); line corresponds to the standardized major axis equation defined by Equation (S1). (b) Individual leaf area ( $L$ ) as a function of size ( $D^2H$ ). Shaded background corresponds to the density of observed points. The results of the binned sampling with the lowest root mean square error are also shown: blue dots correspond to the binned sampled points used for the model fitting, black lines are the fitted model, and the goodness-of-fit metrics for the cross validation are shown for reference.

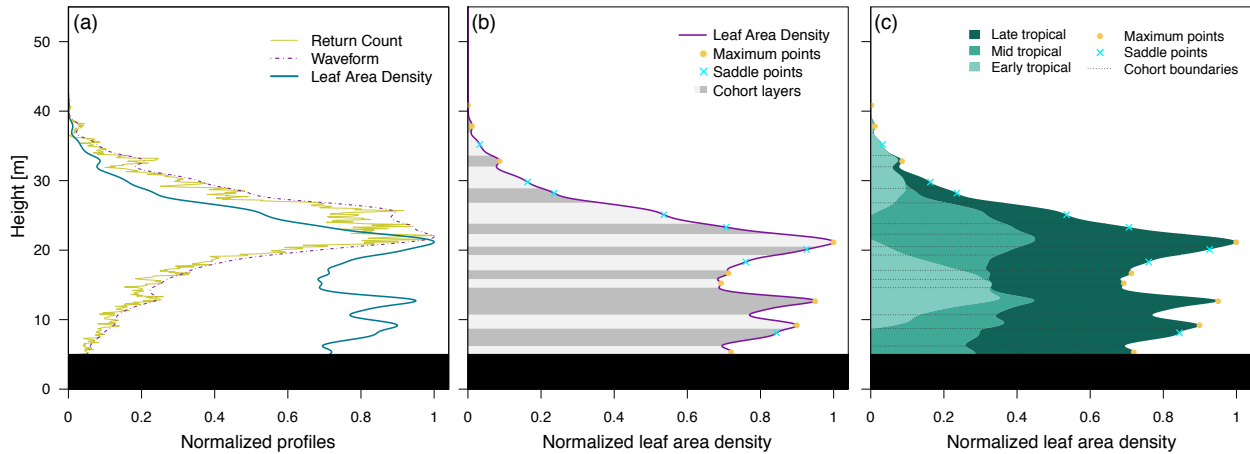


Figure S19. Example of how cohorts are obtained from the vertical distribution of returns, from one 50 × 50 m column at Paracou (GYF). (a) Thin lines: vertical profiles of return counts ( $X_v$ ; Eq. S26); dot-dashed lines: waveform function  $E_v$  (Eq. S25); thick lines: leaf area density ( $L_v$ ; Eq. S30). (b) Discrete layers based on the curve features of leaf area density (thick line); Circles are the local maximum points and crosses are the saddle points. Discrete cohort layers are shown in alternate background shades. (c) Plant functional type (PFT) and cohort attribution. Cohorts are defined by the cohort layers, and further split by the existing PFTs in each layer. The unscaled leaf area index of each cohort is defined by the integral of the curve between each discrete layer and within each plant functional group. Black rectangles near ground are the bottom layer that is excluded from the cohort attribution.

Figure S20. Comparison between forest inventory and airborne-lidar estimates of plot-level properties. (a) aboveground biomass carbon density (ABCD), (b) Basal area (BA), (c) (maximum, allometry-based) leaf area index and (d) stem number density (ND). For the airborne-lidar estimates, we show the average results from cross-validation: for each plot, we averaged all replicates which did not include the plot region in the model training step. Bars correspond to the 95% range of cross-validation predictions. Median bias, root mean square error (RMSE) and adjusted coefficient of determination ( $R_{adj}^2$ ) for cross-validation predictions are shown for reference.